Electromechanical Properties and Defect Chemistry of High-Temperature Piezoelectric Materials

Habilitationsschrift
zur Erlangung der venia legendi für das Fachgebiet

Materialwissenschaft

Fakultät für Natur- und Materialwissenschaften
der Technischen Universität Clausthal

vorgelegt von

Dr. Holger Fritze

Juni 2007

Abstract

Conventional piezoelectric materials such as quartz are widely used as high precision transducers and sensors based on bulk acoustic waves. However, their operation temperature is limited by the intrinsic materials properties to about 500°C. Anticipated high-temperature applications including thermogravimetry on small volumes and gas sensing based on stoichiometry change of thin sensor films are feasible by applying materials that retain their piezoelectric properties up to higher temperatures. Langasite ($La_3Ga_5SiO_{14}$) and gallium phosphate ($GaPO_4$) are promising candidates. Factors limiting potential use of those crystals include excessive conductive and viscous losses, deviations from stoichiometry and chemical instability. The objective of this work is to identify the related microscopic mechanisms, to correlate electromechanical properties and defect chemistry and to improve the stability of the materials by e.g. appropriate dopants.

Part I of this study is related to the electromechanical properties of langasite and gallium phosphate. They are determined at temperatures of up to 1050°C and described by a one-dimensional physical model. The latter is developed with special consideration of losses. Key properties relevant for stable operation of resonators are identified to be shear modulus, density, electrical conductivity and effective viscosity. In order to quantify their impact on frequency and damping, a generalized Sauerbrey equation is given. Further, an equivalent electrical circuit for high-temperature resonator devices is derived which makes the physical model handy for routine data evaluation.

Temperature ranges of predominant viscosity and conductivity related losses are identified. Most remarkably, langasite and gallium phosphate resonators are shown to exhibit bulk acoustic waves up to at least 1400 and 900°C, respectively. Their mass sensitivity at elevated temperatures is about as high as that of quartz at room temperature. Temperature related frequency fluctuations can be compensated almost entirely by using higher vibration modes. Within its operation temperature range, gallium phosphate shows significantly lower losses than langasite.

Part II is focussed on mass and charge transport in single crystalline langasite. Those phenomena are correlated with langasite's defect chemistry and electromechanical properties. First of all, the dominant charge carriers are identified. Undoped langasite shows predominant ionic conduction at elevated temperatures. As long as the atmosphere is nearly hydrogen-free, the transport is governed by oxygen movement. A dominant role of hydrogen is observed in hydrogenous atmospheres since the diffusion coefficient of hydrogen is orders of magnitude higher than that of oxygen.

The loss in langasite is found to be governed up to about 650°C by viscoelastic damping related to the above mentioned movement of oxygen ions. Based on langasite's defect chemistry donor doping is expected to lower that loss contribution and shown to be effective. Above 650°C the impact of the conductivity related loss becomes pronounced. Here, lowering the conductivity results generally in decreased losses.

Further, the evaluation of langasite's applicability is focused on mapping the regimes of gas insensitive operation. The most relevant feature with respect to frequency fluctuations of resonator devices is the formation of oxygen vacancies. The calculated frequency shift induced by redox related reactions only exceeds the limit of ± 4 Hz below 10^{-17} bar at 1000°C, below 10^{-24} bar at 800°C and below 10^{-36} bar at 600°C in nominally hydrogen free atmospheres. Water vapor is found to shift the resonance frequency at higher oxygen partial pressures. In the hydrogen containing atmospheres applied here, langasite can be regarded as a stable resonator material above oxygen partial pressures of above 10^{-13} bar at 800°C and 10^{-20} bar at 600°C. The incorporation of OH-groups into the material determines the frequency shift.

Finally, application examples are summarized to demonstrate the capabilities of high-temperature stable piezoelectric materials.

Contents

1 Introduction **1**
1.1 Piezoelectric Resonators 1
1.2 Open Questions 4
1.3 Objectives 6
1.4 Scope of this Work 8

I Electromechanical Properties **9**

2 Continuum-mechanical Models **11**
2.1 Thickness Shear Mode Resonators 11
2.2 One-dimensional Physical Model 13
2.3 Equivalent Circuit 24
2.4 Resonator Quality Factor 31
2.5 Limitations of the Models 35

3 Parameter Study **37**
3.1 One-dimensional Physical Model 37
3.2 Equivalent Circuit Model 46

4 Materials Properties **55**
4.1 Fit Procedure 55
4.2 Results 59

5 Resonance Properties **69**
5.1 Resonance Frequency 70
5.2 Temperature Compensation 72
5.3 Mass Sensitivity 75
5.4 Resonator Quality Factor 77
5.5 Mass Resolution 77
5.6 Impact of the Materials Parameters 80

II Atomistic Transport **83**

6 Defect Chemistry of Langasite **85**
6.1 Cation Sites 86
6.2 Hydrogen Free Atmospheres 88
6.3 Hydrogen Containing Atmospheres 95

7 Mass and Charge Transport **99**
7.1 Diffusive Transport 99
7.2 Equilibration Times 104
7.3 Ionic Conductivity 106
7.4 Electrical Conductivity 107
7.5 Gallium Loss 116

8 Correlation **121**
8.1 Gas Atmosphere Dependent Frequency 121
8.2 Correlation of Loss and Conductivity 125

III Application Relevant Studies and Outlook **133**

9 Application Relevant Studies **135**
9.1 Gas Sensor Applications 135
9.2 Micro-Electromechanical Structures 136
9.3 High-temperature Stable Electrodes 137

10 Outlook **141**
10.1 Models 141
10.2 Materials 142

Summary **143**

A Materials Data **147**

B Effective Electrode Area **152**

C Experimental Details **156**

D Terms and Acronyms **165**

Bibliography **171**

Chapter 1

Introduction

1.1 Piezoelectric Resonators

Quartz resonators vibrating in the thickness-shear mode are well known as Quartz Crystal Microbalances (QCM)[1]. Very small mass changes during film deposition onto resonators or gas composition dependent stoichiometry changes of thin films already deposited onto the resonators can be correlated with their resonance frequency shift [1, 2]. Thereby, specific surface affinity layers allow chemical sensing. Such devices are able to detect monolayer variations on its surface providing thereby a very high sensitivity. For example, changes in mass equivalent to 0.1 monolayers of oxygen atoms can be detected which enables the stoichiometry determination of surface oxides [3]. Fig. 1.1 presents a typical QCM setup which consists of a piezoelectric disk, key hole shaped electrodes and a sensor film.

Anticipated application fields of such resonant sensors are the in-situ deposition rate monitoring during chemical vapor deposition, thermogravimetry on small volumes and gas sensing based on stoichiometry change of thin sensor films. Thus, operating conditions exceeding 500°C are often required.

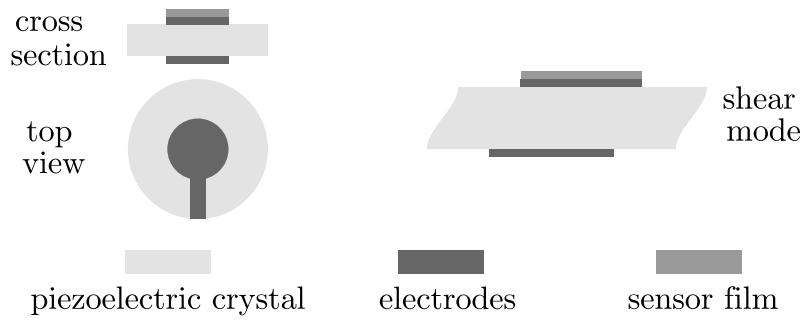

Figure 1.1: Piezoelectric resonator operated in the thickness shear mode.

[1]Terms and acronyms are listed in Appendix D.

Table 1.1: Operation temperature limits of piezoelectric materials.

material	temperature limit [°C]	remarks	reference
$Li_2B_4O_7$	230	excessive ionic conductivity	[6]
$LiNbO_3$	300	decomposition	[6–9]
$LiTaO_3$	300	decomposition	[6]
α-quartz	573	phase transformation	[4, 5]
$AlPO_4$	588	phase transformation	[6, 19, 20]
$GaPO_4$	970	phase transformation	[12–14]
AlN	∼1000	oxidation resistance	[15–18]
langasite	1470	melting point	[10, 11]

As a consequence, conventional piezoelectric materials cannot be used. Their maximum operation temperature is limited by intrinsic materials properties such as phase transformations and high losses. For example, α-quartz undergoes a destructive phase transformation at 573°C [4]. In practice, the maximum temperature of about 450°C is determined by high losses [5]. Non-stoichiometric lithium niobate ($LiNbO_3$) and lithium tetraborate ($Li_2B_4O_7$) either decompose at 300°C or exhibit phase transformations at 500°C, respectively [6–9]. The operation of piezoelectric materials can be extended to higher temperatures by applying materials that retain their piezoelectric properties up to higher temperatures. Langasite ($La_3Ga_5SiO_{14}$), its isomorphs and gallium phosphate ($GaPO_4$) are promising candidates for high-temperature applications. They enable operation temperatures significantly above 500°C. The ultimate temperature limits are given by the melting point of langasite and the phase transition of $GaPO_4$ at 1470 [10, 11] and 970°C [12–14], respectively. Aluminium nitride (AlN) can be, in principle, used up to 1150°C. However, the lack of sufficiently large crystals and poor oxidation resistance prevent its use [15–18].

Tab. 1.1 lists piezoelectric materials of practical relevance[2], with langasite theoretically having the highest possible operation temperature. Another important aspect focussing the interest on langasite is the availability of high quality and large size single crystals manufactured by the Czochralski technique [10, 11, 21]. Besides langasite, $GaPO_4$ is a very promising material for high-temperature applications as long as the operation temperatures do not exceed 900°C considerably. $GaPO_4$ is, in particular, expected to show low losses. However, productivity and yield of growing $GaPO_4$ single crystals is rather low. Extremely anisotropic growth rates, twinning and the incorporation of OH-groups in the crystals are observed [22–25]. Due to those

[2]Further materials of the langasite-related family of compositions are not listed.

difficulties the availability of $GaPO_4$ is limited which might prevent its large scale application. Further, there is still only one commercial supplier worldwide known[3].

The first compound of the langasite-related family of compositions was discovered at Moscow State University in 1979 [26]. Since then the material attracted significant attention for improved electronic oscillators and filters. Advantages of langasite over α-quartz include higher piezoelectric coupling which results in higher resonator quality factors, and thus in reduced phase noise [27–29]. However, a couple years had to pass before the interest turned on langasite's high-temperature properties [30–32]. For example, in 1998 langasite-based Surface Acoustic Wave (SAW) devices were operated for a short time at 1000°C [33]. The literature in those days did not contain meaningful data about the high-temperature properties of langasite [6]. In particular, the option to operate langasite as Bulk Acoustic Wave (BAW) resonator at high temperatures was under question. The latter was caused by the lack of conductivity data and of the knowledge about their impact on the resonance behavior.

The need for a High-Temperature Micro Balance (HTMB) and the above mentioned open questions inspired us to investigate langasite closely. In 1999, we could operate langasite BAW resonators up to 750°C [34]. Increasing experience in data acquisition and electrode preparation enabled the demonstration of even higher operation temperatures such as 900°C in 2000 [35, 36], 1050°C in 2004 [37] and more than 1400°C in 2005 [38, 39]. The high-temperature applicability of $GaPO_4$ BAW resonators was demonstrated to be 700°C by the commercial crystal supplier in 2001 [40]. In 2002 we could operate $GaPO_4$ resonators up to 900°C which is already close to its phase transition [41, 42]. Fig. 1.2 shows the temperature dependent resonance frequency of langasite and $GaPO_4$ thereby demonstrating the appearance of BAW's at high temperatures. The data of α-quartz are given for comparison.

In parallel to the demonstration of the maximum operation temperatures, the materials properties of langasite and $GaPO_4$ were investigated in the frame of a tight cooperation of groups from Massachusetts Institute of Technology (MIT) and Technical University of Clausthal (TUC). In 2002, a crystal growth group from Institute of Crystal Growth (IKZ), Berlin-Adlershof, joint the alliance. The main written outcome of this joint work are the thesis of Dr. Huankiat Seh [43] supervised by Prof. Dr. Harry L. Tuller, this work, related publications in journals and two patents [44, 45]. Further, a prototype of a langasite based sensor system has been developed in cooperation with other universities and companies [39].

[3]Piezocryst GmbH, Graz, Austria (formerly AVL List GmbH).

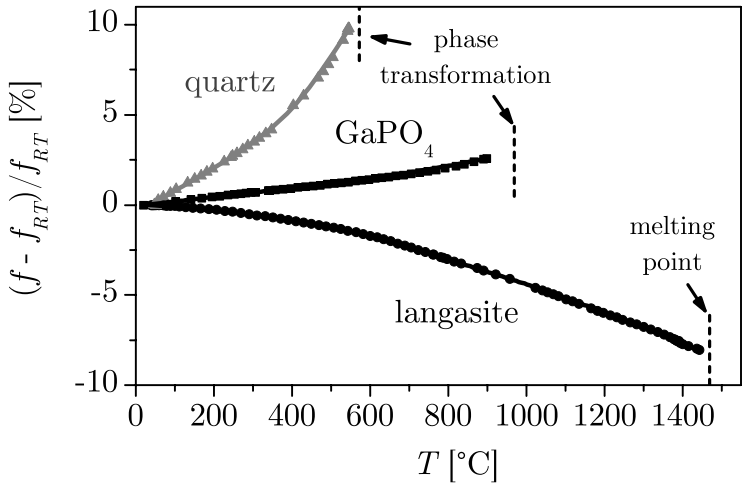

Figure 1.2: Temperature dependent resonance frequency of langasite, gallium phosphate and quartz BAW resonators.

1.2 Open Questions

The application of piezoelectric materials as sensor platform at high temperatures requires environmental independent operation. For example, the minimization of stoichiometry changes is essential to insure high mass resolution in films applied to the HTMB's. The same requirement applies for electrode materials. In contrast, sensor films are supposed to show large environmental dependent mass changes. Consequently, the properties of those sensor device components must be addressed.

1.2.1 Piezoelectric Materials

Key operation-temperature limitations of the piezoelectric crystals, i.e. phase transformations or melting, are already discussed. The accurate knowledge of their temperature dependent electromechanical properties including

- Piezoelectric coefficients and electromechanical coupling factor,
- Elastic constants,
- Viscosity and
- Electrical conductivity and dielectric constants

is the precondition for the understanding of the microscopic mechanisms. Further, the evaluation of the chemical stability is required. Here, the potential loss of gallium is a key issue. Those phenomenological properties are related to open questions such as the impact of

- Excessive conductive and viscous damping,

- Deviations from stoichiometry and
- Chemical instability

on the resonance behavior. Thus, the kinetic mechanisms controlling electronic and ionic transport and the bulk resonant characteristics in this oxides must be evaluated at high temperatures. Further, related models describing the defect chemistry and the atomistic transport must be established.

The operation of piezoelectric resonators as sensor platform at elevated temperatures requires, in general, temperature independence of the resonance frequency. Options to exclude temperature effects such as

- Temperature compensated cuts and
- Compensation methods

must be realized and tested. Another important application relevant property to be determined is the mass sensitivity.

As for room temperature applications, the resonance behavior might be impacted by mechanical stress. High-temperature operation faces effects due to

- Differences in the Coefficients of Thermal Expansion (CTE) of resonator, electrode and sensor film material and
- Stoichiometry change or
- Phase transition related changes of the sensor film volume

which have to be considered.

1.2.2 Electrode Materials

Aside the stability of the piezoelectric materials itself, electrodes must be applied that remain stable under harsh environments. In particular,

- Highly conductive,
- Chemically stable and
- Adherent

electrodes are required. Additionally, the electrodes of resonant devices experience extremely high accelerations. Therefore, they must represent a good compromise on high conductivity and low mass. The mechanical properties must be nearly gas atmosphere and temperature independent to avoid disturbances of the resonance behavior. Consequently, the demands on electrodes for resonant devices exceed those for common high-temperature electrodes.

1.2.3 Sensor Film Materials

Sensor materials showing large stoichiometry changes as function of the surrounding atmosphere must be identified in order to take advantage of the

high-temperature operation of the piezoelectric resonators. The sensor films should exhibit

- Large relative mass changes due to e.g. reduction,
- Short diffusion lengths in order to achieve fast response and
- Chemical stability and low volatility for long term stability and reproducibility of the sensor signal.

Further, porous films might be applied. They provide short diffusion lengths and large surfaces. The letter is advantageous as long as sufficiently low temperatures enable the use of gas adsorption processes. But, it is an open question, if the mechanical stiffness of porous films is sufficient to be used on top of resonant sensors.

1.3 Objectives

1.3.1 Piezoelectric Materials

From the very beginning, this work was focussed on the detailed investigation of langasite because of its high theoretical operation temperature limit of 1470°C. The subsequent demonstration of operation temperatures close to this limit justified the choice. Thereby, langasite is regarded as model compound representing the langasite-related family of compositions. $GaPO_4$ is included in the investigations since it offers extremely low losses. The fact is advantageous as long as the operation temperature does not exceed 900°C considerably. Relevant data of α-quartz are determined and presented for comparison, only.

The research objectives originate from the open questions outlined in Section 1.2.1. First, the electromechanical properties of the above mentioned piezoelectric materials must be determined accurately and modeled up to temperatures as close as possible to the respective ultimate limit. Further, the microscopic mechanisms which determine

- Losses,
- Non-stoichiometry and
- Kinetics of oxidation-reduction

have to be investigated. Special emphasis must be taken on viscosity related losses since they are suspected to limit the sensing capabilities. For that, the viscous damping and potential correlations with other materials parameters have to be explored. These studies must include, in particular, the investigation of the defect chemistry of the piezoelectric materials. Thereby, the

- Predominant charge carriers,
- Ionic and electronic contributions to the conductivity and

- Effects of dopants and hydrogenous species on electrical and mass transport properties at different oxygen partial pressures and temperatures

are intended to be identified.

Based on these results, application conditions should be derived which include ranges of gas insensitive operation and sufficiently low damping of the piezoelectric resonators. Further, concepts to improve the piezoelectric materials should be proposed and tested. Minimized stoichiometry changes and low losses should be achieved by selecting

- Dopants which shift the stoichiometric composition of the piezoelectric materials to operation conditions of interest,
- Compositions in which oxygen vacancy creation is less favorable,
- Conditions in which diffusion kinetics plays a minor role and
- Alternate candidates in the langasite-related family of compositions.

Finally, application relevant aspects such as temperature coefficients, temperature compensation and mass sensitivity must be evaluated.

1.3.2 Electrodes and Sensor Films

Thin film platinum electrodes are intended to be applied initially. The choice is predominantly motivated by its presumably small impact on the resonance properties of resonator devices. The stability limits of such electrodes must be explored including

- Chemical and thermal stability with special emphasis to evaporation of volatile platinum suboxides,
- Reactions at the interface electrode-resonator,
- Adhesive strength and
- Electrical conductivity degradation.

Further steps in development of reliable high-temperature electrodes and adhesive layers involve Pt-Rh alloys, Titanium nitride and lanthanum strontium manganate (LSM). The investigation of their materials properties must consider the above mentioned issues and potential non-stoichiometries in case of ceramic electrodes.

Sensor film materials commonly applied in resistive high-temperature gas sensors can be used for HTMB's provided that they exhibit large environmental related mass changes. The electrical properties and the operation conditions of films such as $TiO_{2-\delta}$ and $CeO_{2-\delta}$ are well known. These materials are stable end expected to cause large frequency shifts via reduction or oxidation. For example, titanium shows a change in mass during oxidation of 67 % (Ti to TiO_2). Potential sensor materials for the measurement

of relatively high oxygen partial pressures are $CeO_{2-\delta}$ and $Pr_xCe_{1-x}O_{2-\delta}$. The above mentioned materials are intended to be tested as environmental dependent mass load for resonant sensors.

1.4 Scope of this Work

The results presented subsequently are predominantly focused on

- Electromechanical properties of the piezoelectric materials,
- Correlation of defect chemistry and electromechanical properties,
- Determination of the operation limits and
- Improvement of the piezoelectric materials.

Further, application relevant studies such as gas sensor testing, micromachining of piezoelectric materials and development of high-temperature stable electrodes has been performed. These studies are described very briefly in Section 9.1. References for further reading are given therein.

The defect chemistry of langasite was predominantly investigated by the MIT group. Some contributions such as diffusivities of the ions were provided by the TUC group. Nominally undoped and doped langasite crystals were provided by the IKZ.

Part I of this work presents materials properties of langasite, $GaPO_4$ and α-quartz such as elastic constants, piezoelectric coefficients, effective viscosity and their temperature and oxygen partial pressure dependencies. The analysis bases on a physical model of the resonator devices and enables the identification of crucial properties for resonator operation and application relevant characteristics such as temperature coefficients and mass sensitivity.

Part II correlates electromechanical properties and defect chemistry of langasite, thereby identifying the operation limits. Further, suggestions to decrease the loss are realized and proven. Part II is exclusively focussed on langasite due to its potential to be operated at very high temperatures and the need to decrease losses.

Part I

Electromechanical Properties

Chapter 2

Continuum-mechanical Models

The first part of this section describes the electromechanical properties of thickness shear mode resonators based on a one-dimensional physical model. Thereby, special attention is drawn to losses. In the second part, an equivalent circuit and relations of its parameters to the electromechanical properties of the resonators are derived. Thereby, approximations are introduced which make the exact model handy for routine data evaluation. Finally, the strength and limitations of the continuum-mechanical model are discussed.

2.1 Thickness Shear Mode Resonators

2.1.1 Crystal Symmetry

The piezoelectric materials langasite, gallium phosphate and α-quartz belong to the same crystal class and point group, namely the trigonal system and 32, respectively. Therefore, their electromechanical properties can be described by a single physical model. In particular, approaches known for quartz can be reviewed and modified for resonators operated at high temperatures.

The materials properties mechanical stiffness c, piezoelectric e and dielectric constant ε as well as physical properties such as the mechanical stress T are tensors of different order. The inherent tensor notation can be transformed into a compressed matrix notation since the symmetry of the crystals reduces the number of non-zero tensor components drastically. The approach is described in detail in [46, 47] and leads for the piezoelectric materials of interest to Eq. 2.1[1] with $c_{66} = \frac{1}{2}(c_{11} - c_{12})$. The axis of the corresponding coordinate system are denoted by x_1, x_2 and x_3 in order to relate the indices to the matrix notation. Thereby, $x_3 = z$ is oriented parallel to the crystallographic c axis. The $x_1 = x$ axis coincides in direction and sense with any one of the crystallographic a axes. The $x_2 = y$ axis is perpendicular to x_1 and x_3, oriented as to form a right-handed system [48]. The crystallographic

[1] The superscript t indicates the transposed matrix.

axis are visualized in Fig. 6.1. Numerical values of the matrix coefficients for langasite, $GaPO_4$ and quartz are given in Appendix A.

$$\left(\begin{array}{c:c} c & e^t \\ \hdashline e & \varepsilon \end{array}\right) = \left(\begin{array}{cccccc:ccc} c_{11} & c_{12} & c_{13} & c_{14} & 0 & 0 & e_{11} & 0 & 0 \\ c_{12} & c_{11} & c_{13} & -c_{14} & 0 & 0 & -e_{11} & 0 & 0 \\ c_{13} & c_{13} & c_{33} & 0 & 0 & 0 & 0 & 0 & 0 \\ c_{14} & -c_{14} & 0 & c_{44} & 0 & 0 & e_{14} & 0 & 0 \\ 0 & 0 & 0 & 0 & c_{44} & c_{14} & 0 & -e_{14} & 0 \\ 0 & 0 & 0 & 0 & c_{14} & c_{66} & 0 & -e_{11} & 0 \\ \hdashline e_{11} & -e_{11} & 0 & e_{14} & 0 & 0 & \varepsilon_{11} & 0 & 0 \\ 0 & 0 & 0 & 0 & -e_{14} & -e_{11} & 0 & \varepsilon_{11} & 0 \\ 0 & 0 & 0 & 0 & 0 & 0 & 0 & 0 & \varepsilon_{33} \end{array}\right) \tag{2.1}$$

2.1.2 Orientation of the Resonators

Unless specified otherwise the resonators used here are plane-parallel disks where the axis normal to the surface is oriented in the x_2-direction (y-cut[2]). Describing the resonators by a one-dimensional model as done in the following section, the electrical field E across the resonator is parallel to this direction

$$E = \begin{pmatrix} 0 \\ E_2 \\ 0 \end{pmatrix}. \tag{2.2}$$

In order to identify the vibration mode of such resonators, the displacement of the resonator surfaces caused by an electric field must be determined. The relative position of two opposite points at the resonator surfaces is given by

$$x = \begin{pmatrix} 0 \\ d_R \\ 0 \end{pmatrix} \tag{2.3}$$

whereas its displacement u follows from

$$u = Sx. \tag{2.4}$$

Thereby, d_R and S represent the thickness of the resonator and the mechanical strain, respectively. The latter property can be calculated using the equation for the inverse piezoelectric effect

$$S = d^t E. \tag{2.5}$$

Here, d represents an alternative notation of the piezoelectric constant with $e_{ip} = d_{iq}c_{qp}$ [48]. From Eqs. 2.1–2.5 and the electrical potential across the

[2]The crystal cut designation follows [48].

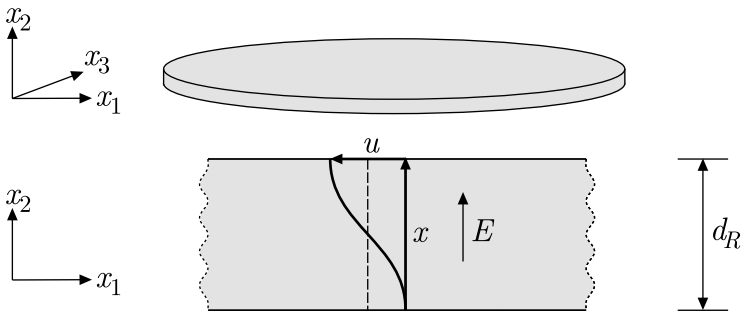

Figure 2.1: Orientation and displacement of the TSM resonators used here.

resonator with $\phi = d_R E_2$, the displacement yields

$$u = \begin{pmatrix} -d_R E_2 d_{11} \\ 0 \\ 0 \end{pmatrix} = \begin{pmatrix} -\phi\, d_{11} \\ 0 \\ 0 \end{pmatrix}. \tag{2.6}$$

Thus, when the electric field is applied in the x_2 direction, the mechanical displacement is in the x_1 direction. In other words, the piezoelectric plate undergoes a shear deformation across its thickness. The corresponding vibration mode is called thickness shear mode (TSM) and results in a displacement as shown schematically in Fig. 2.1.

The following models are developed for y-cut resonators. Nevertheless, the TSM vibration of differently oriented resonators can be described by the same approach using modified materials data. Essentially, the matrix according to Eq. 2.1 has to be rotated as described e.g. in [47].

2.2 One-dimensional Physical Model

The materials properties of a resonator can be determined according to the IEEE standard 176-1987 [48] as long as low losses apply. The method described therein requires the measurement of the electrical impedance $Z = R + jX$ or admittance $Y = G + jB = 1/Z$ of a resonator device in the vicinity of the resonance frequency. The data evaluation bases on the approximation that

1. Resonance frequency $f(|Z|_{min})$ and series resonance frequency $f_S = f(G_{max})$, and
2. Anti-resonance frequency $f(|Z|_{max})$ and parallel resonance frequency $f_P = f(R_{max})$

are equal, respectively. The approximation is fulfilled for low losses only [49]. Since this work is focussed on high-temperature properties where high losses are expected, a more elaborate approach has to be chosen.

2.2.1 Constitutive Equations

A coated TSM resonator can be described by a three-dimensional physical model taking into consideration the materials properties mentioned above. The full set of differential equations is, however, difficult to solve. Numerical approaches such as the finite element method are hardly applicable due to difficulties arising from high aspect ratios between the diameter of film or resonator and their thickness. In addition, computing time and memory prevents the use of finite element methods for routine data evaluation [50]. Analytical two- or three-dimensional solutions are available for uncoated resonators, only [51–53]. Since this work includes application relevant resonator devices wearing environmentally sensitive films, the problem of coated resonators must be treated. An alternative approach is the application of a one-dimensional model which provides an analytical solution and enables the straight forward discussion of the impact of the materials properties of resonator and film on the resonance behavior. The further analysis shows that the restrictions caused by the one-dimensional model are tolerable.

The electrical response of a piezoelectric resonator can be calculated based on constitutive equations, namely [47, 54]

- Linear piezoelectric equations,
- Newton's equation of motion and
- Maxwell's equations.

As mentioned in Section 2.1.1, certain components of the tensors for the mechanical stiffness c and the piezoelectric constant e vanish for the crystals of interest. This fact, the consideration of an infinite plate in x_1- and x_3-direction and shear displacements exclusively in the x_1-direction simplify the constitutive equations. In other words, a one-dimensional model can be introduced where the physical properties changes along the x_2-direction, only. If no losses occur, the mechanical stress tensor T and the electrical displacement D result in [55][3]

$$T_{12} = c_{66}\frac{\partial u_1}{\partial x_2} + e_{26}\frac{\partial \phi}{\partial x_2} \tag{2.7}$$

and

$$D_2 = e_{26}\frac{\partial u_1}{\partial x_2} - \varepsilon_{22}\frac{\partial \phi}{\partial x_2}, \tag{2.8}$$

respectively. Both equations are coupled with the equation of motion

$$\frac{\partial T_{12}}{\partial x_2} = \rho_R \ddot{u}_1. \tag{2.9}$$

[3]It must be noted that viscoelastic losses are already introduced in [55]. The term is skipped here since it is later introduced in its generic form, i.e. as imaginary part of the mechanical stiffness.

Thereby, ρ_R represents the density of the resonator material. Further, the Maxwell equation simplifies to

$$\frac{\partial D_2}{\partial x_2} = 0. \tag{2.10}$$

Considering a harmonic time dependence $e^{j\omega t}$ with $\omega = 2\pi f$ as angular frequency, Eqs. 2.7–2.10 can be transformed to

$$\left(c_{66} + \frac{e_{26}^2}{\varepsilon_{22}}\right) \frac{\partial^2 u_1}{\partial x_2^2} = -\omega^2 \rho_R u_1 \tag{2.11}$$

and

$$e_{26} \frac{\partial^2 u_1}{\partial x_2^2} - \varepsilon_{22} \frac{\partial^2 \phi}{\partial x_2^2} = 0. \tag{2.12}$$

Since the number of relevant tensor elements is reduced to one for each physical property and their assignment to the resonator material must be ensured, the substitutions

$$\begin{aligned} \varepsilon_R &= \varepsilon_{22}, \\ e_R &= e_{26} \quad \text{and} \\ c_R &= c_{66} + e_R^2/\varepsilon_R \end{aligned} \tag{2.13}$$

are introduced. Thereby, a new property, the piezoelectrically stiffened shear modulus c_R, is defined.

Additional layers, i.e. electrodes and sensor films, can be treated in a similar fashion. The situation becomes simplified since non-piezoelectric materials are regarded. In analogy to Eq. 2.11 the equation of motion results in

$$c_F \frac{\partial^2 u_1}{\partial x_2^2} = -\omega^2 \rho_F u_1. \tag{2.14}$$

Here, c_F and ρ_F represent the shear modulus and the density of the film, respectively. If necessary, the index F is extended to F_n with $n = 1, 2 \ldots$ in order to denote several layers. The dielectric properties of the films are not introduced since the resonance behavior is expected to be independent of this properties within the one-dimensional model. The surfaces of the resonator, i.e. in practice the underlying electrodes, are regarded as equipotential planes which prevents any drop of the electrical potential within the films.

The equations presented so far, are state of the art and can be found in textbooks such as [46, 47, 54]. However, a complete analytical solution of the one-dimensional physical model reflecting all types of material related losses is obviously not available. Therefore, the following section presents that solution.

2.2.2 Material Related Losses

The description of a resonator device requires the consideration of losses from different origins. Factors which affect the loss include [47, 56]

- Intrinsic properties of the resonator material such as
  - Electronic and ionic transport,
  - Interstitial diffusion,
  - Motion of dislocations,
- Resonator design and manufacturing such as
  - Resonator blank geometry (contour, dimensional ratios),
  - Electrode geometry,
  - Surface finish,
- Operation conditions such as
  - Mounting stresses,
  - Drive level,
  - Overtone number,
  - Viscosity of the surrounding medium and
  - Ionizing radiation.

The resonator design and manufacturing as well as the operation conditions must meet certain standards to insure proper operation of the resonators. These requirements are well known and excessively published for quartz under room temperature conditions, e.g.:

- Flat or plano-plano resonators with a diameter to thickness ratio greater than 50 usually provide acceptable performance if they are operated in the fundamental mode [57].
- The diameter of the electrodes should be generally smaller than 40 % of the resonator diameter.
- The separation of unwanted spurious modes from the resonance frequency can be achieved by limiting the diameter of electrodes as function of the resonator thickness as described in [58].

The resonators used here follow essentially these standards and show low losses at room temperature.

Since this work is focussed on high-temperature operation of the resonators, material related losses are expected to be dominant at elevated temperatures. To include these losses, the shear modulus, the dielectric constant and the piezoelectric constant of the resonator materials have to be, in general, treated as complex quantities. The imaginary parts of

$$\hat{c}_{66} = c_{66} + j\omega\eta_R \tag{2.15}$$

and

$$\hat{\varepsilon}_R = \varepsilon_R - j\,\frac{\sigma_R}{\omega} \tag{2.16}$$

stand for the mechanical and dielectric loss, respectively [47, 49][4]. Thereby, η_R represents the effective viscosity whereas σ_R expresses the electrical conductivity of the resonator.

It should be noted that the mechanical and dielectric losses are related by the complex dielectric constant included in c_R according to Eq. 2.13. The fact reflects the piezoelectric coupling which causes a depolarization field. The latter is affected by dissipation effects of mobile charge carriers [47].

The complex piezoelectric constant is given by

$$\hat{e}_R = e_R + j\,\epsilon_R. \tag{2.17}$$

Thereby, the name of the imaginary part ϵ_R is not specified since there is no simple physical interpretation. Irrespective of its origin, ϵ_R can be seen as phase lag between the electrical and mechanical properties. Microscopic explanations are e.g. the jumping of lattice defects or the movement of domain walls in polycrystalline materials [59, 60]. However, for most materials systems ϵ_R can be set to zero [47]. The validity of this approximation for the materials of interest in this work is justified in Section 4.1.3. Nevertheless, ϵ_R is included into to the set of equations in order to evaluate its impact on the resonance behavior.

In analogy to Eq. 2.15, films can be described by

$$\hat{c}_F = c_F + j\omega\eta_F \tag{2.18}$$

with η_F as viscosity of the film.

2.2.3 Boundary Conditions

So far, Eqs. 2.11–2.14 describe resonator and layers independently. For completeness, boundary conditions have to be defined. A typical resonant sensor shows a sequence of layers as visualized in Fig. 2.2a. However, the system can be simplified if the focus is drawn to three cases,

(1) Modeling of the resonance behavior,

(2) Determination of the resonator properties and

(3) Determination of the sensor film properties.

The first case can be realized assuming bare resonators where the electrical potential is applied without any impact on the mechanical behavior. The layer sequence in Fig. 2.2b corresponds to this situation if

[4] In [49] the electromechanical coupling $K^2 = \varepsilon^2/(ec)$ is considered instead of ε.

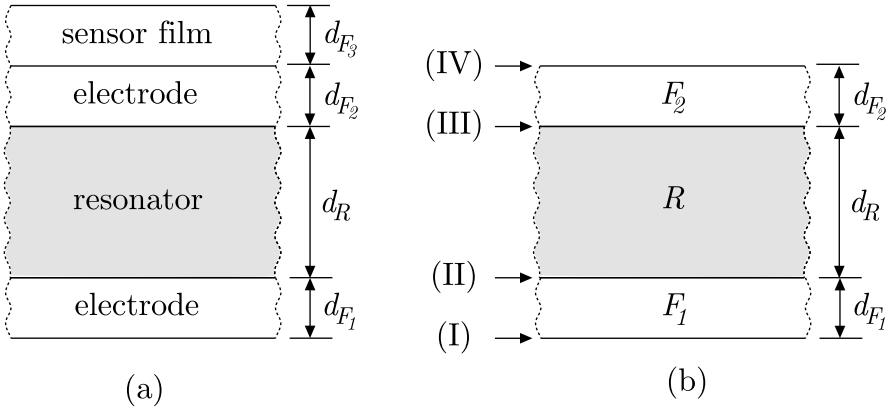

Figure 2.2: Typical resonator device (a) and layer sequence suited for modeling and determination of the resonator and sensor film properties (b).

- R represents the resonator and
- F_1 and F_2 vanish by setting its acoustic load impedance (see below) to zero.

The second case requires resonators without sensor films and the exact consideration of the electrodes. The situation corresponds to Fig. 2.2b whereas

- R stands for the resonator and
- F_1 and F_2 represent the electrodes.

In the third case, resonator and electrodes can be regarded as unit and described by effective properties as long as the electrodes are thin. Essentially, the thickness of the resonator d_R has to be replaced by an effective thickness. The layer sequence in Fig. 2.2b correspond to these situations if

- R represents resonator and electrodes,
- F_2 is regarded as sensor film and
- F_1 vanishes by setting its acoustic load impedance (see below) to zero.

Consequently, an unique layer sequence as shown in Fig. 2.2b can be used to represent the three cases mentioned above. Such resonator meet the boundary conditions

(I),(IV) at the film surface with
  - vanishing shear stress $T_{12} = 0$,

(II) at the lower interface crystal–film with
  - continuous displacement u_1,
  - continuous shear stress T_{12},
  - driving potential $\phi = \phi_0\, e^{j\omega t}$,

(III) at the upper interface crystal–electrode with

- continuous displacement u_1,
- continuous shear stress T_{12} and
- driving potential $\phi = -\phi_0\, e^{j\omega t}$.

2.2.4 Solution of the One-dimensional Model

Finally, the equations describing the lossy system of resonator and layers have to be be solved in analogy to the approach for room temperature conditions chosen in [55, 61, 62]. Thereby, the current I in x_2 direction can be calculated from the electrical displacement D_2

$$I_2 = \frac{\partial}{\partial t} \int_{A_R} D_2 \, dA \tag{2.19}$$

and converted in an electrical impedance of a finite resonator

$$\widetilde{Z} = \frac{2\phi}{I_2} \tag{2.20}$$

whereas A_R represents the area of the resonator. For this and the following equations the tilde indicates an intermediate result which refers to the area A_R. In case of a single layer on each side of the resonator $\widetilde{Z}$ yields

$$\widetilde{Z} = \frac{d_R}{j\,\omega A_R\,\hat{\varepsilon}_R} \left(1 - \frac{K^2 \left(\zeta_{F_1} + \zeta_{F_2} + 2\tan\frac{\alpha_R}{2} \right)}{\alpha_R \left(1 - \zeta_{F_1}\zeta_{F_2} + (\zeta_{F_1} + \zeta_{F_2}) \cot\alpha_R \right)} \right). \tag{2.21}$$

Thereby, the abbreviations

$K^2 = \hat{e}_R^2 / (\,\hat{\varepsilon}_R \hat{c}_R)$

for the electromechanical coupling coefficient of the resonator material,

$\zeta_{F_n} = \sqrt{\rho_{F_n} \hat{c}_{F_n}} / \sqrt{\rho_R \hat{c}_R}\ \tan\,\alpha_{F_n}$

for the normalized acoustic load impedance,

$\alpha_R = \omega d_R \sqrt{\rho_R / \hat{c}_R}$

and

$\alpha_{F_n} = \omega d_{F_n} \sqrt{\rho_{F_n} / \hat{c}_{F_n}}$

for the acoustic phase shift inside the resonator and the film, respectively,

are used.

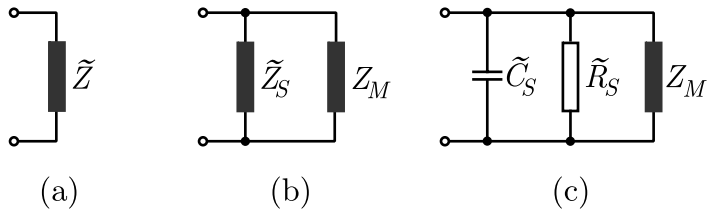

Figure 2.3: Equivalent circuit corresponding to Eqs. 2.21 (a), 2.23, 2.24 (b) and 2.23, 2.25, 2.26 (c).

For the further discussion $\widetilde{Z}$ is interpreted as a parallel arrangement of the motional impedance Z_M and static impedance $\widetilde{Z}_S$[5]

$$1/\widetilde{Z} = 1/Z_M + 1/\widetilde{Z}_S \qquad \text{or} \qquad \widetilde{Z} = Z_M \parallel \widetilde{Z}_S \tag{2.22}$$

with

$$Z_M = \frac{d_R}{j\,\omega A_R \hat{\varepsilon}_R} \left(\frac{\alpha_R(1 - \zeta_1\zeta_2 + (\zeta_1 + \zeta_2)\cot\alpha_R)}{K^2\left(\zeta_1 + \zeta_2 + 2\tan\frac{\alpha_R}{2}\right)} - 1 \right) \tag{2.23}$$

and

$$\widetilde{Z}_S = \frac{d_R}{j\,\omega A_R \hat{\varepsilon}_R}. \tag{2.24}$$

$\widetilde{Z}_S$ represents the bulk properties of the resonator with respect to the area A_R. The fact becomes obvious by expanding the complex dielectric constant $\hat{\varepsilon}_R$ leading to a parallel arrangement of the capacitance $\widetilde{C}_S$

$$\widetilde{C}_S = \varepsilon_R \frac{A_R}{d_R} \tag{2.25}$$

and resistance $\widetilde{R}_S$

$$\widetilde{R}_S = \frac{1}{\sigma_R} \frac{d_R}{A_R} \tag{2.26}$$

The corresponding elements of the equivalent circuit are visualized in Figure 2.3.

2.2.5 Effective Resonator Area

The modeling of a finite resonator device requires the introduction of the area A_R as done by Eq. 2.19. In the following the property is discussed in detail.

The one-dimensional physical model describes a resonator of infinite dimensions in the x_1–x_3 plane which results in a constant amplitude of mechanical vibration u_1 for a given value of x_2. In contrast, finite and, in particular,

[5]The right side of Eq. 2.22 represents a short notation of the left side. In the following the notation will be also applied to more than two parallel elements.

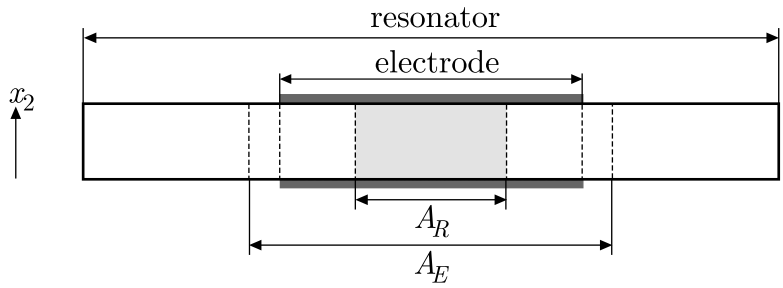

Figure 2.4: Cross section of a circular TSM resonator and extent of the characteristic areas A_R and A_E which lie in the x_1–x_3 plane.

partially electroded resonators exhibit a distribution of their amplitude in the x_1–x_3 plane which can be approximated by a Gaussian function [63]

$$u_1(x_1) = u_1^{max}\ e^{-w\,{x_1}^2}. \tag{2.27}$$

Thereby, w and u_1^{max} stand for the width and the maximum of the distribution, respectively. As a consequence, the one-dimensional model is applicable to finite devices provided that the problem of the conflictive amplitude distribution can be solved. For that purpose, the fundamental approach chosen here is to replace the area showing the amplitude distribution by an effective area of constant amplitude. Within the one-dimensional model, the effective area corresponds to the already introduced property A_R. Measured values of A_R are given in Section 4.2.2 and found to be substantially smaller than the effective electrode area A_E as depicted in Fig. 2.4. The difference between the areas can be explained qualitatively by comparing the distributions of the mechanical amplitude and of the electrical field which determine the effective values of A_R and A_E, respectively:

- The amplitude of the mechanical vibration at the border of the electrode u_1^b with respect to the maximum at the center of the electrode u_1^{max} is small, e.g. $u_1^b/u_1^{max} = 0.08$ for typical TSM resonators [63]. The amplitude distribution depends on the mass of the electrodes. Even gold electrodes[6] of only 25 nm lead to $u_1^b/u_1^m = 0.4$ [64]. Therefore, the average amplitude is always smaller than the maximum amplitude. The fact can be described by an effective area A_R which is smaller than the geometrical area of the electrode.
- The distribution of the electrical field is largely homogenous. There is a minor impact of fringing fields, only[7]. Consequently, A_E corresponds roughly to the geometrical electrode area.

[6]The situation is comparable to platinum electrodes applied here since their density is similar.

[7]The effective electrode area A_E is 5–10 % larger than the geometrical electrode area due to the fringing field. Details are given in Appendix B.

So far, the static impedance $\widetilde{Z}_S$ refers to A_R. Consequently, the property does not reflect the effective electrode area A_E of finite resonators. The required modification can be achieved by replacing A_R by A_E in Eqs. 2.24–2.26 leading to the static impedance Z_S

$$Z_S = \frac{d_R}{j\,\omega A_E \hat{\varepsilon}_R} \tag{2.28}$$

with the capacitance C_S

$$C_S = \varepsilon_R \frac{A_E}{d_R} \tag{2.29}$$

and the resistance R_S

$$R_S = \frac{1}{\sigma_R} \frac{d_R}{A_E}. \tag{2.30}$$

Thus, the impedance of the resonator device follows in analogy to Eq. 2.22 from

$$Z = Z_M \parallel Z_S = Z_M \parallel C_S \parallel R_S \tag{2.31}$$

and Eqs. 2.23 and 2.28–2.30. The corresponding equivalent circuit is visualized in Fig. 2.5a.

For completeness, a lead resistance R_L and a stray capacitance C_L have to be added. These elements reflect predominantly the properties of the sample holder. The arrangement of R_L and C_L is chosen as shown in Fig. 2.5b and results for the total impedance Z_T of resonator and holder in

$$Z_T = [(Z_M \parallel C_S \parallel R_S) + R_L] \parallel C_L. \tag{2.32}$$

Actual measurements are performed using a calibrated setup consisting of network analyzer and sample holder. Therefore, R_L and C_S essentially vanish. Nevertheless, these properties are kept in the equivalent circuit and fitted to the resonance spectra in order to detect potential electrode degradation or other unexpected effects.

In summary, the approach bases on a motional and a static part of the impedance which are related to different areas, namely the effective resonator area and the effective electrode area. The distinction of these areas is not necessarily required at or near room temperature where the resonators are highly resistive. Under such circumstances

- The static resistance R_S does not appear in common models and
- The part of the static capacitance which is related to the difference $A_E - A_R$ can be assigned to the stray capacitance C_L.

Despite the inconsistency regarding the static capacitance, common models describe the experimental results satisfactorily. However, problems arise as soon as the static resistance and capacitance get changed due to e.g. high operation temperatures (see also Appendix B.2).

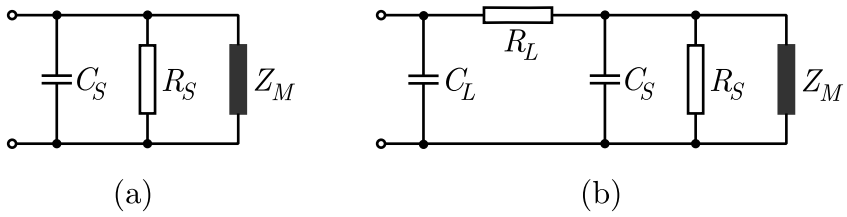

Figure 2.5: Equivalent circuit for the resonator (a) and the resonator including lead resistance and stray capacitance (b).

2.2.6 Typical Layer Sequences

The motional impedance according to Eq. 2.23 can be simplified for some typical layer sequences which are

- The bare resonator where $\zeta_{F_1} = \zeta_{F_2} = 0$ with

$$Z_M^R = \frac{d_R}{j\,\omega A_R \hat{\varepsilon}_R} \left(\frac{\alpha_R \cot \frac{\alpha_R}{2}}{2K^2} - 1 \right). \tag{2.33}$$

  The expression can be used to model the impact of the materials properties on the resonance properties.

- The resonator coated with identical films where $\zeta_{F_1} = \zeta_{F_2} = \zeta_F$ with

$$Z_M^E = \frac{d_R}{j\,\omega A_R \hat{\varepsilon}_R} \left(\frac{\alpha_R \left(1 - \zeta_F^2 + 2\zeta_F \cot \alpha_R\right)}{2K^2 \left(\zeta_F + \tan \frac{\alpha_R}{2}\right)} - 1 \right). \tag{2.34}$$

  The equation corresponds e.g. to a resonator coated with (identical) electrodes and allows to determine the materials properties as described in Section 4.2.2.

- The resonator coated with one film where $\zeta_{F_1} = \zeta_F$ and $\zeta_{F_2} = 0$ with

$$Z_M^S = \frac{d_R}{j\,\omega A_R \hat{\varepsilon}_R} \left(\frac{\alpha_R \left(1 + \zeta_F \cot \alpha_R\right)}{K^2 \left(\zeta_F + 2 \tan \frac{\alpha_R}{2}\right)} - 1 \right). \tag{2.35}$$

  The film can act as environmental dependent acoustic load. The device represents a sensor where resonator and electrodes are regarded as unit with an effective thickness.

In summary, the modeling of the electrical impedance of TSM resonators results in Eq. 2.32 with the static part according to Eqs. 2.29 and 2.30 and the motional part according to Eq. 2.33, 2.34 or 2.35. These equations are the initial point for the evaluation of the resonance properties of TSM resonators.

2.3 Equivalent Circuit

Despite the availability of an analytical solution for the one-dimensional physical model it is advantageous to convert it into an equivalent circuit (EC). First, the impact of environmental changes on the EC elements can be discussed. Thereby, the interpretation of the resonance spectra becomes easier since numerous empirical approaches are described in textbooks. Secondly, a reduced numerical effort to evaluate data is expected which enables the efficient handling of large data volumes.

In part, the equivalent circuit for TSM resonators is already introduced by the lumped elements representing the bulk properties and the resonator holder as shown in Fig. 2.5b. However, the most crucial part, the motional impedance Z_M, is still unevaluated. Eqs. 2.33, 2.34 or 2.35 are hardly suited to discuss the impact of the materials parameters on the resonance behavior. Therefore, it is attempted to transform Z_M into a serial and parallel arrangement of contributions of the form

$$Z_R = R, \quad Z_C = -j\frac{1}{\omega C} \quad \text{or} \quad Z_L = j\omega L. \tag{2.36}$$

Real contributions to Z_M are regarded as resistors R while imaginary contributions are interpreted as capacitances C or inductances L depending on the position of the adjacent angular frequency ω in the equation.

As an initial step resonator and film are regarded separately according to

$$Z_M = Z_M^R + Z_M^F. \tag{2.37}$$

Thereby, Z_M^R represents the unperturbed resonator while Z_M^F reflects the acoustic load of the film.

2.3.1 Motional Resonator Impedance

The evaluation of the experimental results using the expression for the one-dimensional physical model performed in Section 4.1.3 confirms that the imaginary part of the piezoelectric constant ϵ vanishes. This enables to simplify the following transformation of the motional resonator impedance Z_M^R into an equivalent circuit by setting this parameter to zero. The expansion of Eq. 2.33 for the remaining parameters results in

$$\begin{aligned} Z_M^R = \frac{jd_R}{2A_R e_R^2}\Bigg(&\frac{2e_R^2}{(\omega\varepsilon_R - j\sigma_R)} - d_R\sqrt{\rho_R\left(\frac{\omega e_R^2}{\omega\varepsilon_R - j\sigma_R} + c_{66} + j\omega\eta_R\right)} \\ &\times \cot\left(\frac{\omega d_R}{2}\sqrt{\frac{\rho_R}{\omega e_R^2/(\omega\varepsilon_R - j\sigma_R) + c_{66} + j\omega\eta_R}}\right)\Bigg). \end{aligned} \tag{2.38}$$

The equation is exact within the one-dimensional model but not suited for further discussions.

Simplifications can be applied to the cot-function provided that the acoustic phase shift in the resonator α_R is close to odd multiples of π. The condition is fulfilled for small acoustic loads, i.e. for small derivations of the unperturbed resonance frequency. The condition corresponds to $\alpha_R \approx N\pi$ with N as the harmonic number. Under such conditions the argument of the cot-function can be approximated by [65]

$$\cot\left(\frac{\alpha_R}{2}\right) \approx \frac{N^2\pi^2 - \alpha_R^2}{4\alpha_R}. \tag{2.39}$$

The simplification yields two advantages, the separation of the real and imaginary part of Z_M^R and the explicit introduction of the harmonic number.

At first, the real part $R_M = \mathrm{Re}(Z_M^R)$

$$R_M = \underbrace{\frac{N^2\pi^2 d_R}{8A_R {e_R}^2}\,\eta_R}_{R_\eta} + \underbrace{\frac{(N^2\pi^2 - 8)\,d_R\sigma_R}{8A_R\,(\varepsilon_R{}^2\omega^2 + \sigma_R{}^2)}}_{R_\sigma} \tag{2.40}$$

is discussed. It represents losses and can be interpreted as series of R_η and R_σ. The property therein expected to exhibit the strongest temperature dependence is used as index, respectively. The limits of R_σ for $\sigma \to 0$ and $\sigma \to \infty$ vanish. The maximum in between is found at the so-called dielectric relaxation frequency $\omega_\varepsilon = \sigma_R/\varepsilon_R$. The situation can be illustrated by expressing R_σ as parallel connection $R_\sigma = R_{\sigma+} \parallel R_{\sigma-}$ with

$$R_{\sigma+} = \frac{(N^2\pi^2 - 8)\,d_R}{8A_R{\varepsilon_R}^2\omega^2}\,\sigma_R \tag{2.41}$$

and

$$R_{\sigma-} = \frac{(N^2\pi^2 - 8)\,d_R}{8A_R}\,\frac{1}{\sigma_R}. \tag{2.42}$$

Thereby, $R_{\sigma+}$ increases and $R_{\sigma-}$ decreases with increasing conductivity or temperature. The resistors are part of the equivalent circuit as visualized in Fig. 2.6.

Secondly, the imaginary part of the motional resonator impedance is discussed. From Eqs. 2.38 and 2.39 $X_M = \mathrm{Im}(Z_M^R)$ follows with

$$X_M = -\frac{1}{\omega}\underbrace{\frac{N^2\pi^2 d_R}{8A_R e_R^2}\,c_{66}}_{1/C_c} + \omega\underbrace{\frac{d_R^3}{8A_R e_R^2}\,\rho_R}_{L_\rho} + \underbrace{\frac{\omega\,(8 - N^2\pi^2)\,d_R\varepsilon_R}{8A_R\,(\varepsilon_R^2\omega^2 + \sigma_R^2)}}_{X_\sigma}. \tag{2.43}$$

The expression can be interpreted as series of three elements. The capacitive element $X_c = -1/(\omega C_c)$ as well as the inductive element $X_\rho = \omega L_\rho$ show a

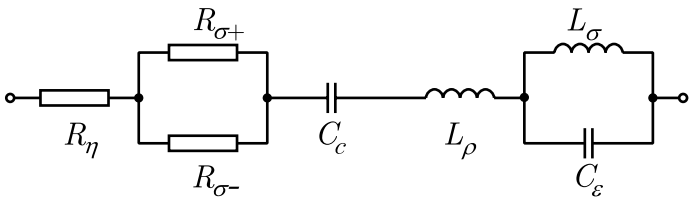

Figure 2.6: Equivalent circuit of the motional resonator impedance Z_M^R.

low temperature dependence with respect to terms containing σ_R. Therefore, the properties which reflects their predominant physical meaning, i.e. the mechanical stiffness c_{66} and the density ρ_R, are chosen as index. The third term X_σ includes σ_R which causes a strong temperature dependence. In order to express the equivalent circuit entirely by lumped elements, X_σ is regarded as a parallel connection $X_\sigma = L_\sigma \parallel C_\varepsilon$ of a capacitance

$$C_\varepsilon = \frac{8A_R\varepsilon_R}{(N^2\pi^2 - 8)\, d_R} \tag{2.44}$$

and an inductance

$$L_\sigma = -\frac{(N^2\pi^2 - 8)\, d_R\varepsilon_R}{8A_R}\,\frac{1}{\sigma_R^2}. \tag{2.45}$$

The capacitance corresponds, except for a constant, to the static capacitance C_S and is, therefore, denoted by the index ε. The term shows a weak temperature dependence. In contrast, the inductance depends strongly on the temperature due to the included conductivity. The arrangement of these elements in the equivalent circuit is shown in Fig. 2.6.

Further, the impact of the resonator parameters on the series resonance frequency f_S is of major interest. The latter property can be determined using Eq. 2.43 with

$$X_M(f_S) = 0. \tag{2.46}$$

The equation yields four solutions for f_S whereas only two of them are real. The positive real solution

$$f_S = \frac{1}{\sqrt{8\rho_R}\,\pi\varepsilon_R d_R}\left(-8\varepsilon_R {e_R}^2 - {d_R}^2\rho_R{\sigma_R}^2 + N^2\pi^2\varepsilon_R\left({e_R}^2 + c_{66}\varepsilon_R\right) + \sqrt{4N^2\pi^2 c_{66}{d_R}^2\varepsilon_R{}^2\rho_R{\sigma_R}^2 + \left(8\varepsilon_R{e_R}^2 + {d_R}^2\rho_R{\sigma_R}^2 - N^2\pi^2\varepsilon_R\left({e_R}^2 + c_{66}\varepsilon_R\right)\right)^2}\right)^{1/2} \tag{2.47}$$

is suited to calculate f_S. The expression contains the electrical conductivity due to the coupling of electrical and mechanical properties as seen e.g. in

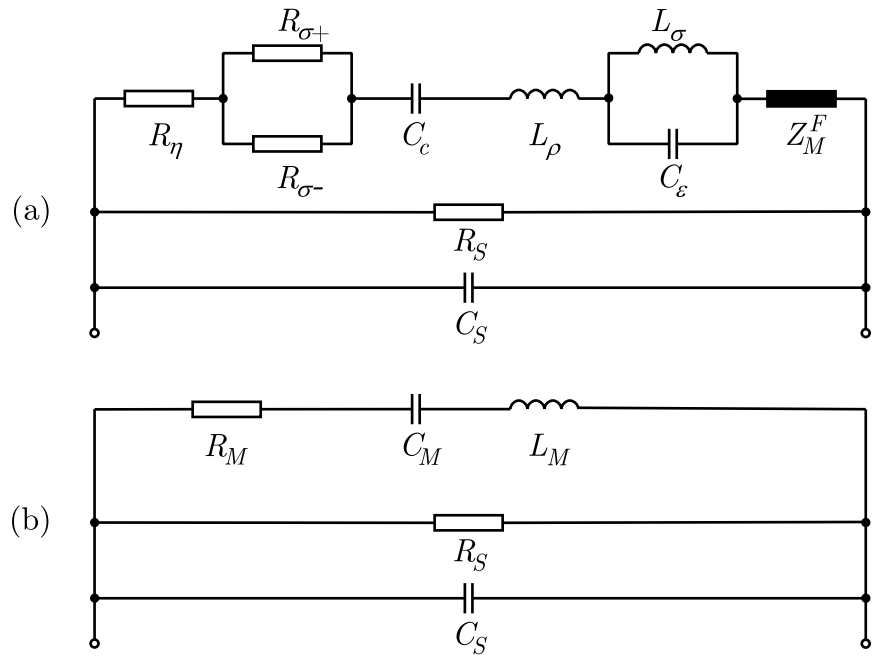

Figure 2.7: Equivalent circuit derived from the physical model (a) and extended Butterworth-van Dyke equivalent circuit (b).

Eq. 2.11. The fact leads, most remarkably, to an impact of the conductivity on the series resonance frequency. Contrary, the viscosity does not impact the resonance frequency which fulfills the expectations.

2.3.2 Motional Film Impedance

In analogy to the approach for the motional resonator impedance, it is attempted to convert the motional film impedance Z_M^F into lumped electrical elements. Thereby, a special case, the resonator coated with a single film according to Eq. 2.35 is chosen. Hence, Z_M^F follows from the difference $Z_M^S - Z_M^R$ and results in

$$Z_M^F = \frac{j\alpha_R d_R}{2\omega A_R K^2 e_R \left(\cot\left(\frac{\alpha_R}{2}\right) + 2\sqrt{\frac{c_R\rho_R}{c_F\rho_F}}\cot(\alpha_F)\right)}. \tag{2.48}$$

The separation of Z_M^F and Z_M^R is illustrated in Fig. 2.7a. Further, the approximations

- For $\cot(\frac{\alpha_R}{2})$ according to Eq. 2.39 and
- $\cot(\alpha_F) \approx \frac{1}{\alpha_F}$ for $\alpha_F \ll 1$ which corresponds to small phase shifts in the film

are applied and result in

$$Z_M^F = \frac{2jd_R}{\omega A_R K^2 e_R \left(\frac{\pi^2 N^2}{\alpha_R^2} + \frac{8}{\alpha_R \alpha_F}\sqrt{\frac{c_R \rho_R}{c_F \rho_F}} - 1\right)}. \tag{2.49}$$

The equation can be expanded by the complex properties K^2, α_R, α_F, c_R and c_F and separated into real and imaginary parts. However, the result is lengthy and not suited either for discussion or transformation into lumped electrical elements. Consequently, the motional film impedance should be handled based on Eq. 2.48.

2.3.3 Butterworth-van Dyke Equivalent Circuit

The equivalent circuit derived here can be used to discuss the impact of the physical properties on the resonance behavior at elevated temperatures. However, the evaluation of experimental results by e.g. fitting the resonance spectra $Z(f)$ with the equivalent circuit is hardly practical due to the large number of lumped elements and their simultaneous dependence from several physical parameters. For example, R_η is governed by η_R and e_R.

Equivalent circuits known for room temperature operation of resonators are relatively simple and suited for routine data evaluation. They are highly attractive to describe the operation of resonators at elevated temperatures provided that minor modifications of their structure and reassignments of their lumped elements to the physical properties lead to reasonable approximations.

The Butterworth-van Dyke equivalent circuit (BvD EC) is well known for piezoelectric resonators operated at room temperature [66, 67]. Here, the motional impedance consists of a series of three elements, namely the resistor R_M, the capacitance C_M and the inductance L_M. The static impedance is simply the capacitance C_S. In order to account for high-temperature effects, the most obvious extension of the BvD EC is the introduction of a bulk resistance R_S which reflects the finite conductivity of the resonator material in analogy to Eq. 2.30. Fig. 2.7b shows the extended BvD EC.

The comparison of the extended BvD EC with the equivalent circuit derived from the physical model as visualized in Fig. 2.7a exhibits some similarities. First of all, the static parts of the impedance are identical. Further, the real part of the motional resonator impedance can be calculated from the arrangement of R_η, $R_{\sigma+}$ and $R_{\sigma-}$ and corresponds to R_M according to Eq. 2.40. Consequently, the extended BvD EC includes losses without further approximations with respect to the equivalent circuit derived from the physical model.

In contrast, the imaginary part of the motional resonator impedance represented by C_c, L_ρ, C_ε and L_σ cannot be transformed into elements of the BvD EC. Approximations are required to express them as series of C_M and

L_M. The parallel arrangement $X_\sigma = L_\sigma \parallel C_\varepsilon$ as given by Eq. 2.43 can be simplified provided that σ_R meets limiting conditions. Thereby, the properties related to low and high temperatures are indexed by additional minus and plus signs, respectively.

- Low temperature: $\sigma_R \ll \varepsilon_R \omega$.
  X_σ becomes capacitive with

$$X_{\sigma-} \approx -\frac{1}{\omega}\frac{1}{C_{\sigma-}} \quad \text{and} \quad C_{\sigma-} = \frac{8A_R}{d_R}\frac{\varepsilon_R}{(N^2\pi^2 - 8)}. \tag{2.50}$$

  Under such circumstances the series connection of C_c and $C_{\sigma-}$ can be transformed into a single capacitance. Consequently, the expressions

$$C_{M-} = \frac{1}{1/C_c + 1/C_{\sigma-}} = \frac{8A_R}{d_R}\,\frac{e_R^2\varepsilon_R}{N^2\pi^2\,(e_R^2 + c_{66}\varepsilon_R) - 8e_R^2}. \tag{2.51}$$

  and

$$L_{M-} = L_\rho = \frac{d_R}{8A_R}\,\frac{d_R^2\rho_R}{e_R^2} \tag{2.52}$$

  connect the parameters of both equivalent circuits and of the physical model. The latter equations do not contain σ_R, i.e. the low temperature approximation is not affected by the conductivity.

- High Temperature: $\sigma_R \gg \varepsilon_R \omega$.
  X_σ becomes inductive with

$$X_{\sigma+} = \omega\ L_{\sigma+} \quad \text{and} \quad L_{\sigma+} = \frac{d_R}{8A_R}\,\frac{(8 - N^2\pi^2)\,\varepsilon_R}{\sigma_R^2}. \tag{2.53}$$

  Thus, the equivalent circuits and the physical model are related by

$$C_{M+} = C_c = \frac{8A_R}{d_R}\frac{e_R^2}{N^2\pi^2}\,\frac{1}{c_{66}} \tag{2.54}$$

  and

$$L_{M+} = L_\rho + L_{\sigma+} = \frac{d_R}{8A_R}\,\frac{(8 - N^2\pi^2)\,\varepsilon_R e_R^2/\sigma_R^2 + d_R^2\rho_R}{e_R^2}. \tag{2.55}$$

Consequently, the extended BvD EC describes the resonance spectra properly as long as the approximations apply. For

$$\sigma_R \approx \varepsilon_R\,\omega, \tag{2.56}$$

however, the structure of the extended BvD EC is incorrect. In this case, the physical model should be applied despite the extensive numeric effort. The applicability of the approximations is discussed in more detail in Sections 3.2.3 and 4.2.3.

The physical model and the corresponding equivalent circuit consider the effect of additional films in form of the motional film impedance Z_M^F. Thus, the extended BvD EC is applicable without further approximation provided that the sum $Z_M^R + Z_M^F$ can be transformed into a series of resistor, capacitance and inductance. Since the motional film impedance is obviously not convertible into lumped elements, the desired transformation cannot be performed. Approximations for small acoustic loads lead to slightly modified BvD parameters and keep the structure of the EC unchanged. Therefore, the BvD approach remains applicable for small acoustic loads.

The subsequent discussion in this section is focussed on the determination of the materials parameters of the resonators. Therefore, additional films are not required. i.e. Z_M^F can be set to zero and the BvD parameters as derived above describe the situation. The electrodes are regarded as infinite thin sheets.

2.3.4 Materials Constants

So far, the electrical elements of the extended BvD EC are expressed as function of the materials properties and dimensions of the resonators. However, the determination of the materials properties by fitting the elements of the BvD EC to the resonance spectra requires their subsequent transformation into the materials properties. Consequently, the materials properties must be expressed as function of the BvD parameters.

In order to proceed further, the resonator properties accessible by this approach have to be identified:

- The geometrical parameters d_R, A_R and the density ρ_R have to be determined by methods as described in Section 4.1.3.
- In general, σ_R cannot be extracted accurately from the resonance spectra. For the langasite resonator devices used here, high resistances occurring below about 700°C prevent the determination of σ_R. Complementary impedance measurements at low frequencies have to be performed. The second bulk parameter ε_R is accessible by such measurements, too.
- The motional physical properties η_R, c_{66} and e_R remain to be calculated from R_M, C_M and L_M. The latter parameters can be determined by fitting the extended BvD EC to the resonance spectra.

In order to calculate η_R, c_{66} and e_R from R_M, C_M and L_M Eqs. 2.40, 2.51 and 2.52 or 2.40, 2.54 and 2.55 for the low or high-temperature approximation, respectively, have to be solved. The result

$$\eta_{R-} = \frac{d_R^2 \rho_R}{N^2\pi^2} \left(\frac{d_R}{8A_R} \frac{(8 - N^2\pi^2)\,\sigma_R}{(\varepsilon_R^2\omega^2 + \sigma_R^2)} \frac{1}{L_{M-}} + \frac{R_M}{L_{M-}} \right), \tag{2.57}$$

$$c_{66-} = \frac{d_R^2 \rho_R}{N^2\pi^2}\left(\frac{d_R}{8A_R}\frac{(8-N^2\pi^2)}{\varepsilon_R}\frac{1}{L_{M-}} + \frac{1}{C_{M-}L_{M-}}\right) \tag{2.58}$$

and

$$e_{R-} = \sqrt{\frac{d_R^3 \rho_R}{8A_R L_{M-}}} \tag{2.59}$$

is obtained directly from the equations mentioned above for low temperatures. The corresponding equations for high temperatures can obviously not solved. However, if R_M is simplified for $\sigma_R \gg \varepsilon_R\omega$

$$R_{M+} = \frac{d_R}{8A_R}\left(\frac{N^2\pi^2-8}{\sigma_R} + \frac{\eta_R N^2\pi^2}{e_R^2}\right) \tag{2.60}$$

the solution

$$\eta_{R+} = \frac{d_R^2\rho_R}{N^2\pi^2}\frac{(8-N^2\pi^2)\,d_R/\sigma_R + 8A_R R_{M+}}{8A_R L_{M+} + (N^2\pi^2-8)\,d_R\varepsilon_R/\sigma_R^2}, \tag{2.61}$$

$$c_{66+} = \frac{d_R^2\rho_R}{N^2\pi^2}\frac{1}{(N^2\pi^2-8)\,/\,(8A_R)\,d_R\varepsilon_R/\sigma_R^2\,C_{M+} + L_{M+}C_{M+}} \tag{2.62}$$

and

$$e_{R+} = \sqrt{\frac{d_R^3\rho_R}{8A_R L_{M+} + (N^2\pi^2-8)\,d_R\varepsilon_R/\sigma_R^2}}. \tag{2.63}$$

is received.

2.4 Resonator Quality Factor

Resonators are commonly evaluated by the quality factor Q (Q-factor) which is defined by the ratio of stored E_S and dissipated energy E_D multiplied by 2π.

$$Q = 2\pi\frac{E_S}{E_D} \tag{2.64}$$

The property reflects the loss and is determinable in different ways such as

- Dissipation factor,
- Equivalent circuit and
- Bandwidth

approach.

2.4.1 Dissipation Factor Approach

The dissipation factor δ is the most fundamental expression for losses. Its tangent is given by the ratio of imaginary and real part of complex quantities. The resonator quality factor Q is closely related according to $\delta = Q^{-1}$.

For the mechanical loss follows immediately

$$Q_c{}^{-1} = \delta_c = \arctan \frac{{c_R}''}{{c_R}'}. \tag{2.65}$$

The separation of the real and imaginary part of the piezoelectrically stiffened shear modulus $\hat{c}_R = c_{66} + e_R^2/\varepsilon_R + j\omega\eta_R$ yields

$$\delta_c = \arctan \frac{2\omega^2\varepsilon_R\epsilon_R\, e_R + \omega^3\varepsilon_R^2\eta_R + \omega\sigma_R\,(\eta_R\sigma_R + e_R^2 - \epsilon_R^2)}{\omega^2\varepsilon_R\,(e_R^2 - \epsilon_R^2) - 2\omega e_R\epsilon_R\,\sigma_R + c_{66}\,(\omega^2\varepsilon_R^2 + \sigma_R^2)}. \tag{2.66}$$

The contributions of the loss related parameters η_R, σ_R and ϵ_R can be discussed separately by setting only one of them to non-zero values. For the viscosity follows

$$Q_{c,\eta}{}^{-1} = \delta_{c,\eta} = \arctan \frac{\omega\varepsilon_R\eta_R}{e_R^2 + c_{66}\varepsilon_R}. \tag{2.67}$$

Introducing the dielectric relaxation frequency $\omega_\varepsilon = \sigma_R/\varepsilon_R$ the conductivity related contribution becomes

$$\begin{aligned} Q_{c,\sigma}{}^{-1} = \delta_{c,\sigma} &= \arctan \frac{{e_R}^2\omega_\varepsilon/\omega}{{e_R}^2 + c_R\varepsilon_R(1 + {\omega_\varepsilon}^2/\omega^2)} \\ &\approx \arctan \frac{{e_R}^2\omega_\varepsilon/\omega}{c_R\varepsilon_R(1 + {\omega_\varepsilon}^2/\omega^2)}. \end{aligned} \tag{2.68}$$

The second line of Eq. 2.68 follows from ${e_R}^2 \ll c_R\varepsilon_R$ which is fulfilled for the materials of interest and indicates a maximum of the conductivity related mechanical loss at $\omega_\varepsilon = \omega$. Beyond that maximum, increasing conductivities (i.e. increasing temperatures) lead to decreasing conductivity related losses. The fact is highly remarkable since a decreasing total loss can be expected with increasing temperature if that contribution dominates.

Finally, the loss related to the imaginary part of the piezoelectric constant results in

$$Q_e{}^{-1} = \delta_{c,e} = \arctan \frac{2\epsilon_R e_R}{{e_R}^2 - \epsilon^2 + c_{66}\varepsilon}. \tag{2.69}$$

According to the experimental results presented in Section 4.1.3 the imaginary part of the piezoelectric constant ϵ_R is found to be zero. Therefore, $Q_{c,\eta}$ and $Q_{c,\sigma}$ are the terms if interest, only.

The dissipation factor approach requires the knowledge of the materials properties which prevents its practical applicability in many cases. Therefore, alternative descriptions of the loss are presented. So far, electrical losses caused by the finite bulk conductivity of the resonator materials are not regarded. However, the following approaches include this property.

2.4.2 Equivalent Circuit Approach

For the conventional BvD EC, i.e. the circuit without the resistor R_S in the static arm, the energy terms

$$E_S = \frac{I_M^2 L_M}{2} \qquad \text{and} \qquad E_D = 2\pi\sqrt{L_M C_M}\,\frac{I_M^2 R_M}{2} \tag{2.70}$$

can be expressed using the parameters of the motional arm and the corresponding current I_M [68] which results in the Q-factor

$$Q_0 = \sqrt{\frac{L_M}{C_M}}\frac{1}{R_M}. \tag{2.71}$$

The recalculation for the extended BvD EC includes additional losses due to the finite bulk resistance R_S according to

$$E_D = 2\pi\sqrt{C_M L_M}\,\frac{I_M^2 R_M}{2} + R_S I_S^2. \tag{2.72}$$

Thereby, I_S denotes the current through the static arm. With

$$I_M R_M = I_S R_S \tag{2.73}$$

follows

$$\begin{aligned} Q =& \frac{1}{\sqrt{L_M C_M}}\frac{L_M I_M^2}{R_M I_M^2 + R_S I_S^2} = \sqrt{\frac{L_M}{C_M}}\frac{1}{R_M}\frac{R_S}{R_S + R_M} \\ =& Q_0 \frac{R_S}{R_S + R_M}. \end{aligned} \tag{2.74}$$

Eq. 2.74 can be applied to calculate Q as long as the approximations for the parameters of the extended BvD EC are valid.

2.4.3 Bandwidth Approach

The Q-factor follows from the bandwidth Δf_S at half maximum of the conductance peak $G_{max}/2$ and the series resonance frequency f_S according to [47, 69]

$$Q = \frac{f_S}{\Delta f_S}. \tag{2.75}$$

The expression is highly attractive because of its model independence. If a Lorentz function

$$G = \frac{2A}{\pi}\frac{\Delta f_S'}{4\left(f - f_S\right)^2 + \Delta f_S'^2} \tag{2.76}$$

is fitted to the data, the width of G squared $\Delta f_S \approx 0.64\Delta f_S'$ can be used to calculate Q. The parameter A reflects the area under the curve is not used in this context.

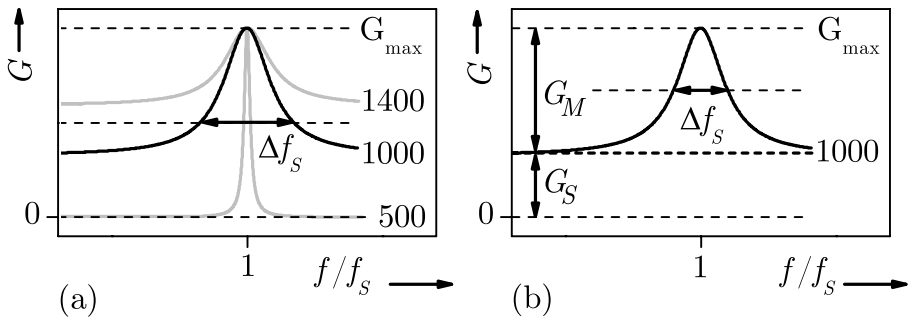

Figure 2.8: Schematic conductivity of a resonator in the vicinity of the resonance frequency and indication of the bandwidth Δf_S. The parameter represents the temperature [°C].

However, the approach is derived for low temperatures where the conductance G of the resonator vanishes except for frequencies in the vicinity of the resonance frequency. Fig. 2.8a illustrates the fact which is even valid at 500°C[8]. Under such circumstances Δf_S can be determined accurately. With increasing temperature Δf_S at $G_{max}/2$ becomes meaningless or indeterminable as visualized in Fig. 2.8a for 1000 and 1400°C, respectively. Consequently, the bandwidth approach must be modified to evaluate losses at high temperatures.

If a resonator is operated at its resonance frequency f_S, the imaginary part of the impedance vanishes. For the extended BvD EC as shown in Fig. 2.7b, the impedance becomes $R_{min} = R_S \,||\, R_M$. The expression is equivalent to $G_{max} = G_S + G_M$. The situation corresponds to the conventional BvD EC if G_S is ignored. Therefore, the bandwidth approach can be applied provided that the baseline of the conductance spectra is moved to G_S as indicated by the heavy dashed line in Fig. 2.8b. Consequently, Δf_S must be determined at $G_S + G_M/2$. The resulting resonator quality factor corresponds to Q_0 in Eq. 2.71. In order to calculate Q using Eq. 2.74, the resistors R_S and R_M remain to be extracted from the conductance plot. Thereby, R_S corresponds to the baseline of the conductance spectra with $R_S = 1/G_S$. R_M follows from $R_M = 1/(G_{max} - G_S)$. Finally, the Q-factor yields

$$Q = Q_0 \frac{G_{max} - G_S}{G_{max}} = \frac{f_S}{\Delta f_S} \frac{G_{max} - G_S}{G_{max}}. \tag{2.77}$$

The properties on the right hand side of Eq. 2.77 can be extracted easily from the spectrum $G(f)$ provided that a Lorentz function with the offset G_S is fitted.

The approach is advantageous since the motional parameters C_M and L_M

[8]The calculation is done using the standard data set for langasite resonators. Details are given in Appendix A.

of the BvD EC do not have to be known. The parallel arrangement of R_S and R_M is the only condition which is, however, undoubtedly valid.

As for the dissipation factor approach, the contributions of the loss related parameters η_R, σ_R and ϵ_R can be separated by setting only one of them to non-zero values.

2.5 Limitations of the Models

The one-dimensional physical model describes the shear vibration of infinite piezoelectric plates exactly. In particular, any acoustic load is reflected by the model. However, finite resonators requires the introduction of an effective area of the mechanical vibration. The approximation is believed to be valid for simple geometries of the resonator device and confirmed for circular resonators and electrodes by the experimental results presented in Chapter 4. Inhomogeneities of the materials, spurious resonances or the energy trapping cannot be regarded by the current approach.

So far, continuum-mechanical phenomena are described which does not give any atomistic insight about transport processes or loss mechanisms in the resonator or film materials. However, the description of the resonator devices is the base for the extraction of accurate materials data which help to create microscopic models as presented in Part II.

The expressions introduced here include at most one layer on each side of the resonator. The corresponding layer sequences as given by Eqs. 2.33–2.35 reflect situations of practical relevance and are suited to describe the experimental results of this work. For example, the determination of the materials properties of the resonators incorporates the impact of the electrodes using the appropriate layer sequence. Additional layers which would reflect the viscous damping due to surrounding gases are ignored. The approximation is justified by the dominating intrinsic loss of the resonator materials at elevated temperatures.

It should be noted that multilayer systems does not require new physical approaches. A Transfer matrix can be used to describe such situations [70].

Equivalent circuits simplify the handling and interpretation of the resonance spectra at the expense of further approximations. In particular, the model is restricted to small acoustic loads.

Chapter 3

Parameter Study

Crucial physical properties with respect to high-temperature operation of the resonators must be identified. For that purpose, the impact of the physical properties on the resonance frequency and the resonator quality factor is calculated.

The materials data used for the following parameter study correspond to some extend to those of langasite. They are extrapolated to 1400°C in order to extend the calculations to extremely high temperatures which are not experimentally accessible because of the limited stability of the thin film electrodes applied here. Further, single activation energies for the conductivity σ_R and the viscosity η_R are assumed. For comparison, room temperature data of $GaPO_4$ and quartz are included. Finally, dimensions of standard resonators according to Appendix A are used. The details about the materials data used here are summarized in Appendix A.

3.1 One-dimensional Physical Model

3.1.1 Features of the Resonance Spectra

Resonance spectra in form of the impedance modulus $|Z(f)|$ and the phase angle $\varphi(f)$ are calculated from Eq. 2.32. Thereby, room temperature data of the 5 MHz standard langasite resonator are used. The resonance frequency and and the antiresonance frequency are clearly visible in Fig. 3.1 by the minimum $f(|Z|_{min})$ and maximum $f(|Z|_{max})$ of the impedance modulus, respectively. The series resonance frequency f_S is found at the maximum of the conductance $f_S = f(G_{max})$ and close to the resonance frequency. A similar statement holds true for the parallel resonance frequency f_P which is located at the maximum of the resistance $f_P = f(R_{max})$. Its value is close to the antiresonance frequency. Further, the phase φ vanishes at f_S and f_P which corresponds to a vanishing imaginary part of Z.

The damping of the vibrations is fairly low at room temperature. The fact becomes obvious by very pointed peaks of $|Z(f)|$ and the nearly rectangular

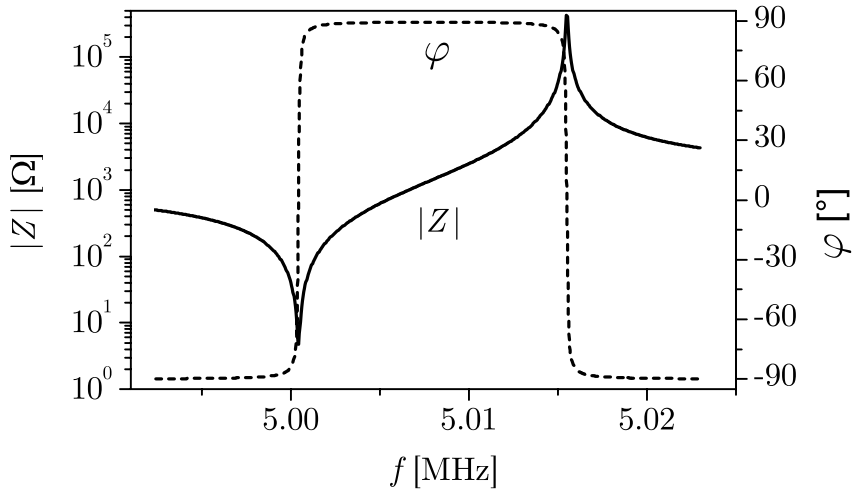

Figure 3.1: Impedance modulus $|Z|$ and phase angle φ calculated based on the one-dimensional physical model.

$\varphi(f)$ characteristics with a very steep slope at the two zero phase frequencies. Further, the minimum value of $|Z|_{min}$ is an approximate measure of the loss, i.e. small values reflect low losses.

The general temperature dependence of the resonance behavior can be visualized from the spectra themselves. The resonance shifts to lower frequencies with increasing temperature as shown in Fig. 3.2 and 3.3 for langasite. At elevated temperatures, i.e. at 1000 and 1400°C, high damping leads less pronounced, flatter peaks in $|Z(f)|_{min}$ and to a rounder shape of $\varphi(f)$. The anti-resonance peak vanishes which is a highly remarkable feature.

As shown in the next section the series resonance frequency f_S is independent of the stray capacitance and, therefore, generally preferred for frequency determination. This advantage justifies the closer inspection of the conductance G since it is used to determine f_S. In addition, G is a nearly symmetric function with respect to f_S and can be described by e.g. a Lorentz function [69, 71]. Consequently, routine data evaluation can be performed model independent using G. Fig. 3.4 shows the conductance of the data sets already used for Figs. 3.2 and 3.3. As for the impedance modulus the peak becomes broadened with increasing temperature. Nevertheless, the series resonance frequency remains clearly observable up to 1400°C for the spectra calculated from the one-dimensional physical model.

3.1.2 Series Resonance Frequency

The frequency of resonators is their key operation characteristics. If such devices are regarded as sensor platform, environmental independent operation is required. However, the materials properties included in the physical

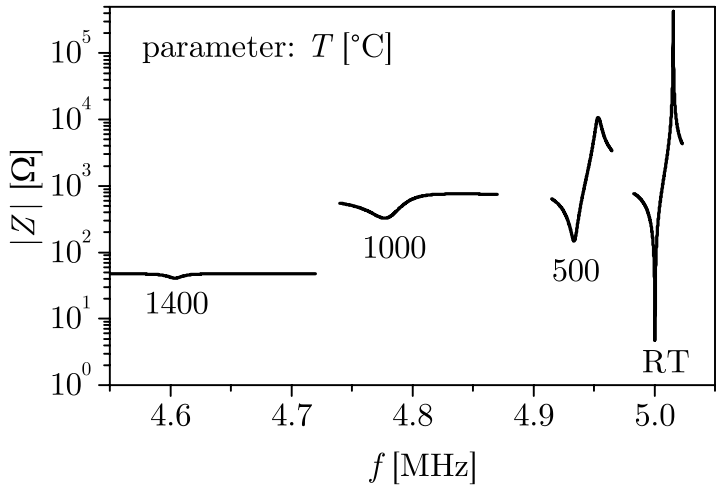

Figure 3.2: Impedance modulus of the standard langasite resonator calculated for different temperatures.

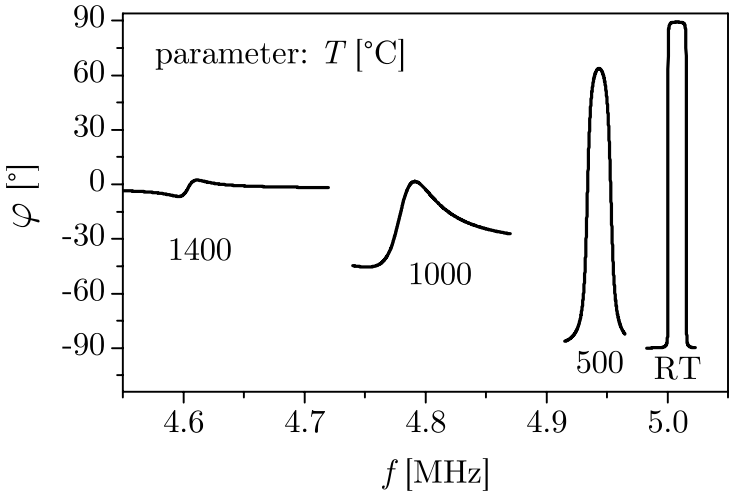

Figure 3.3: Phase shift of the standard langasite resonator calculated for different temperatures.

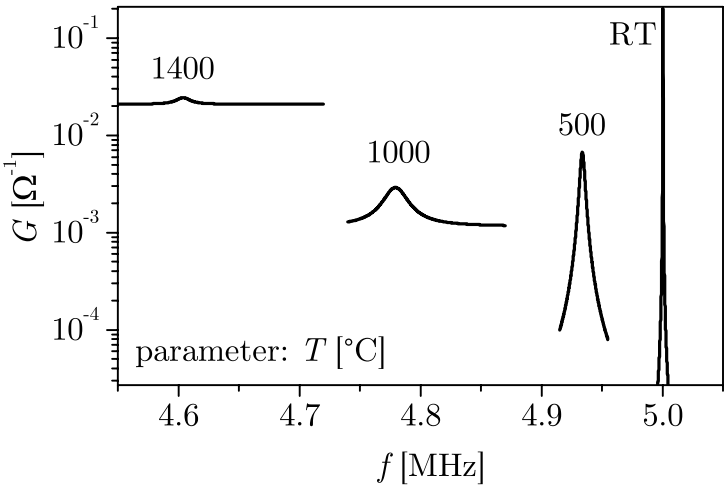

Figure 3.4: Conductance of the standard langasite resonator calculated for different temperatures.

model exhibit, in general, a dependence from the environmental conditions and may cause a frequency shift. The same holds true for the resonator holder capacitance and the electrode diameter[1]. Consequently, parameters which are potentially responsible for large frequency shifts have to be identified and investigated in detail. This section is the initial point where the impact of these parameters on the series resonance frequency f_S is calculated systematically. For completeness, the effect of films is considered in the same fashion. Here, large frequency shifts points to film properties which are attractive for sensor purposes.

The following part of the parameter study is carried out for the 5 MHz standard resonator wearing identical films on both sides of 1 μm thickness. The stiffness and density of the films correspond to those of titania as given in Appendix A.

The parameter study bases on Eq. 2.34 which is used to calculate spectra $G(f)$ and $R(f)$. The series resonance frequency f_S and the parallel resonance frequency f_P are obtained with a numerical accuracy of 10^{-6} Hz from the respective maximum. Further, the derivatives of these frequencies $\partial f/\partial\,[..]$ for all parameters [..] being included in the physical model[2] are calculated and multiplied by $[..]/f$. The approach results in relative values of the derivatives $\kappa_{[..]}$

$$\kappa_{[..]} = \frac{[..]}{f}\frac{\partial f}{\partial [..]} = \frac{[..]}{f}\frac{\Delta f}{\Delta [..]} \tag{3.1}$$

[1]Additional films showing environmental dependent conductivities may alter the electrode diameter.

[2]The parameters are $d_R, A_R, A_E, c_{66}, \eta_R, \epsilon_R, \sigma_R, \rho_R, d_F, c_F, \eta_F, \rho_F, C_L and R_L$.

which enables their comparison. The right hand side of Eq. 3.1 is written using small differences in order to relate relative changes of the frequency to that of the parameters [..] by $\kappa_{[..]}$

$$\frac{\Delta f}{f} = \kappa_{[..]} \frac{\Delta [..]}{[..]}. \tag{3.2}$$

The meaning of Eq. 3.2 becomes obvious taking the thickness of the resonator as example, i.e. $[..] = d_R$. Its change Δd_R can be related to a mass change Δm by $\Delta d_R / d_R = \Delta m / m$ which results in

$$\frac{\Delta f}{f} = \kappa_{d_R} \frac{\Delta m}{m}. \tag{3.3}$$

Since the subsequent numerical calculation yields $\kappa_{d_R} = -1$, the example corresponds to the Sauerbrey equation [64]

$$\frac{\Delta f}{f} = - \frac{\Delta m}{m} \tag{3.4}$$

which is the first order approach to relate relative changes in mass and frequency. In summary, Eq. 3.2 can be regarded as a kind of generalized Sauerbrey equation for the corresponding physical property or dimension of the resonator.

Fig. 3.5 shows values for $\kappa_{[..]}$ calculated from the series resonance frequency f_S. The signs of the changes are indicated in the plot. This calculation is performed for langasite, $GaPO_4$ and quartz at room temperature. Obviously, these piezoelectric materials exhibit a similar behavior. The impact of the resonator properties on the series resonance frequency can be summarized as follows:

- Changes in thickness d_R, shear modulus c_{66} and density ρ_R influence f_S predominantly.
- The piezoelectric coefficient e_R and the dielectric constant ε_R show a little impact, only.
- The effective resonator area A_R, the effective electrode area A_E, the viscosity η_R and the conductivity σ_R do not affect f_S at room temperature.

The influence of the film properties on the piezoelectric resonators made of different materials is also similar.

- Changes in thickness d_F and density ρ_F dominate.
- The shear modulus c_F and the viscosity η_F does not affect f_S under the conditions chosen here.

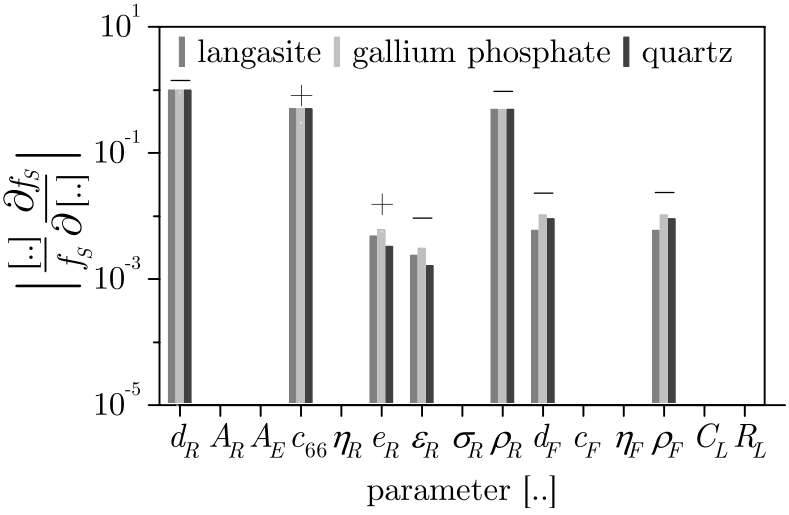

Figure 3.5: Relative derivatives of the series resonance frequency for the parameters of the resonator device calculated for different materials at room temperature.

Finally, it should be noted that the stray capacitance C_L and the lead resistance R_L have no impact on f_S. Since the piezoelectric materials behave in a similar fashion, the calculation is continued using the standard materials parameters of langasite.

The situation changes for some parameters if the parallel resonance frequency f_P is regarded. As visualized in Fig. 3.6, A_R, A_E and especially C_L influence that frequency. The values for f_S are given for comparison purposes and correspond to those in Fig 3.5 for langasite. Some sensor applications may take advantage of the electrode area dependent parallel resonance frequency [72] while the impact of the stray capacitance generally disturbs the frequency determination. Therefore, f_P is seen as hardly useful resonance property.

The most important issue in the context of this work concerns the relative frequency shift at elevated temperatures. Thereby, special attention has to be drawn to loss related properties, i.e. η_R and σ_R. Fig. 3.7 shows remarkable features for changes in f_S at 500 and 1000°C:

- The impact of the conductivity σ_R becomes pronounced at 1000°C.
- The sign of the relative deviation of ε_R changes going from 500 to 1000°C.
- The effect of the film properties remains almost unchanged.

So far, relative derivatives of the frequency are calculated and compared. If the focus is drawn exclusively on the resonator, d_R, c_{66} and ρ_R cause the strongest impact. In order to identify the dominant parameters for *absolute* frequency changes according to $\Delta[..]\partial f_S/\partial[..]$, the magnitude of environmen-

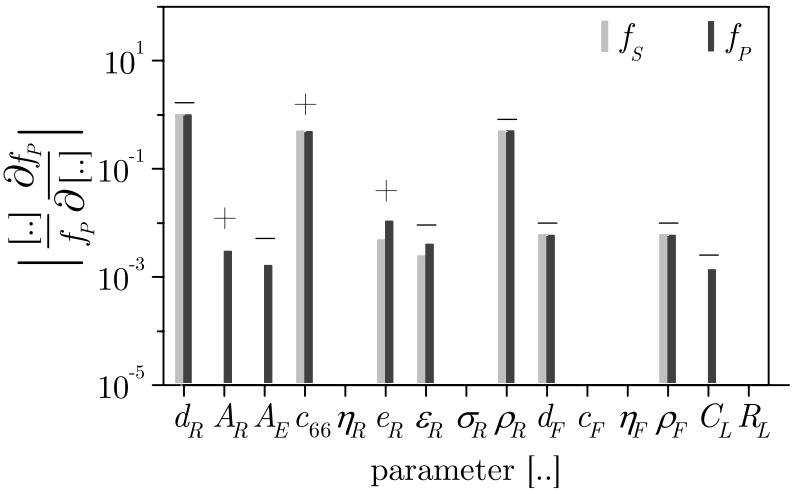

Figure 3.6: Relative derivatives of the series and parallel resonance frequency for the parameters of the resonator device calculated for langasite at room temperature.

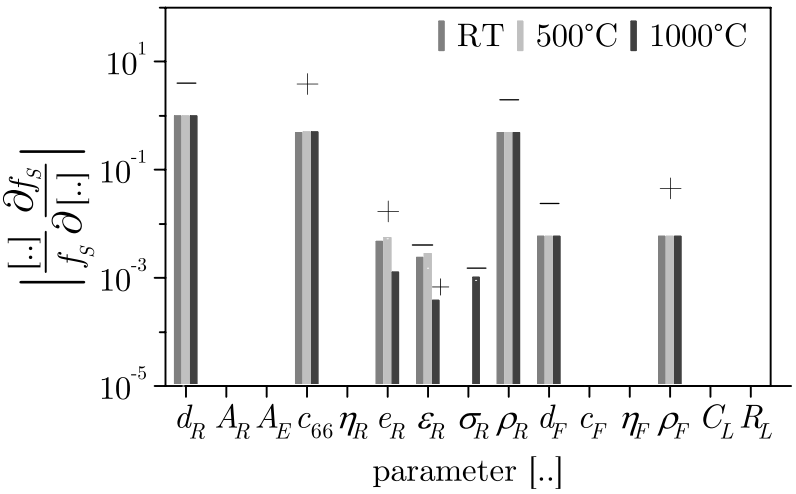

Figure 3.7: Relative derivatives of the series resonance frequency for the parameters of the resonator device calculated for langasite at different temperatures.

tally dependent variations of the corresponding parameter $\Delta[..]$ must be considered. Thereby, the temperature is expected to cause the strongest impact. Since the conductivity σ_R and the viscosity η_R are commonly thermally activated, they might be subject to changes by several orders in magnitude. In contrast, the parameters d_R, c_{66} and ρ_R are expected to show a relatively weak temperature dependence. The conclusion is that changes in σ_R potentially govern the resonance frequency even if its relative derivative κ_σ is smaller than that for d_R, c_{66} and ρ_R.

In summary, d_R, c_{66}, ρ_R and σ_R are identified as the most relevant properties for stable, i.e. environmental independent, operation of resonators at its series resonance frequency at elevated temperatures. Consequently, the dependence of these parameters from the environmental conditions must be studied in detail.

3.1.3 Resonator Quality Factor

Further, the impact of the materials parameters on the resonator quality factor is of particular interest. Conductance spectra according to Eq. 2.33 are evaluated to get Q_{BW}. Its derivatives $\partial Q/\partial [..]$ for the parameters [..] are calculated and multiplied by $[..]/Q$ to get $\nu_{[..]}$

$$\nu_{[..]} = \frac{[..]}{Q}\frac{\partial Q}{\partial [..]} = \frac{[..]}{f}\frac{\Delta f}{\Delta [..]}. \tag{3.5}$$

which allows to relate relative changes

$$\frac{\Delta Q}{Q} = \nu_{[..]}\frac{\Delta [..]}{[..]}. \tag{3.6}$$

The numerical approach corresponds to that for f_S and f_P in Section 3.1.2.

Fig. 3.8 shows the result of the calculation for langasite, $GaPO_4$ and quartz at room temperature. The sign of the changes is indicated in the plot. The most obvious result is the dominance of d_R, c_{66}, η_R, e_R and ρ_R. In contrast, A_R, A_E, ε_R and σ_R do not influence Q.

The behavior at high temperatures is calculated taking langasite as example. The most remarkable result is the increased impact of A_R, A_E, e_R, ε_R and σ_R at 1000°C as seen in Fig. 3.9.

The comparison of ν_η and ν_σ with the other dominant parameters shows differences smaller than one order of magnitude, only. The fact must be discussed in concert with the expected changes in the corresponding parameters. Again, d_R, c_{66}, e_R and ρ_R undergo relatively small changes in a wide temperature range. On the other hand, η_R and σ_R exhibit changes of some orders in magnitude. Therefore, the latter parameters are expected to affect Q predominantly. The result meets the expectations since η_R and σ_R are introduced to reflect losses.

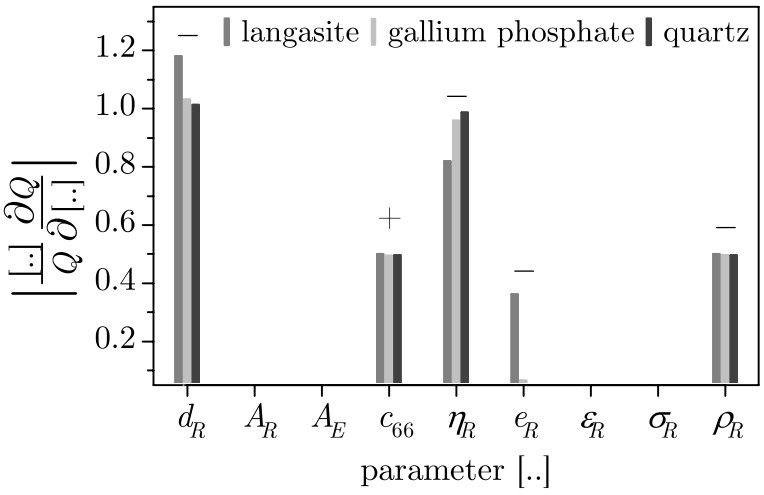

Figure 3.8: Relative derivatives of the resonator quality factor for the parameters of the resonator device calculated for 5 MHz standard resonators of different materials at room temperature.

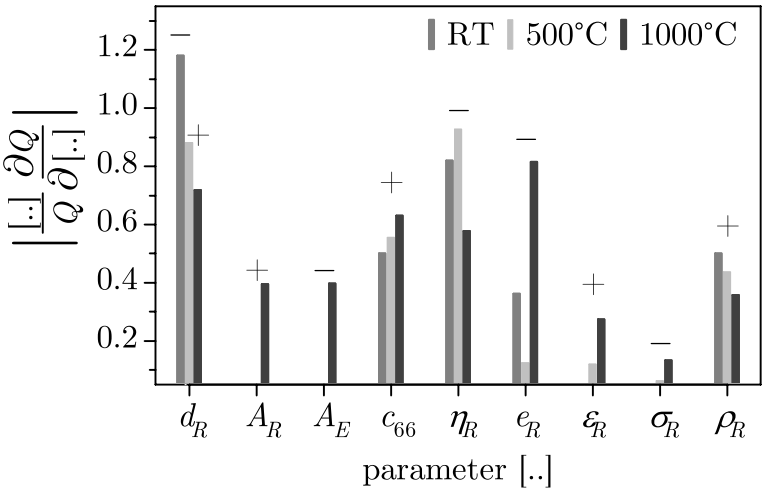

Figure 3.9: Relative derivatives of the resonator quality factor for the parameters of the resonator device calculated for 5 MHz standard langasite resonator at different temperatures.

3.2 Equivalent Circuit Model

3.2.1 Temperature Dependence of the Parameters

The following part of the parameter study is exclusively focussed on the impact of the temperature dependent conductivity and viscosity on the elements of the equivalent circuit visualized in Fig. 2.7a. For that purpose, the idealized temperature dependencies of both properties showing a single activation energy are used. The remaining parameters A_E, A_R, d_R, e_R, c_{66} and ε_B are regarded as temperature independent and set to the values of the standard langasite resonators at room temperature.

The temperature dependent values of the real elements of the motional arm R_η and R_σ (or $R_{\sigma+}$ and $R_{\sigma-}$) for an 1 MHz resonator operated in the fundamental mode, i.e. for $N = 1$, are shown in Fig. 3.10. $R_{\sigma+}$ increases while $R_{\sigma-}$ decreases with temperature which leads to a maximum of R_σ. The fact is highly remarkable since the expression implies decreasing losses with increasing temperature above a certain temperature. However, the statement must be seen in the context of the entire equivalent circuit. Other properties may overwhelm the decreasing values of R_σ. Further, Fig. 3.10 shows the temperature dependence of the overall motional resistance R_M. For the materials data and resonator dimensions chosen here the following statements can be derived:

- R_M is dominated by the viscosity in the low and high temperature range while the conductivity governs the intermediate temperature range. The peak slightly above 700°C indicates the center of the latter range. Its position is defined by the dielectric relaxation frequency with 1 MHz$\times 2\pi = \omega_\varepsilon(719°\text{C})$.
- In the intermediate temperature range R_M and, thereby, the loss can be lowered by decreasing the conductivity σ_R.
- The temperature dependence of R_M does not reflect the activation energy of a single property such as σ_R or η_R.

Fig. 3.11 shows the impact of the resonance frequency on R_M, R_σ and R_η. Two crucial facts can be derived:

- The maximum of R_σ shifts with increasing frequency to higher temperatures. Again, its position is defined by the dielectric relaxation frequency. This shift applies also for R_M as long as R_σ impacts R_M significantly.
- The contribution of R_σ to R_M decreases with increasing frequency. Above about 25 MHz R_σ plays an insignificant role.

The overall resistance of the resonator R can be calculated according to $R = R_S \parallel R_M$ if the resonator is operated at its series resonance f_S. Under

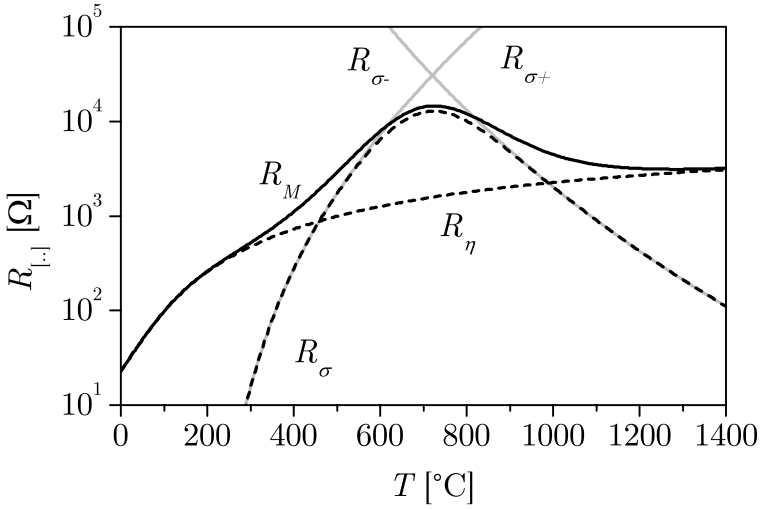

Figure 3.10: Temperature dependent values of the resistors of the motional arm for an 1 MHz standard resonator operated in the fundamental mode.

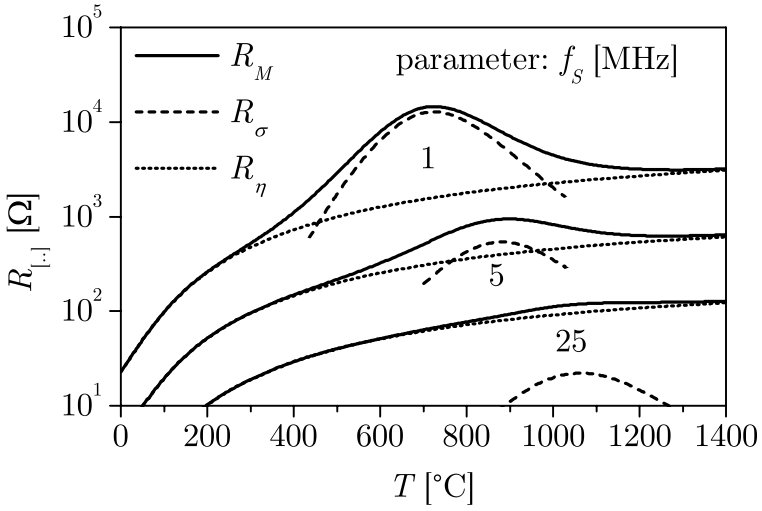

Figure 3.11: Temperature dependent values of R_M, R_σ and R_η for 1, 5 and 25 MHz resonators operated in the fundamental mode.

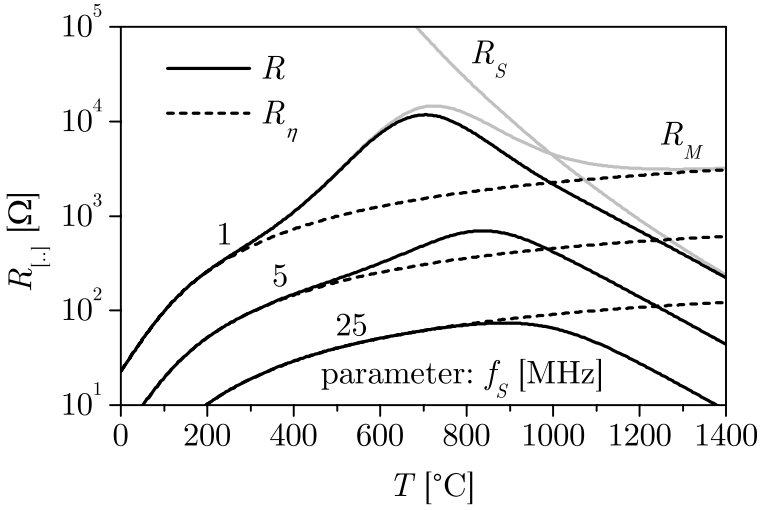

Figure 3.12: Temperature dependent overall resistance R and viscosity related resistance R_η for standard resonators of different frequencies. In addition, the resistance of the static R_S and motional arm R_M are given for the 1 MHz resonator.

such circumstances the imaginary part of Z_M vanishes. Fig. 3.12 shows exemplarily the corresponding curves for $f_S = 1$ MHz. Further, the overall resistance R and the viscosity related resistor R_η are compared in Fig. 3.12 for $f_S = 1$, 5 and 25 MHz. The following conclusions concerning the impact of R_S and R_η can be drawn:

- The static resistance R_S influences the overall resistance R at high temperatures, only.
- The overall resistance decreases with increasing frequency. The fact must be related to the decreased thickness of the resonators at high frequencies and is not necessarily an indication for decreased losses.

Since the static resistance does not change the overall resistance fundamentally, the statements about R_M from above remain true for R.

Furthermore, the impact of the overtone number N is calculated and shown in Fig. 3.13. The plot indicates a clear increase in the overall resistance R and a shift of its maximum to lower temperatures with increasing N. The difference between the fundamental mode ($N = 1$) and the 1^{st} overtone ($N = 3$) is much bigger than the differences between higher overtones.

The temperature dependent values of the imaginary elements of the motional arm X_c, X_ρ and X_σ can be discussed by setting the series resonance frequency of the standard langasite resonator to $f_S = 5$ MHz. Fig. 3.14 shows X_σ as function of temperature under that condition. X_σ undergoes changes around 700°C. Below about 600°C, $\varepsilon_R\,\omega$ dominates with respect to

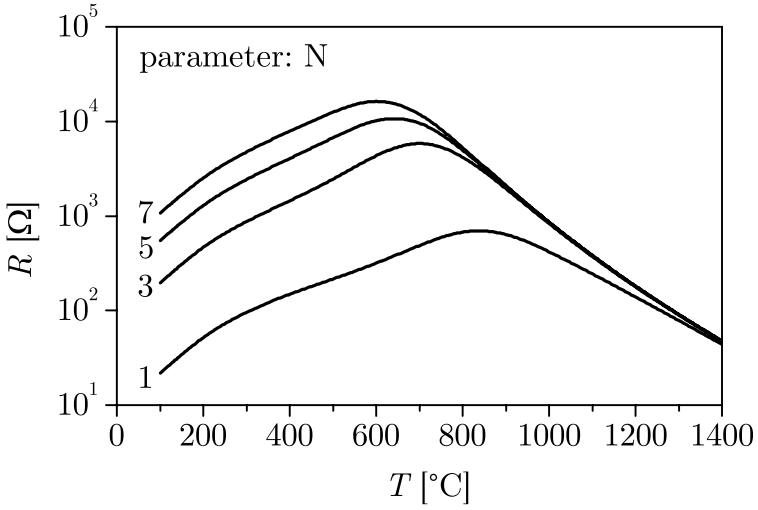

Figure 3.13: Temperature dependent overall resistance for a 5 MHz standard langasite resonator operated at different overtones.

σ_R. Consequently, X_σ is nearly constant. Above about 800°C, σ_R is dominant and X_σ approaches zero. These conclusions also follow from Eq. 2.43 where the limits of X_σ for $\sigma \to 0$ and $\sigma \to \infty$ result in $X_\sigma = const$ and $X_\sigma = 0$, respectively. For completeness, the remaining part of X_M, i.e. the sum $X_c + X_\rho$, is also shown in Fig. 3.14.

Further, the impact of σ_R on the series resonance frequency f_S is calculated as function of temperature according to Eq. 2.47. The curves in Fig. 3.15 result for $f_{RT} = 1$, 5 and 25 MHz applying again the idealized temperature dependence of σ_R according to Fig. A.2 and fixed values for A_E, A_R, d_R, e_R, c_{66} and ε_B. Thereby, the data are normalized using the series resonance frequency at room temperature f_{RT}. The series resonance frequency of the 5 MHz resonator drops above about 700°C. It is not surprising that the changes in frequency and in X_σ are correlated as it becomes obvious by comparing the curves for $f_S = 5$ MHz in Fig. 3.15 with that for X_σ in Fig. 3.14. Further, the frequency drop starts with increasing frequency at higher temperatures.

Finally, the impact of the overtone number N is evaluated and shown in Fig. 3.16. Below about 1000°C, the difference between the fundamental mode ($N = 1$) and the 1^{st} overtone ($N = 3$) is much bigger than the differences between higher overtones. The observation corresponds to that for the overall resistance R in Fig. 3.13.

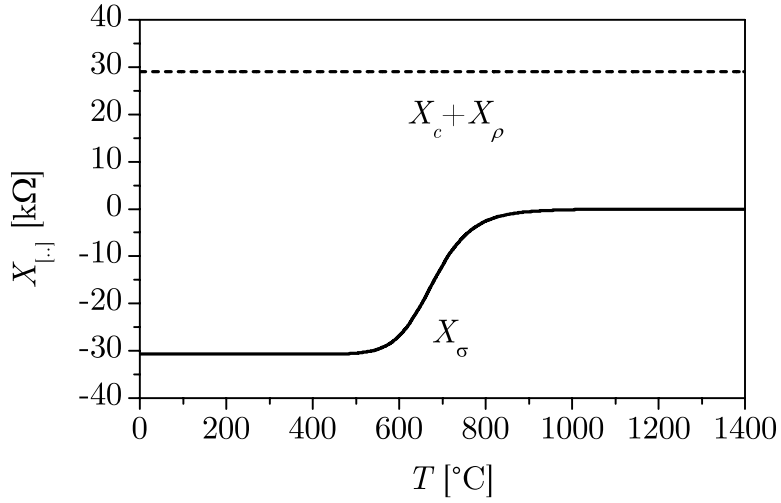

Figure 3.14: Temperature dependent imaginary elements of the motional arm for a 5 MHz standard langasite resonator.

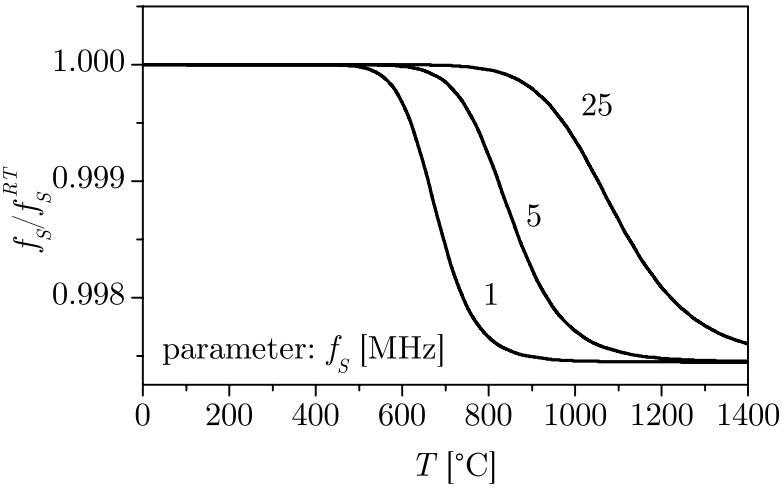

Figure 3.15: Impact of the temperature dependent bulk conductivity on the series resonance frequency for standard langasite resonators of 1, 5 and 25 MHz.

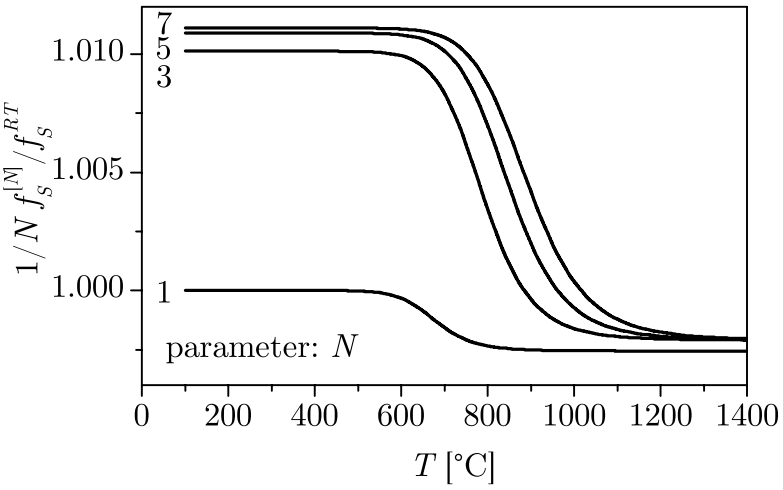

Figure 3.16: Temperature dependent series resonance frequency for a 5 MHz standard langasite resonator operated at different overtones.

3.2.2 Iso-Q Lines

Fig. 3.17 shows iso-Q lines in the log(R_M)-log(R_S) plane in order to visualize the influence of R_M and R_S. Thereby, the values for C_M and L_M are calculated from the room temperature materials data of the standard langasite resonator according to Eqs. 2.51 and 2.52. The plot allows to estimate whether the static resistance R_S has a significant influence on the resonance behavior. Q is independent of R_S for values above the dashed line, i.e. above about $R_S \approx 10^4\ \Omega$ or $\sigma_R \approx 1.4 \times 10^{-3}$ S/m for the standard langasite resonators.

3.2.3 Validity of the Equivalent Circuit

In the following the validity range of the approximations leading to the extended BvD EC is discussed by comparing the resonance spectra obtained from the one-dimensional physical model and from the extended BvD EC. Thereby, the impedance modulus is calculated using the standard data set of the 5 MHz langasite resonator given in Appendix A.

The one-dimensional physical model yields $|Z|$ directly whereas the approximations $|Z_-|$ and $|Z_+|$ are received in two steps, namely

- The calculation of the BvD parameters R_M, C_{M-}, L_{M-} and R_{M+}, C_{M+}, L_{M+} for the low and high approximation, respectively, and
- Their transformation into the impedance according to the circuit given in Fig. 2.7b. Thereby, the motional film impedance Z_M^F is set to zero.

The results of the calculations for room temperature, 500, 1000 and

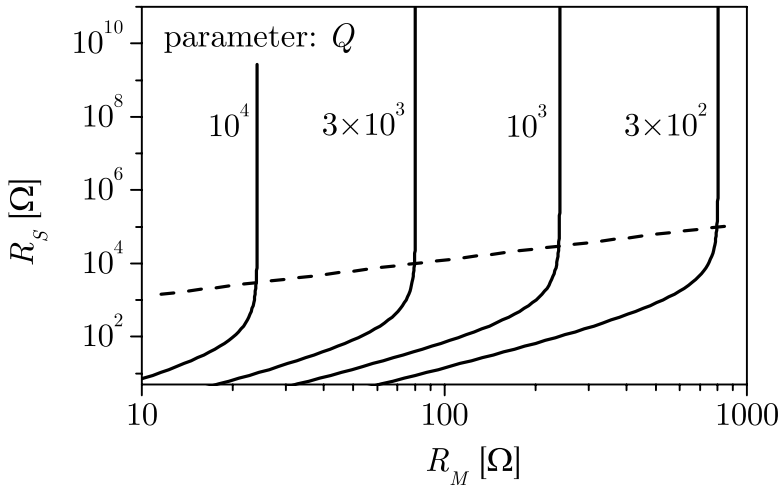

Figure 3.17: Calculated Iso-Q lines as function of the motional R_M and static R_S resistance for the 5 MHz standard langasite resonator.

1400°C are summarized in Fig. 3.18. The gray curves represent the reference data $|Z|$ since they are calculated using the physical model[3]. The dashed and the solid black lines stand for the low and high-temperature approximation, respectively. The spectra calculated from the BvD EC agree with that from the physical model at room temperature, 500 and 1400°C as clearly visible in the figure. In contrast, $|Z_-|$, $|Z_+|$ and $|Z|$ disagree at 1000°C. The latter is reasonable since the extended BvD EC is expected to be incorrect for $\sigma_R \approx \varepsilon_R \omega$. This condition corresponds to $\sigma_R = 5 \times 10^{-3}$ S/m at 5 MHz or to a temperature of about 1000°C according to the conductivity data for langasite presented in Chapter 4.

In order to show the differences more clearly, $|Z_+|$ and $|Z|$ are enlarged in the inlay of Fig. 3.18 for 1000°C. The shape of $|Z_+|$ does not reflect the reference data. The attempt to fit $|Z_+|$ would lead to large numbers for the sum of the squared differences of data and fit function, i.e. to a poor fit quality. In contrast, $|Z_-|$ is shifted along the frequency axis, only. A modification of C_M by 0.65 % results in a an agreement between $|Z_-|$ and $|Z|$ as visualized by the dashed line in the inlay.

From these calculation can be concluded that

- The low- and high-temperature approximations correspond very well to the physical model and are, therefore, suited to extract the materials properties from the parameters of the extended BvD EC,
- Both approximations are not suited for $\sigma_R \approx \varepsilon_R \omega$ which requires the use of the physical model under such circumstances and

[3]These data are the same as in Fig. 3.2

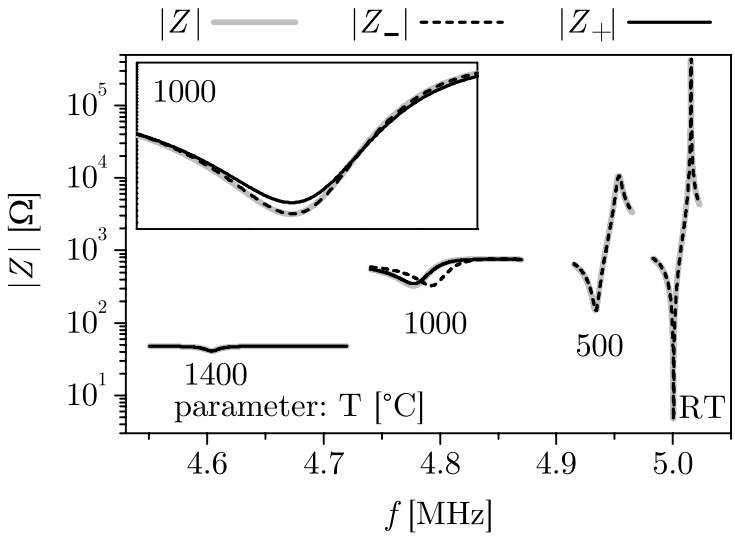

Figure 3.18: Impedance modulus calculated from the one-dimensional model $|Z|$ and the extended BvD EC for the high $|Z_+|$ and low $|Z_-|$ temperature approximation for the 5 MHz standard resonator at different temperatures.

- The low-temperature approximation describes the data properly if insignificantly false values for C_M are acceptable.

3.2.4 Band Width and Equivalent Circuit Approach

The resonator quality factors resulting from the band width approach and the extended BvD equivalent circuit are compared. In contrast to Section 3.2.1, the temperature dependence of all properties of the 5 MHz standard langasite resonator are used for the calculation. The parameters of the EC required to evaluate Eq. 2.74 follow from Eqs. 2.29, 2.30, 2.40, 2.51, 2.52, 2.54, 2.55 and 2.60. Thereby, the results for the low and high-temperature approximation are denoted by Q_{BvD-} and Q_{BvD+}, respectively. The quality factor Q_{BW} of the band width approach follows from Eq. 2.77. The required parameters are extracted from $G(f)$ spectra calculated by Eq. 2.33.

Fig. 3.19 summarizes the results. Thereby, Q_{BvD-} and Q_{BvD+} are shown below and above 1000°C, respectively. Up to about 1000°C and above about 1100°C, the corresponding EC approximation fits very well to Q_{BW}. However, the apparent agreement of Q_{BvD-} and Q_{BW} between about 900 and 1000°C must be seen in the context of the slightly false values of C_M as discussed in Section 3.2.3. In other words, the EC approach can be applied except for the temperature range from 900 to 1100°C which corresponds to $\sigma_R \approx \varepsilon_R \omega$.

Further, the mechanical loss contribution Q_c is shown in Fig. 3.19. It clearly dominates the overall loss up to about 750°C. Above that temper-

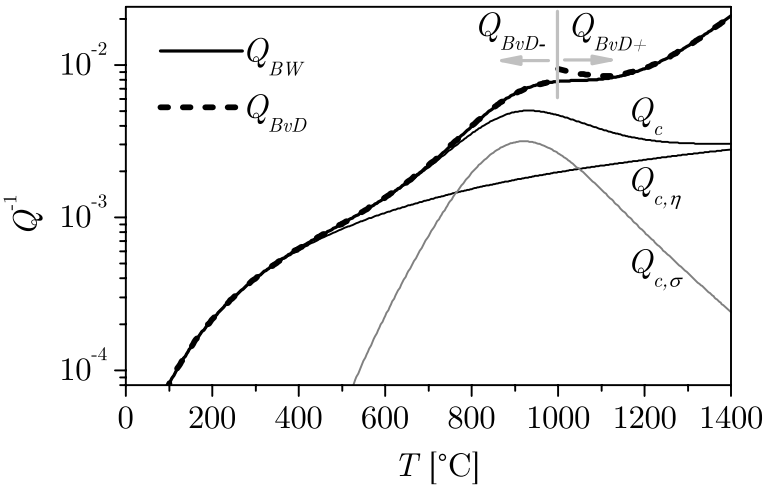

Figure 3.19: Temperature dependent resonator quality factor of a 5 MHz standard langasite resonator according to the bandwidth and the BvD EC approach.

ature, electrical losses caused by the bulk conductivity increasingly impact the overall loss. The separate contributions from η_R and σ_R to the mechanical loss are also shown and denoted by $Q_{c,\eta}$ and $Q_{c,\sigma}$, respectively. Their slope corresponds to that of R_η and R_σ in Fig. 3.10. The viscosity related contribution $Q_{c,\eta}$ dominates up to about 500°C.

Since the band with approach describes the loss properly in the entire temperature range it is recommended to apply it for data evaluation. Nevertheless, the BvD EC approach is suited to discuss the impact of the materials parameters on the resonance properties.

The materials parameters and the dimensions applied so far reflect the properties of langasite resonators to some extent and represent the case where the viscosity and the conductivity determine the overall resistance in different temperature ranges. Other resonator materials and dimensions may lead to an altered predominance of these properties. For example, $GaPO_4$ exhibits a lower conductivity than langasite which results potentially in the dominance of the effective viscosity up to high temperatures.

In the following sections the terms R_M, C_M and L_M, are used, only. The additional index, i.e. the minus and plus sign, is skipped to avoid repeated references on the low- and high-temperature approximation. Of course, the appropriate expressions have to be applied for actual calculations.

Chapter 4

Materials Properties

The following sections present and discuss the materials parameters of quartz, $GaPO_4$ and langasite at temperatures up to 540, 930 and 1050°C, respectively. Thereby, the temperature limit of the langasite resonator devices is determined by the stability of the platinum electrodes. Tolerable degradation within the period of measurement is found up to the temperature mentioned above, only. The maximum examination temperature of the $GaPO_4$ and quartz devices is already close to the phase transformation of these materials.

The resonance spectra of the piezoelectric resonators are determined by recording the real R and imaginary X parts of the impedance spectra in the vicinity of the resonance frequency. The measurements are performed in air and explained in more detail in Appendix C.3.

The description of the TSM resonators presented so far enables the direct determination of the materials properties by fitting the solution of the one-dimensional physical model to the resonance spectra. Alternatively, the parameters of the BvD EC can be determined from the resonance spectra and converted into the materials properties. Both approaches are applied and compared.

Resonator properties of direct relevance to applications such as the mass sensitivity and the temperature compensation are discussed in Chapter 5.

4.1 Fit Procedure

4.1.1 General Approach

For the further discussion it is advantageous to arrange the parameters of the resonators in groups which are

- The sample holder properties
  - C_L, R_L and

- The dimensions of resonator and film
  - d_R, d_F, A_E, A_R,
- The materials properties of the film
  - c_F, ρ_F, η_F,
- The materials properties of the resonator
  - c_{66}, e_R, ε_R, ρ_R (no loss contributions),
  - η_R, ϵ_R, σ_R (loss contributions).

Resonators without sensor films are used to determine the properties of the piezoelectric materials. A layer sequence *electrode | piezoelectric material | electrode* according to Eq. 2.34 reflects this situation. Consequently, the film properties mentioned above correspond to that of the electrodes.

The determination of the materials properties is performed by fitting the actual model $Z(f_i)$ to the experimentally determined resonance spectra $Z_E(f_i)$ using the Levenberg-Marquardt algorithm [73]. Thereby, the sum of the squared differences of data and fit function

$$\chi^2 = \sum_i \left[\left(\frac{R_E(f_i) - R(f_i)}{|Z(f_i)|} \right)^2 + \left(\frac{X_E(f_i) - X(f_i)}{|Z(f_i)|} \right)^2 \right] \tag{4.1}$$

is minimized. The index i represents the number of data points within one resonance spectra. Homogeneous weighing is achieved by the impedance modulus as given in Eq. 4.1. The application of the Levenberg-Marquardt algorithm requires the mathematical derivations of the fitting function for its parameters. These equations are neither instructive nor short and, therefore, not given here.

4.1.2 Likely Errors of the Best-fit Parameters

The fit is realized using the Levenberg-Marquardt method [73]. As for every fit method, it has to be assumed that the model is a likely match to the data. Small values of χ^2 confirm the applicability of the model and the maximum likelihood of the parameters is achieved. For further confidence, the error estimates of the parameters have to be regarded. The occurrence of large errors despite of small χ^2 indicates, for example, potential correlations of the parameters.

Least-square fitting is a maximum likelihood estimation for the parameters provided that

- The measurement error is independently random and distributed as a Gaussian distribution and
- The standard derivations are the same for all measurement points [73].

Under such favorable circumstances the error estimates for the parameters can be extracted from the fit algorithm. The diagonal elements of the covariance matrix used to solve the normal equations of the least-square problem are the squared uncertainties of the fitted parameters [73]. They are extracted, converted into a confidence interval of 95 % and indicated by the error bars in the plots for c_{66}, e_R and η_R.

However, the errors of real data are hardly Gaussian distributed. Further, the measurements are also affected by systematic errors which are not considered here. Consequently, the error estimates do not cover the total error. Despite of this restrictions, the values are presented to give at least a hint to the confidence of the parameters.

4.1.3 Free Parameters of the Physical Model

It is obvious that the number of free parameters for the fit procedure must be much smaller than the total number of parameters, i.e. 16 for the one-dimensional model. Reasonable fits can be, in general, expected if the number of free parameters does not exceed three or four. This section identifies the parameters which have to be varied.

The geometrical area of the electrodes is known from the size of the shadow masks used to produce them and converted into the effective resonator area A_E according to Appendix B. This value is always kept constant. The approximate thickness of the resonator d_R is determined by a micrometer gauge.

Most relevant properties of the electrodes are their thickness d_F and density ρ_F. Accurate values of the thickness are determined using a surface profiler. The density of the platinum electrodes is assumed to be 100 % of the theoretical density. The method to deposit them, i.e. the Pulsed Laser Deposition (PLD), leads to compact films. Further, the stiffness of the 200 nm thick electrodes is set to the room temperature value of platinum $c_F = 4.8 \times 10^{10}$ Nm^{-2} [74] since its impact on the resonance behavior is negligible. Unrealistic values below about 10^7 Nm^{-2} which correspond to rubbery materials would shift the resonance frequency, only. Further, for the conditions chosen here, the viscosity of the electrodes η_F does not impact the resonance behavior at all and is, therefore, set to zero. A parameter study confirmed the fact even for extremely large viscosities. The statement corresponds to the small value of the relative derivation $\eta_F/f\ \partial f/\partial \eta_F$ which is below 10^{-6} according to Figs. 3.5 and 3.7. In summary, d_F, ρ_F and c_F are always kept constant at the values given in Appendix A. Further, η_F is set to zero since very soft materials like polymers would impact the behavior, only.

The data evaluation applied here potentially delivers unreliable absolute values due to experimental problems resulting from the stray capacitance C_L of the high-temperature sample holder. Since the arrangement of wires

and contacts is not completely fixed, C_L might be altered after calibration of the network analyzer or during sample change. As a consequence, the calibration does not compensate necessarily C_L. Inaccurate numbers of C_L would cause e.g. false dielectric constants. Further, mechanical tools do not allow a sufficiently accurate determination of the thickness of the resonator d_R which leads to wrong values for the mechanical stiffness c_{66}.

To overcome these problems, room temperature values for c_{66}, e_R, ρ_R and ε_R from the literature [40, 48, 74–76] are taken and kept constant in the room temperature fits. The numerical values used here are tabulated in Appendix A. In case of langasite, the approach is justified by independent measurements using the pulse-echo method. Thereby, the agreement of key properties of the actual material with literature data is confirmed [77]. The data of $GaPO_4$ are taken from the crystal's manufacturer.

Based on these data, an initial fit step using room temperature resonance spectra is performed. Beside the resonator thickness d_R and the stray capacitance C_L, the effective resonator area A_R and the viscosity of the resonator η_R are varied to achieve optimum fit quality. The imaginary part of the piezoelectric constant ϵ_R must be set to zero. Otherwise, the errors of the fit parameters become extremely large while the fit quality does not improve. The facts indicate that ϵ_R is either independent nor required. Further, the lead resistance R_L can be set to zero. Obviously, the calibration of the network analyzer compensates the resistance of the sample holder.

For all other temperatures, the numbers found at room temperature for C_L, A_R and ϵ_R are kept fixed. There is obviously no need to modify them. The thickness d_R and the density ρ_R are set according to their temperature dependence given in Appendix A. Further, the bulk conductivity σ_R cannot be treated as a fit parameter. As already mentioned in Section 2.3 (page 30) high resistances occurring below about 700°C in case of langasite resonators lead to undefined fit results. Consequently, independent impedance measurements at relatively low frequencies have to be performed. The dielectric constant extracted simultaneously from these measurements shows a relatively large uncertainty and can be used as initial value for the fit procedure, only. Finally, c_{66}, e_R, η_R and ε_R are varied.

4.1.4 Free Parameters of the Equivalent Circuit

The extended BvD EC includes the motional parameters R_M, C_M and L_M as well as the static parameters R_S and C_S. As for the one-dimensional physical model, high bulk resistances prevent the determination of R_S, i.e. impedance measurements are also required for this approach. The remaining parameters of the EC have to be varied in the actual fit procedure.

The conversion of the EC parameters into the physical properties requires the knowledge of the resonator dimensions and of the stray capacitance. Here, an approach comparable to that for the one-dimensional physical model is

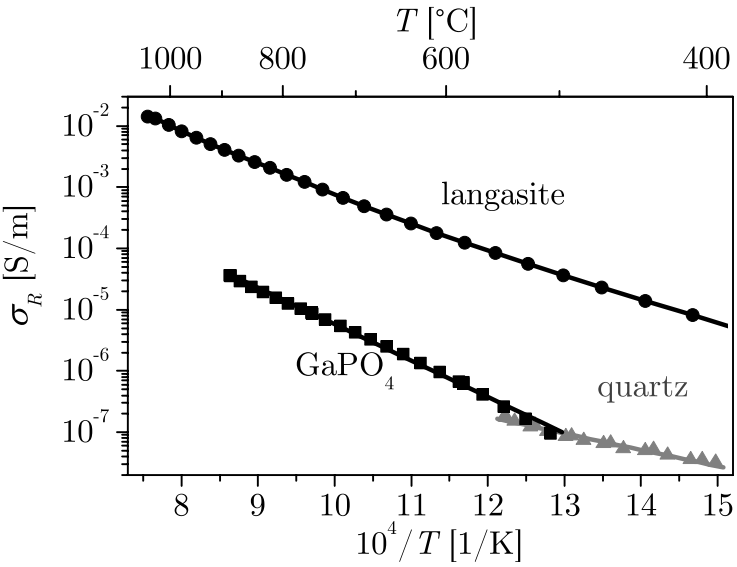

Figure 4.1: Arrhenius plot of the conductivity of langasite, gallium phosphate and quartz.

chosen. The actual calculation is done using Eqs. 2.57–2.59 and 2.61–2.63 for the low- and high-temperature approximation, respectively. Since the approach ignores the electrodes, the resonator thickness is expected to be slightly off.

4.2 Results

4.2.1 Conductivity and Dielectric Constant

Initially, the bulk conductivity of the resonator materials has to be determined. Therefore, impedance measurements in the frequency range from 10 mHz to 1 MHz are performed. The low frequency intercept of the $R_S C_S$-semicircle in the complex impedance plane represents the resistance of the parallel arrangement and is converted in the bulk conductivity σ_R. Further, the dielectric constant ε_R is extracted from the data. Experimental details and insights in the microscopic mechanisms are given in Chapter 7.

Fig. 4.1 shows the temperature dependence of σ_R. Most remarkably, the conductivity of langasite is more than two orders of magnitude higher than that of $GaPO_4$ and quartz. Therefore, the impact of the conductivity on the resonance spectra is expected to play a pronounced role in case of langasite resonators.

The temperature dependence of dielectric constants of the resonator materials is given in Fig. 4.2. Thereby, the solid symbols represent typical values

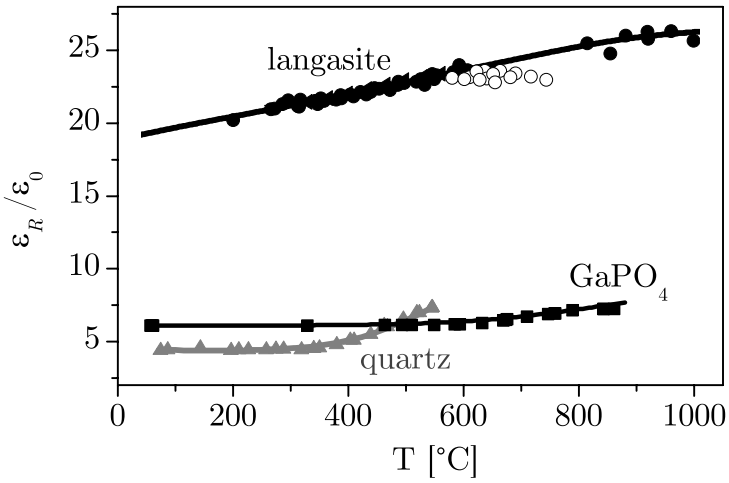

Figure 4.2: Temperature dependent dielectric constant of langasite, gallium phosphate and quartz.

which does not change as function of time. Those samples are expected to be either in a metastable state or already equilibrated. These situations correspond to relatively low and high temperatures, respectively. At intermediate temperatures, equilibration cannot be achieved within reasonable periods of time. The open symbols represent this situation where the result is time dependent. Since the conductivity is obviously less affected by time-dependent changes, other effects like the presence of hydrogenous species contributes potentially to the time-dependence of the dielectric constant. Details about the kinetics of the equilibration are given in Section 7.1.

For langasite, the temperature dependence of ε_R is in accordance with literature data measured up to about 350°C [26]. This comparison cannot be done for $GaPO_4$ since high-temperature data are obviously not published.

In order to obtain fit results using the one-dimensional physical model as done in the next section, the bulk conductivity derived here is taken and fixed for a given temperature. Due to its uncertainty the dielectric constant is used as initial parameter for the fit procedure, only.

4.2.2 One-dimensional Physical Model

First, the one-dimensional physical model is used to determine the properties c_{66}, e_R, η_R and ϵ_R by fitting it to the resonance spectra. Most important, very good agreement between data and model could be achieved in the entire temperature range. The fact is illustrated in Fig. 4.3 for langasite up to 1000°C. The symbols represent the measurements whereas the lines result from the model. The agreement justifies the applicability of the model even at very high temperatures.

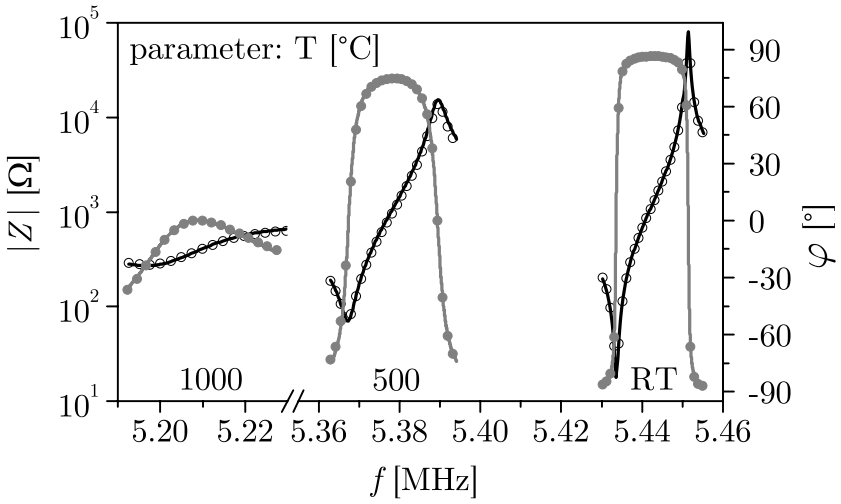

Figure 4.3: Measured resonance spectra of langasite (open symbols: $|Z|$, solid symbols: φ) and fit of the one-dimensional model (lines) at different temperatures.

Effective Resonator Area

The effective resonator area A_R is determined using resonance spectra acquired at room temperature and the literature data for c_{66}, e_R, ρ_R and ε_R. The solid symbols in Fig. 4.4 show the results for langasite (L), $GaPO_4$ (G) and quartz (Q). Remarkably, the ratio A_R/A_E is significantly smaller than unity. The fact justifies the introduction of different effective areas for the electrode and the oscillating resonator material. Further, there is no indication to changes of the ratio A_R/A_E with increasing temperature.

Fig. 4.4 shows the ratio of the resonator thickness d_R and effective electrode radius r_E which meets the empirical relation

$$\frac{A_R}{A_E} \approx 4.93 \frac{d_R}{r_E}. \tag{4.2}$$

Consequently, the effective resonator area A_R can be estimated based on the dimensions of the resonators. The fact is important since it by-passes the application of the quite complex one-dimensional physical model and must be seen with respect to the necessity to know A_R in order to

- Calculate the mass sensitivity and
- Convert the parameters of the equivalent circuit into the physical properties of the resonator materials.

Other relations such as $A_R/A_E \sim d_R$ or $A_R/A_E \sim 1/r_E$ do not describe the behavior determined experimentally.

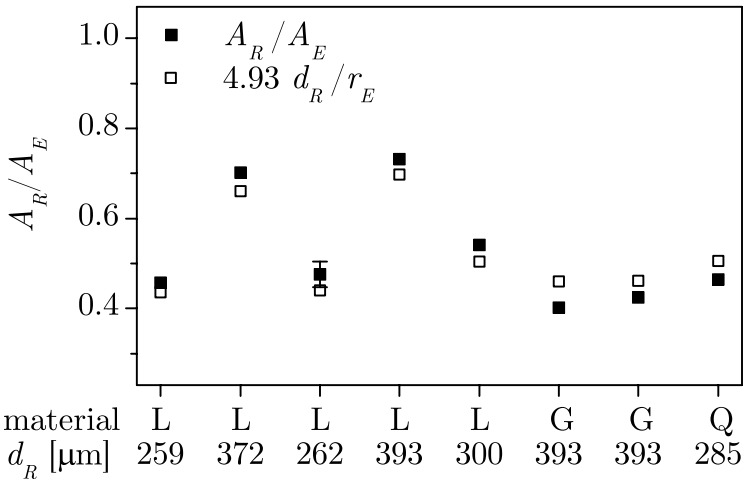

Figure 4.4: Ratio of the effective resonator area A_R to the effective electrode area A_E and their empirical description (see text) for langasite (L), gallium phosphate (G) and quartz (Q) resonators.

Elastic Properties

The shear modulus of the materials of interest is given in Fig. 4.5. Its temperature dependence determines predominantly the course of the resonance frequency as is becomes obvious by comparing Figs. 1.2 and 4.5. A modified presentation of the shear modulus according to $(c_{66} - c_{RT})/c_{RT}$ matches the pattern of $(f - f_{RT})/f_{RT}$ in Fig. 1.2. The relative change in the respective entire temperature range are the smallest for $GaPO_4$ (5 %). Stronger changes are found for langasite and quartz (9 and 17 %, respectively). The values presented here are in reasonable agreement with literature data determined e.g. by resonant ultrasound spectroscopy up to 450°C [78, 79].

Piezoelectric Coefficients

Fig. 4.6 shows the temperature dependent piezoelectric coefficient e_R for langasite, $GaPO_4$ and quartz. Since its sign does not impact the dynamic behavior of TSM resonators, its modulus is of interest for the further discussion.

Remarkably, the piezoelectric coefficient of langasite is about three times as large as that of quartz. Further, the property is expected to decrease with increasing temperature as observed for $GaPO_4$ and quartz. In contrast, langasite shows a reverse temperature dependence which might be an intrinsic piezoelectric property. In any case, the large value and its increase with increasing temperature are advantageous features of langasite for high-temperature applications. Another important issue is the very little temperature dependence of the piezoelectric coefficient of $GaPO_4$. At 930°C,

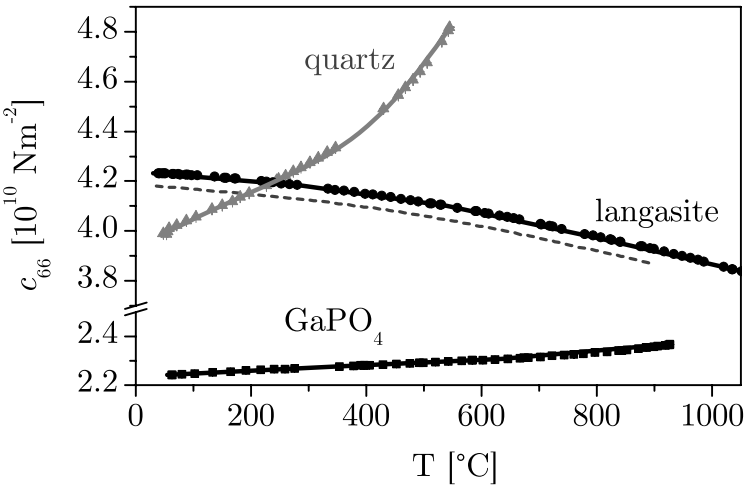

Figure 4.5: Temperature dependent shear modulus of langasite, gallium phosphate and quartz (line and symbols: physical model, dashed line: BvD EC model).

the modulus is only 5 % lower than that at room temperature. The results for $GaPO_4$ matches very well the data from the crystal's manufacturer measured at temperatures up to about 700°C by the Michelson interferometry [40, 76]. The piezoelectric coefficient of langasite correspond to data given up to 500°C in [31]. Further, independent measurements performed in our laboratory [77, 80] are in accordance with these data.

Viscosity

The viscosity of the piezoelectric materials exhibits a quite different behavior. $GaPO_4$ and quartz show an almost linear slope in the $\log(\eta_R) - T$ plot as presented in Fig. 4.7. The only exception is found in a narrow temperature range around 400°C where the resonance spectra of the quartz resonators cannot be fitted due to numerous spurious resonance modes. The loss of quartz seems to be increased around this temperature. In contrast, langasite undergoes some loss maximus as seen by the shallow peaks of the viscosity at about 250, 700 and 950°C. Remarkably, the loss tends to decrease with increasing temperature above 950°C. Further, the temperature dependence of η_R corresponds to that of the viscosity related resistance R_η presented in Fig. 3.12.

In the literature, the loss is described predominantly by the resonator quality factor Q. Therefore, a direct comparison with the viscosity cannot be done. However, loss peaks in form of Q^{-1} are reported for langasite at 260 [81] and 680°C [79] which supports the result presented here.

The loss of hydrogen swept quartz is reported in [82, 83] in the temperature range up to 450°C. Such crystals exhibit a moderate and nearly temperature independent loss up to about 400°C. Commonly, alkali impu-

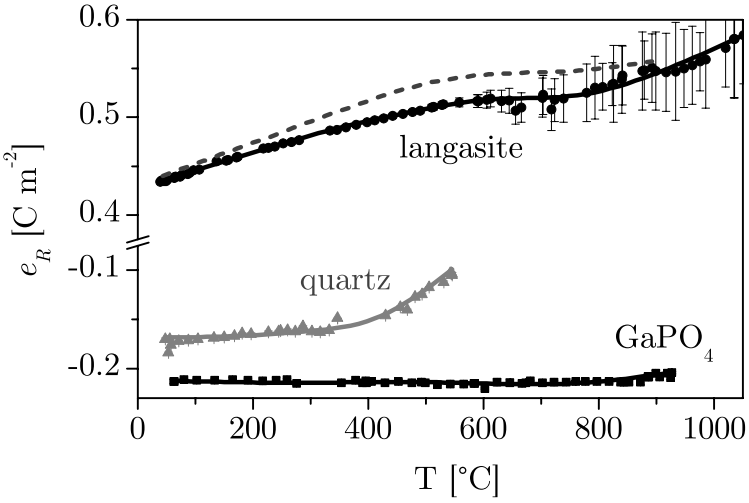

Figure 4.6: Temperature dependent piezoelectric constant of langasite, gallium phosphate and quartz (line and symbols: physical model, dashed line: BvD EC approach).

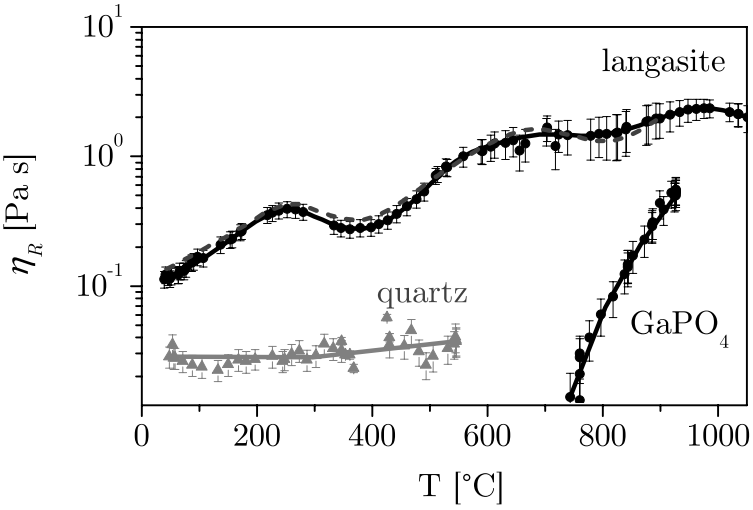

Figure 4.7: Temperature dependent viscosity of langasite, gallium phosphate and quartz (line and symbols: physical model, dashed line: BvD EC approach).

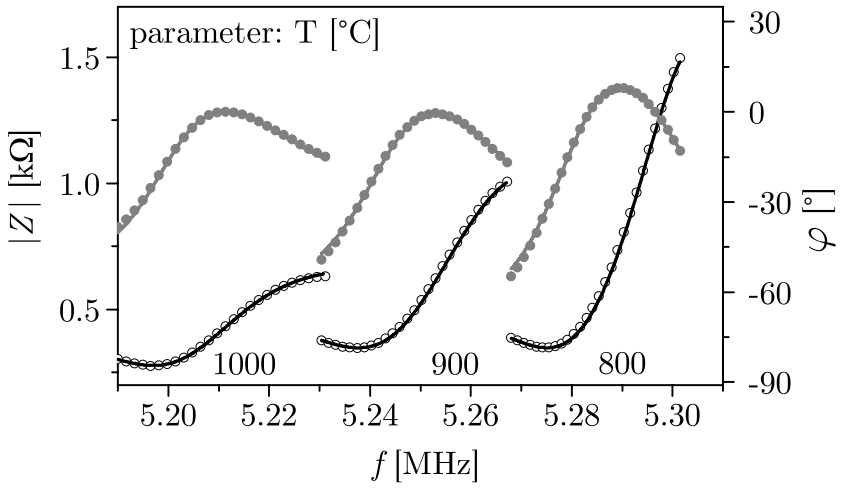

Figure 4.8: Measured resonance spectra of langasite (open symbols: $|Z|$, solid symbols: φ) and fit of the extended Butterworth-van Dyke equivalent circuit (lines) at different temperatures.

rity ions are thermally activated and responsible for the acoustic loss. If they are replaced by hydrogen, the loss is largely suppressed. Above about 400°C an increase of the loss is observed which goes along with the data presented here. The behavior of quartz is, however, not investigated in detail since its materials properties are introduced for comparison, only.

Independent reference data for $GaPO_4$ at high temperatures are obviously not published. Details about the loss in langasite are discussed in Section 5.4.

4.2.3 Extended Butterworth-van Dyke Circuit

Secondly, the extended BvD equivalent circuit model is used to determine the properties c_{66}, e_R, η_R and ϵ_R by fitting it to the resonance spectra. Thereby, two steps, i.e.

- The determination of the parameters of the equivalent circuit and
- Their conversion into the physical properties of the resonator materials

is performed. As an example langasite is chosen.

Good agreement between experiment and model could be achieved by the low temperature approximation of the extended BvD EC up to 1000°C as seen in Fig. 4.8. However, above about 900°C, the fit quality is achieved at the expense of modified values for C_M, only. The parameter starts to differ from that calculated by the one-dimensional physical model. Therefore, the model no longer suited to extract the materials properties. The temperature limit matches the condition for the inapplicability of the extended BvD EC accord-

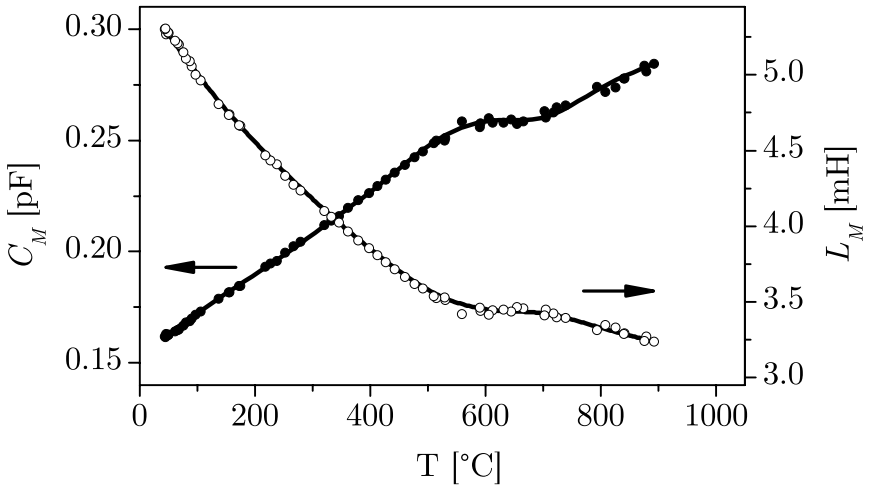

Figure 4.9: Temperature dependence of the motional parameters C_M and L_M of the extended Butterworth-van Dyke equivalent circuit for langasite.

ing to Eq. 2.56. For the actual resonator applies $\varepsilon_R\omega = \sigma_R = 7.6\ 10^{-3}$ S/m which corresponds to 970°C. Consequently, up to some temperature below that limit, i.e. in the specific case up to about 900°C, the parameters of the extended BvD EC can be determined accurately. Above the limit of 970°C, the structure of extended BvD EC becomes correct again. Consequently, the fit quality should improve with increasing temperature while applying the high-temperature approximation for the BvD EC. The expectation could, however, not be proven experimentally since the stability of the electrodes limits the investigations to 1050°C.

Figs. 4.9 and 4.10 present the temperature dependence of the motional parameters C_M, L_M and R_M of the extended BvD EC up to 900°C. It should be noted that the product $C_M L_M$ is determined by the resonance frequency. Therefore, it can be extracted very precisely from the data. In contrast, the fit procedure does not deliver accurate values for the ratio of C_M and L_M since the χ^2 function shows little changes if that ratio is varied. The fact might explain the slope of C_M and L_M around 600°C.

The parameters of the extended BvD EC are known for $\sigma_R < \varepsilon_R\omega$, only. Therefore, they are converted into the materials parameters c_{66}, e_R and η_R using the low temperature approximation according to Eqs. 2.57–2.59. The thickness of the resonators is taken from the data of the one-dimensional physical model. Further, Eq. 4.2 is used to calculate A_R from A_E. The results of the conversion are shown as dashed lines in Figs. 4.5–4.7.

So far, the contribution of the electrodes to the resonance behavior is neglected. Since the electrodes act as an additional mass shifting the resonance spectra to lower frequencies, a c_{66} different from the one-dimensional physi-

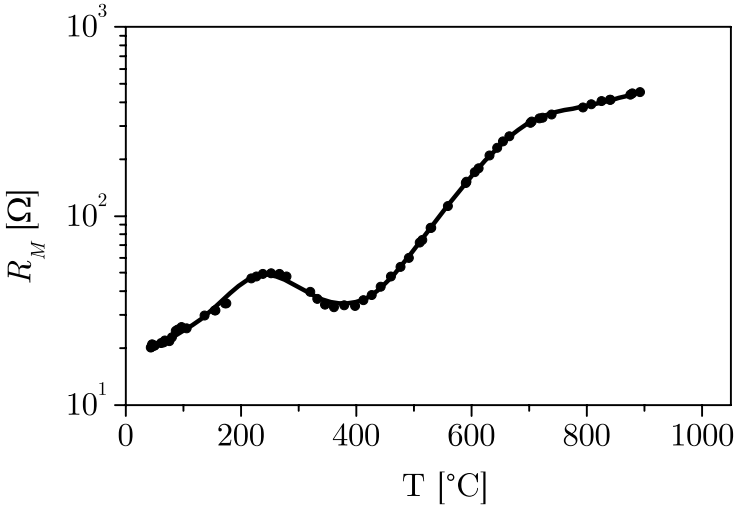

Figure 4.10: Temperature dependence of the motional parameter R_M of the extended Butterworth-van Dyke equivalent circuit for langasite.

cal model is expected. The dashed line in Fig. 4.5 confirms this fact. Using Sauerbrey's approach to express a mass uptake by the electrodes as change of the resonator thickness, the difference can be corrected. An increase of the resonator thickness d_R by $\Delta d_R = d_F \rho_F / \rho_R$ corrects the difference in c_{66}. If required, the determination of d_R can be done independently of the one-dimensional physical model. The property has to be adjusted using room temperature data for c_{66} from the literature.

The piezoelectric constant derived from the extended BvD EC and the one-dimensional physical model differs slightly as seen in Fig. 4.6. The fact might be caused by the uncertainty in determining L_M. The viscosity resulting from both approaches matches very well. The fact becomes obvious by the dashed line in Fig. 4.7 which is almost covered by the data from the one-dimensional physical model.

Provided that the limit $\sigma_R < \varepsilon_R \omega$ is regarded, the extended BvD EC describes the resonance behavior satisfactorily. The approach is suited for time-inexpensive data modeling. Minor differences occur if the EC parameters are converted into the physical properties of the resonator materials. Therefore, the application of the one-dimensional physical model is recommended for precise determination of the materials properties.

Chapter 5

Resonance Properties

One key property of langasite, $GaPO_4$ and quartz resonators, namely their temperature dependent resonance frequency is already presented in Fig. 1.2. Further issues such as the mass sensitivity and the mass resolution have to be considered to evaluate the resonators comprehensively. Except for the resonator geometry, the mass sensitivity is predominantly determined by the shear modulus c_{66} and the resonator density ρ_R whereas the mass resolution is governed by the resonator quality factor Q. The latter depends on η_R and σ_R. Beyond that, the stable operation of the resonators at elevated temperatures requires the knowledge of the impact of the remaining materials properties.

In contrast to the parameter study in Section 3.1.2

- Measured data and
- Analytical derivatives of the series resonance frequency for the materials properties

are used here. If not stated otherwise the series resonance frequency f_S is denoted by f from now on.

The measurements presented so far are performed in air. Extreme conditions may alter the properties of the resonator materials and affect, thereby, the resonance behavior. However, in Chapter 8 is shown that the operation in air impacts the materials properties of the resonators in the most modest extend. Consequently, the following sections deliver resonance characteristics least affected by the environmental conditions.

After discussing the temperature dependence of the resonance frequency, its temperature compensation is introduced since the evaluation of other properties is preferably done based on that frequency.

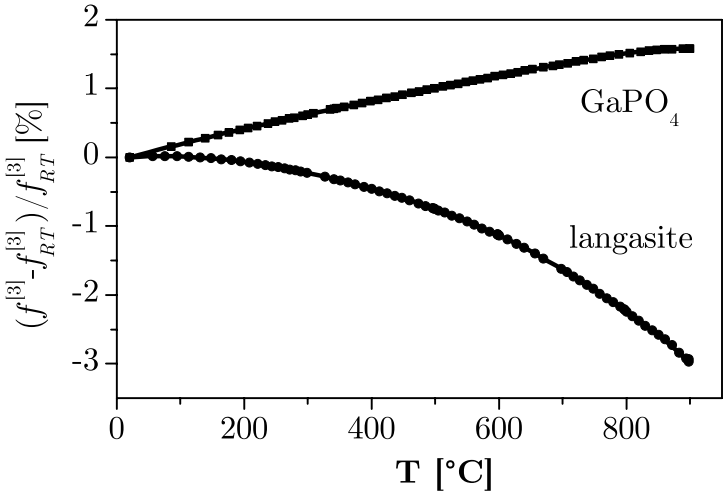

Figure 5.1: Temperature dependent resonance frequency of the 1^{st} overtone of langasite and gallium phosphate resonators.

5.1 Resonance Frequency

The temperature dependent resonance frequency of the fundamental mode ($N = 1$) is already presented in Fig. 1.2. For completeness, this property is given for the 1^{st} overtone ($N = 3$) in Fig. 5.1. In case of langasite and $GaPO_4$ the relative frequency shift can be approximated satisfactorily by a parabolic function

$$\frac{f^{[N]} - f^{[N]}_{RT}}{f^{[N]}_{RT}} = c^{[N]}_0 + c^{[N]}_1 T + c^{[N]}_2 T^2. \tag{5.1}$$

The temperature ranges, the constants $c^{[N]}_0$, $c^{[N]}_1$ and $c^{[N]}_2$ as well as the turnover temperature T_{TC} ($\partial f/\partial T|_{T_{TC}} = 0$) are given in Tab. 5.1. The determined temperature dependence of langasite is in general accordance with the results for BAW resonators in the temperature range from 5 to 125°C [84] and for SAW devices at temperatures of up to about 1000°C [33]. It should be noted that the 1^{st} overtone temperature dependence of $GaPO_4$ is vanishing at about 900°C.

The derivatives of the resonance frequency for the temperature, i.e. the temperature coefficients $c = \partial f/\partial T$, are shown in Fig. 5.2. It becomes obvious that the absolute values for quartz are significantly higher of than those for langasite and $GaPO_4$. Nevertheless, the latter materials exhibit temperature coefficients of several hundred Hz/K at elevated temperatures.

Table 5.1: Temperature related parameters of the resonance frequency according to Eq. 5.1 and turnover temperatures.

	N	range [°C]	$c_0^{[N]}$ [10^{-3} °C]	$c_1^{[N]}$ [10^{-5}]	$c_2^{[N]}$ [10^{-8} °C^{-1}]	T_{TC} [°C]
langasite	1	20 ... 800	-0.74	0.14	-4.82	(15.1)
	3	20 ... 700	0.28	0.22	-3.58	31.2
$GaPO_4$	1	20 ... 600	1.34	1.34	1.41	–
	3	20 ... 800	-0.58	0.25	-0.69	–

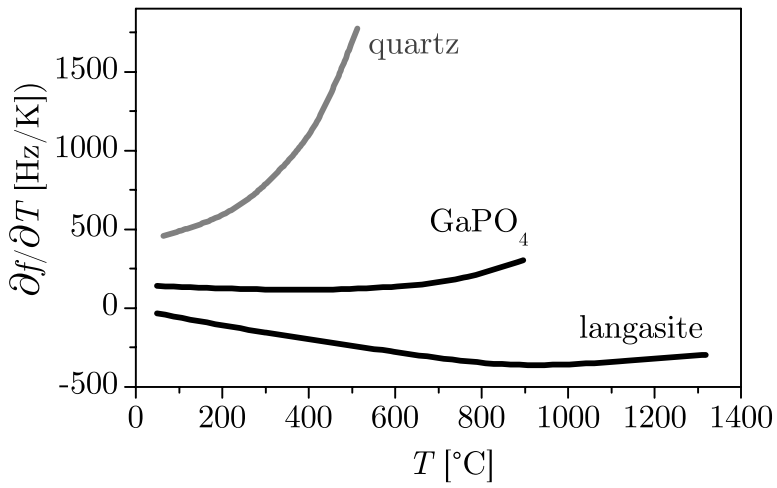

Figure 5.2: Temperature coefficients of the series resonance frequency of 5 MHz langasite, gallium phosphate and quartz resonators.

5.2 Temperature Compensation

The large temperature coefficients must be seen in the context of mass load dependent frequency shift of resonators expected to be in the order of tens of Hz. Given the temperature coefficient of the 5 MHz standard langasite resonator of about 280 Hz/K at 600°C, temperature fluctuations of only 0.01 K overwhelm the signal of interest. Consequently, temperature effects have to be excluded or drastically minimized. The reduction to practice includes two different approaches, namely

1. The application of temperature-compensated crystal cuts and
2. Compensation methods.

The first approach limits the operation temperature to a narrow range. However, if such conditions apply, the approach is highly attractive for commercial applications. The resonance frequency can be obtained with minimum effort. In order to determine temperature-compensated crystal orientations, a full set of materials parameters as presented in [77, 80] is required.

The second approach opens up a wide operation temperature range for a given device and is, therefore, suited for e.g. laboratory conditions. First and most simply, an external temperature probe can be used to calculate the temperature-compensated frequency f_{EP} (EP = external probe) according to

$$f_{EP} = f - c^{[1]}\left(T - T_0\right) \tag{5.2}$$

with $c^{[1]}$, T and T_0 as temperature coefficient, measured and nominal operation temperature, respectively. According to the example given above, temperature measurements more accurate than 0.01 K are required. Therefore, difficulties come up with external temperature probes even if they are installed in very close proximity to the piezoelectric devices. In case of gas sensors, reactions catalyzed by e.g. platinum electrodes or by sensor films may cause local temperature differences. Further, temporary temperature fluctuations may obviously arise upon temperature changes due to differences in heat capacity of temperature probe and piezoelectric device.

An improved compensation approach uses the fundamental mode and the 1^{st} overtone resonance frequency of the actual resonator itself to exclude temperature effects, and does not require accurate external temperature measurements. Therefore, the previously described problems do not apply. The temperature dependence of the fundamental mode ($N = 1$) and of the 1^{st} overtone ($N = 3$) can be expressed as linear functions in the vicinity of T_0 according to

$$f^{[N]}\left(T, m, ..\right) = f_0^{[N]}\left(m, ..\right) + c^{[N]}\left(T - T_0\right). \tag{5.3}$$

The frequencies $f^{[N]}$ are regarded as function of temperature T, mass load m and other undesignated parameters. The resonance frequencies at T_0 are

denoted by $f_0^{[N]}$ with

$$f_0^{[N]}(m,..) = f^{[N]}(T_0, m, ..). \tag{5.4}$$

From Eq(s). 5.3, the temperature difference $T - T_0$ can be eliminated which results in a temperature independent frequency f_{IC} (IC = internal compensation) according to

$$f_{IC}(m,..) = f_0^{[1]}(m,..) - \frac{c^{[1]}}{c^{[3]}} f_0^{[3]}(m,..) = f^{[1]}(T,m,..) - \frac{c^{[1]}}{c^{[3]}} f^{[3]}(T,m,..). \tag{5.5}$$

If the expectations $3f^{[1]} \approx f^{[3]}$ and $3c^{[1]} \approx c^{[3]}$ hold true, the values for f_{IC} would be fairly small. However, the temperature dependencies do not correspond entirely to this expectation which lead to finite values of f_{IC}. The fact becomes obvious by the temperature dependence of $f^{[1]}$ and $f^{[3]}$ presented in Fig. 3.16[1] and the values for $3c^{[1]}/c^{[3]}$ given in Tab. 5.2. In the literature, different temperature dependencies of the overtones are reported in the temperature range from 5 to 125°C in [84, 85] which supports these findings. A theoretical approach describes the crystal orientation dependent resonance behavior of quartz resonators [86]. It is concluded that the nodal planes of the anharmonics of each harmonic family are oriented differently. Since langasite belongs to the same crystal class as quartz the conclusion can be applied here. Differently oriented vibration planes of the harmonic families and the orientation dependent materials constants would be one possible explanation for the differences in temperature behavior. Another explanation could be the overtone dependent extent of energy trapping.

The temperature compensation schemes can only be applied on the condition that the temperature coefficients are known and independent from the environmental parameter of interest. The gas atmosphere composition is taken as an example and investigated in the vicinity of 600°C using a platinum contacted langasite resonator with $f^{[1]} \approx 2.1$ MHz. The temperature coefficients result from setting the atmosphere alternately to O_2, Ar and 6 % H_2/Ar and subsequent variation of the temperature from 590 to 610°C. Fitting of a linear function to $f^{[N]}(T)$ yields $c^{[N]}$. As shown in Tab. 5.2, the temperature coefficients are oxygen partial pressure independent within its error range. Consequently, the temperature compensation schemes can be applied for the environmental conditions described above. It should be noted that langasite resonators coated with e.g. $TiO_{2-\delta}$ sensor films also show oxygen partial pressure independent temperature coefficients and can be subjected to the temperature compensation.

[1]It must be underlined that $f^{[N]}$ in Fig. 3.16 is calculated based on the temperature dependence of σ_R and η_R, only. The consideration of the temperature dependence of all parameters would potentially result in even higher differences between $3f^{[1]}(T)$ and $f^{[3]}(T)$.

Table 5.2: Temperature coefficients of the series resonance frequency of a 2.1 MHz langasite resonator operated in different atmospheres at 600°C.

atmosphere	$c^{[1]}$ [Hz/K]	$c^{[3]}$ [Hz/K]	$3c^{[1]}/c^{[3]}$
O2	-125.4	-279.1	1.35
Ar	-127.0	-282.5	1.35
6% H_2/Ar	-126.9	-280.2	1.36
average	-126.4	-280.6	1.35

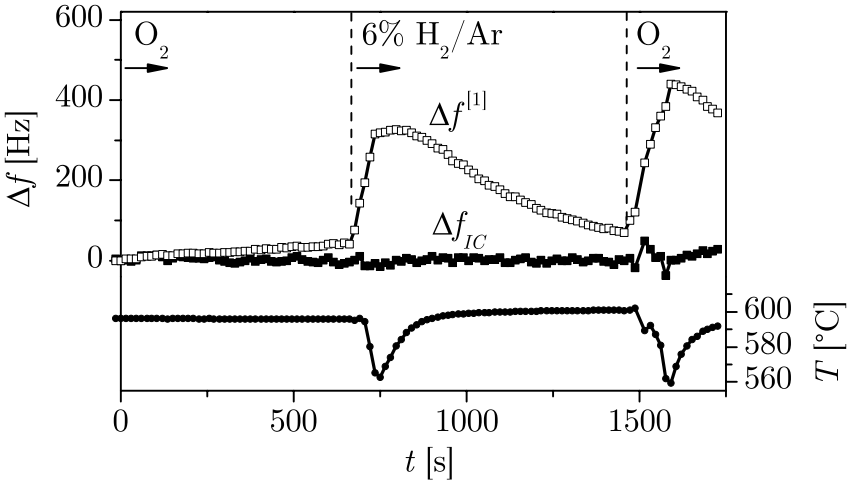

Figure 5.3: Significant frequency fluctuations $\Delta f^{[1]}$ and vanishing frequency shift Δf_{IC} of an uncoated langasite resonator during switching the atmosphere from oxygen to 6 % H_2/Ar and reverse.

The internal temperature compensation is proven by exposure of the platinum contacted resonator to gas exchanges from pure oxygen to 6 % H_2/Ar and reverse at nominally 600°C. The lower part of Fig. 5.3 shows the corresponding temperature fluctuations of about 40 K as determined by an external temperature probe. Consequently, the raw data $f^{[N]}$ varies by several hundreds of Hz in an undefined manner as visualized by $\Delta f^{[1]}$ in the upper part of Fig. 5.3. Any intensional response in the expected order of tens of Hz becomes disguised. In contrast, the temperature-compensated frequency f_{IC} does not show significant deviations upon gas exchange. Temperature effects are minimized successfully. The few peaks of about 20 Hz can be explained by the fact that $f^{[1]}$ and $f^{[3]}$ are not determined at the same time. A shift of about 5 s between the measurements results in a temperature difference which distorts the compensation. The disturbance is observable for fast temperature fluctuations, i.e. during gas exchange, only.

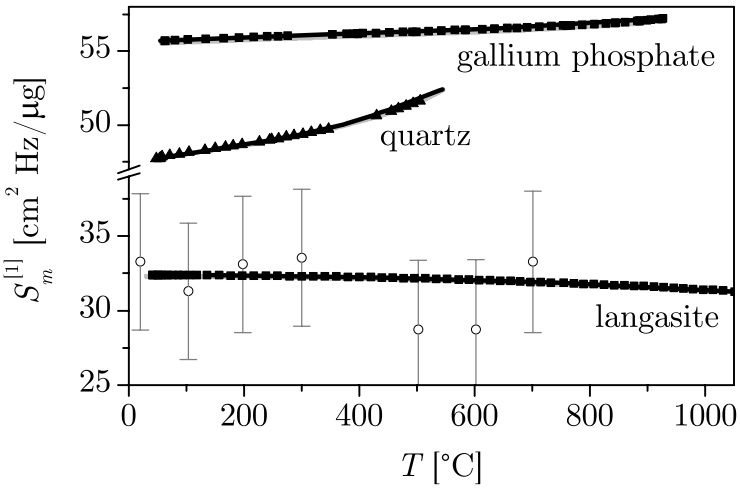

Figure 5.4: Mass sensitivity of 5 MHz y-cut langasite, gallium phosphate and quartz resonators as function of temperature.

The external temperature compensation requires highly precise temperature data which can be provided by averaging over a prolonged period of time, only. For the experimental conditions chosen here, the latter is fulfilled very rarely. Consequently, the internal compensation is the preferred approach and applied unless specified otherwise.

5.3 Mass Sensitivity

The impact of the resonator thickness d_R on the series resonance frequency $f(d_R(m_R))$ is determined and converted into a mass sensitivity $S_m^{[1]}$ according to

$$S_m^{[1]} = -A_R \frac{\partial f^{[1]}}{\partial m_R} = -A_R \frac{\partial f^{[1]}}{\partial d_R} \frac{\partial d_R}{\partial m_R} \tag{5.6}$$

with $\partial d_R/\partial m_R = 1/(A_R \rho_R)$. Thereby, the analytical derivative of Eq. 2.47 for d_R and the materials parameters presented in Chapter 4 are used. The result corresponds to the Sauerbrey equation in the sense that the mass uptake m is expressed as a change of the resonator mass m_R. The black curves in Fig. 5.4 are the result for quartz, $GaPO_4$ and langasite resonators showing a resonance frequency of 5 MHz at room temperature. Fig. 5.4 also contains grey curves for each material resulting from simplified calculations of the mass sensitivity for small acoustic loads without consideration of the finite resonator conductivity [87]

$$S_m^{[N]} = \frac{2N f^{[1]2}}{\sqrt{\rho_R c_{66}}} = \frac{N}{2{d_R}^2} \sqrt{\frac{c_{66}}{{\rho_R}^3}}. \tag{5.7}$$

Table 5.3: Mass sensitivity of 5 MHz y-cut langasite, gallium phosphate and quartz resonators. The value for an AT-cut quartz resonator is given in parenthesis.

T [°C]	$S_m^{[1]}$ [cm^2 Hz/μg]		
	langasite	$GaPO_4$	quartz
20	32.4	55.7	47.7 (56.5)
600	32.1	56.5	–
800	31.8	56.8	–
1000	31.4	–	–

These curves are almost covered by the black curves which indicates the applicability of the simplified approach to calculate the mass sensitivity. Numerical values for the mass sensitivity are given in Tab. 5.3.

Complementary, the mass sensitivity is determined experimentally by changing the thickness of the platinum electrodes. Additional platinum is deposited between measuring the temperature dependence of the resonance frequency. Thereby, the change in mass Δm and frequency Δf are related to the mass sensitivity at 5 MHz using the resonance frequency f_{RT} of the actual resonator at room temperature

$$S_m^{[1]} = -A_R \frac{\Delta f^{[1]}}{\Delta m} \left(\frac{5 \text{ MHz}}{f_{RT}} \right)^2 \tag{5.8}$$

and given in Fig. 5.4 as open circles. Thereby, the resonator area is set to $A_R = 0.7\, A_E$ which is a reasonable value for the actual resonator. The large errors result from the uncertainty of the experimental approach including the measurement of the electrode thickness and temperature.

The most important result is the comparable mass sensitivity of these resonator materials. Even at elevated temperatures, the sensitivity of langasite and $GaPO_4$ is in the same order of magnitude than that of quartz at room temperature. Gallium phosphate exhibits a slightly higher sensitivity than quartz whereas langasite is slightly less sensitive. Therefore, the detection of very tiny mass changes caused by e.g. gas adsorption processes or stoichiometry changes in thin films is, in principle, feasible at elevated temperature.

The meaning of the mass sensitivity S_{IC} of the temperature compensated frequency f_{IC} remains to be discussed. Applying Eq. 5.5, S_{IC} results in

$$S_{IC} = -A_R \frac{\Delta f_{IC}}{\Delta m} = S^{[1]} - \frac{c^{[1]}}{c^{[3]}} S^{[3]} = S^{[1]} \left(1 - \frac{3c^{[1]}}{c^{[3]}} \right). \tag{5.9}$$

Taking the temperature coefficients of the 2.1 MHz langasite resonator at 600°C from Tab. 5.2, it turns out that, in this case, the temperature compensation changes the magnitude as well as the sign of the mass sensitivity,

i.e. S_{IC} = -0.35 $S^{[1]}$. This fact has, of course, to be taken into consideration while discussing mass effects.

If required, similar considerations have to be undertaken for other resonance properties such as the bandwidth at half maximum of the admittance peak which represents losses.

5.4 Resonator Quality Factor

The applicability of high-temperature resonators depends crucially on their quality factor Q. In order to relate this property directly to losses, the inverse value Q^{-1} has to be regarded. In contrast to the parameter study in Section 3.1.3, the following calculations base on the measured data.

First, the Q-factor for langasite is derived from the parameters of the extended BvD EC and from the bandwidth approach and presented in Fig. 5.5 by the open and solid symbols, respectively. Within the availability range of the EC parameters, i.e. up to 900°C both approaches match. Further, the Q-factor is calculated for $GaPO_4$ and quartz using the bandwidth approach. As already discussed in the context of the viscosity, langasite shows higher losses than $GaPO_4$ and quartz.

In order to compare the inverse Q-factor and the viscosity η_R, the latter property is added to Fig. 5.5 by dashed lines. Appropriate scaling of the left and right hand axis demonstrates their equivalence. The statement holds true for langasite up to about 550°C which is not surprising since the parameter study, and in particular Fig. 3.10, indicates a clear dominance of viscosity related losses in langasite at low temperatures. The data of $GaPO_4$ and quartz[2] are in accordance in the entire temperature range. Consequently, the loss of $GaPO_4$ and quartz is exclusively dominated by mechanical contributions even at elevated temperatures.

In contrast, langasite is influenced by conductivity related losses above 550°C. The transition temperature can be defined by the condition $Q^{-1} = 2\ Q_\eta^{-1}$ leading to about 650°C. Details are discussed in Section 8.2.

5.5 Mass Resolution

Temperature related frequency shifts can be excluded by evaluation f_{IC}. However, losses potentially limit the accuracy in frequency determination and, thereby, the applicability of resonant langasite sensors at elevated temperatures.

An increase in damping or Q^{-1} with increasing temperature and a clear correlation between Q^{-1} and the uncertainty in the peak frequency, expressed

[2]The small difference between Q^{-1} and η_R of quartz above about 450°C might be an artefact due to the scattering of the data and is, therefore, not discussed.

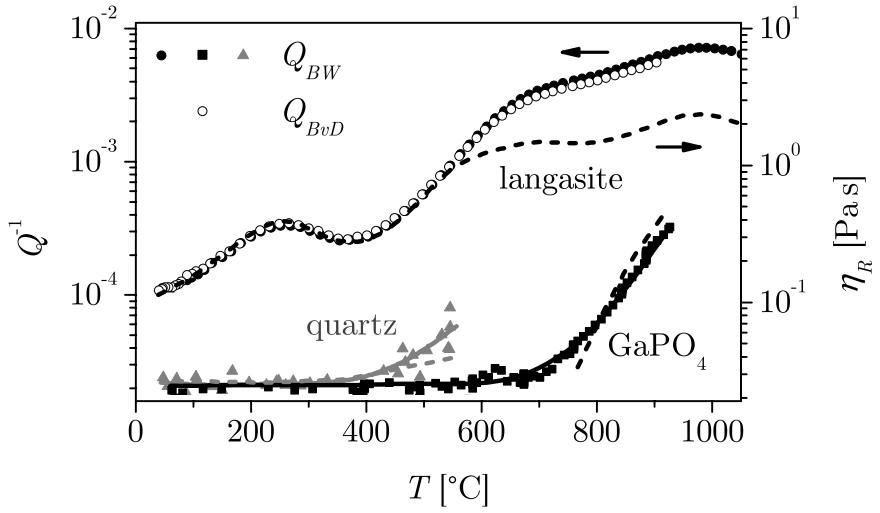

Figure 5.5: Inverse Q-factor (solid lines and symbols) and viscosity (dashed lines) as function of temperature for langasite, gallium phosphate and quartz.

as a multiple of the standard derivation σ_f, is observed. A factor of 1.96 σ_f corresponds to a probability of 95 % of finding the frequency within the values given in Fig. 5.6. The parameter $i = 5, 10, \ldots, 200$ indicates the number of points of the spectra $G(f_i)$ used for the determination of f as indicated in Fig. 5.7. Small i result in a noise of several hundred Hz which is much larger than the frequency shifts expected from e.g. microbalance applications. The situation corresponds to the frequency determination by oscillator circuits, where low Q values limit the resolution of the measurement. In contrast, high i values drastically reduce the noise.

For the given experimental conditions, a noise of $f^{[1]}_{noise} = \pm 4$ Hz at 1000°C is achieved by choosing $n = 100$. Larger numbers of data points i does not decrease $f^{[1]}_{noise}$ noticeably. A comparable value of $f_{noise,IC} = \pm 9$ Hz at 600°C is observed after temperature compensation, where the signal is composed of the fundamental mode and the 1^{st} overtone frequency.

The mass resolution

$$R^{[1]} = \left| \frac{f^{[1]}_{noise}}{S^{[1]}} \right| \tag{5.10}$$

results in 124 ng/cm^2 taking the noise $f^{[1]}_{noise} = 4$ Hz and the mass sensitivity $S^{[1]} = 32.1$ cm^2 Hz/μg of 5 MHz langasite resonators at 600°C from Fig. 5.4. If the temperature compensation is applied, the calculation yields $R_{IC} = |f_{noise,IC}/S_{IC}| = 910$ ng/cm^2.

For further discussions, frequency fluctuations of 5 MHz resonators equivalent to noise of ± 4 Hz are defined as criterion to determine the range of stable operation.

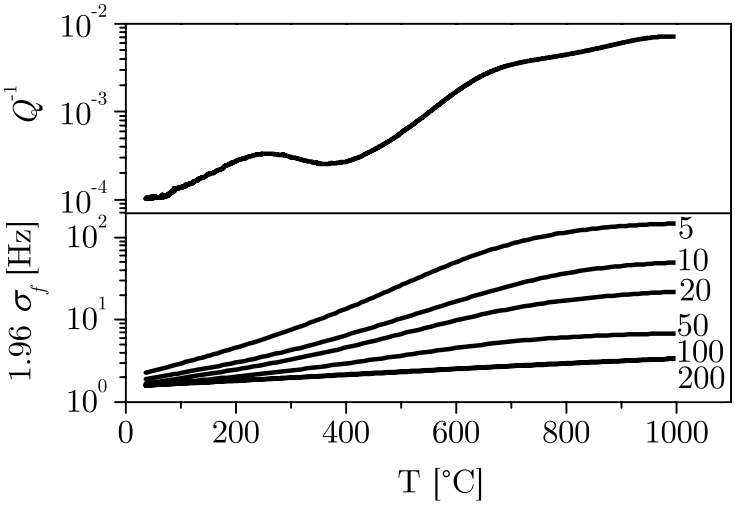

Figure 5.6: Temperature dependent inverse Q-factor and frequency noise expressed as multiple of the standard derivation. The numbers adjacent to each curve in the plot of 1.96 σ_f indicate the number of data points used to determine the peak frequency from the admittance peak.

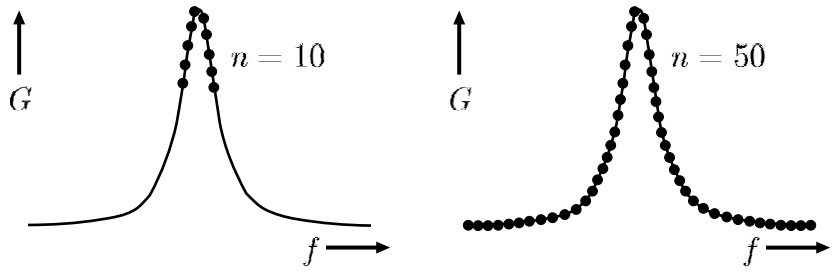

Figure 5.7: Schematic view of the distribution of data points used for the determination of the series resonance frequency $f = f(G_{max})$.

5.6 Impact of the Materials Parameters

The evaluation of the tolerable frequency fluctuations requires the knowledge of the impact of the most relevant materials properties c_{66}, ρ_R, σ_R and η_R as already identified by the parameter study in Section 3.1.2. For the calculations, a resonance frequency of $f = 5$ MHz is chosen again.

First, the relative derivative of the resonance frequency for the shear modulus $\kappa_c = c_{66}/f\, \partial f/\partial c_{66}$ is calculated. A value of approximately 0.49 applies for the three piezoelectric materials and is almost temperature independent. The relatively strong effect of c_{66} on the resonance frequency has to be compensated as already described in Section 5.2.

Further, the derivative of the series resonance frequency for the resonator density $\partial f/\partial \rho_R$ is calculated and related to the mass m_R of the actual resonator material according to $\partial \rho_R/\partial m_R = 1/(A_R d_R)$. The analytical calculation confirms the numerical result from the parameter study in Section 3.1.2. The frequency shift caused by mass changes of the resonator material Δm_R is half of that caused by an external mass uptake Δm, i.e.

$$S_\rho = -\frac{1}{d_R}\frac{\partial f}{\partial \rho_R} = \frac{1}{2}\, S_m. \tag{5.11}$$

Consequently, special attention must be drawn to environmental dependent mass changes of the resonator material. Chapter 8 covers that crucial issue for the operation of resonators as stable sensor platform.

Finally, the impact of the conductivity on the resonance frequency is calculated. Fig. 5.8 shows the temperature dependence of the relative derivative $\kappa_\sigma = \sigma_R/f_S\, \partial f_S/\partial \sigma_R$. Most remarkably, the effect of the conductivity runs though a maximum at about 930°C for langasite. This statement corresponds qualitatively to the slope of the curve for X_σ in Fig. 3.14. In contrast, Fig. 3.7 does not point to this phenomenon since the relative derivatives are calculated only for some specific temperatures, namely room temperature, 500 and 1000°C. The resonance frequency of $GaPO_4$ and quartz (gray triangles in Fig. 5.8) is virtually not affected by the conductivity.

The viscosity does not influence the series resonance frequency at all since the property is not included in Eq. 2.47.

The conclusion is that the conductivity of langasite should be minimized primarily to decrease their impact on the frequency. In addition, conductivity and viscosity related losses decrease the mass resolution. The effect can be excluded to some extend by acquisition of sufficiently large numbers of data points. Nevertheless, the loss should be as low as possible.

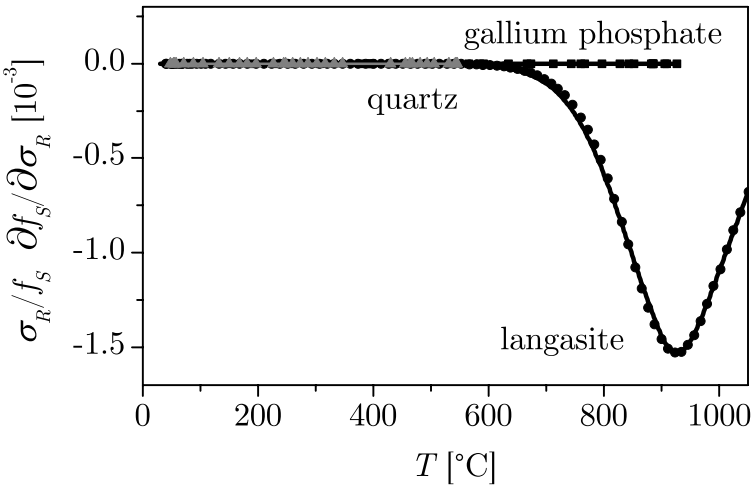

Figure 5.8: Temperature dependent relative derivative of the resonance frequency for the conductivity of langasite, gallium phosphate and quartz.

For completeness, the impact of the materials properties identified as less relevant in Section 3.1.2 is presented. The temperature dependence of the relative derivatives of f for ε_R and e_R are given in Figs. 5.9 and 5.10. These values are required to discuss the effect of hydrogen containing species on the resonance behavior in Chapter 8.

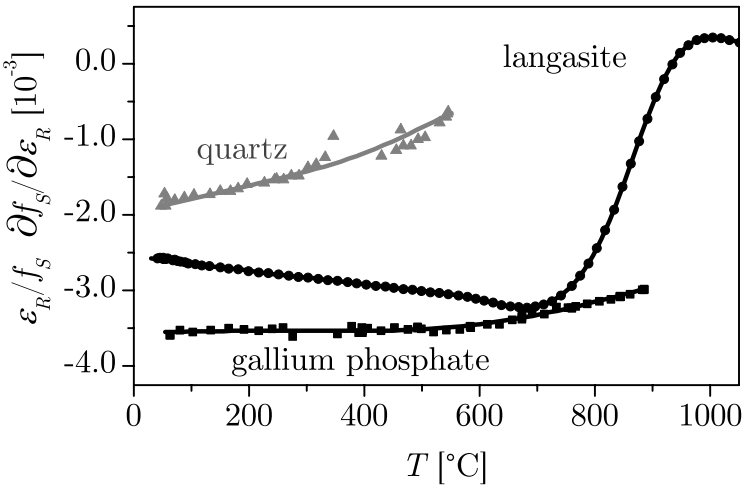

Figure 5.9: Temperature dependent relative derivative of the resonance frequency for the dielectric constant of langasite, gallium phosphate and quartz.

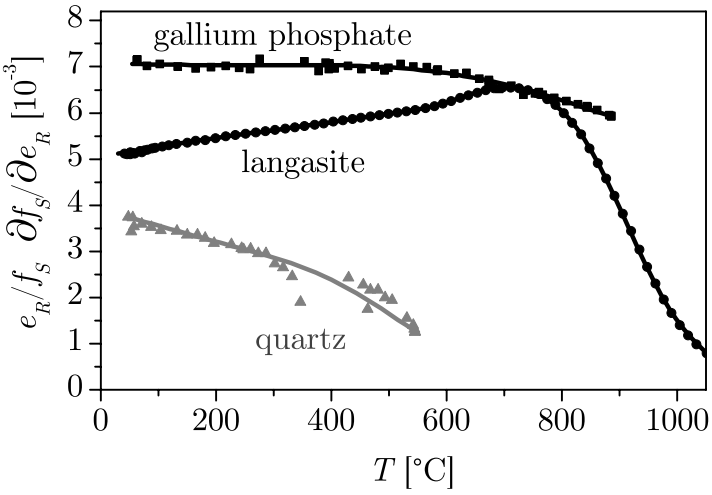

Figure 5.10: The temperature dependent relative derivative of the resonance frequency for the piezoelectric constant of langasite, gallium phosphate and quartz.

Part II

Atomistic Transport

Chapter 6

Defect Chemistry of Langasite

Given langasite's operation temperature of up to at least 1400°C it is worth to explore its defect chemistry and transport mechanisms at high temperatures. The objective is to minimize losses. In contrast, the maximum operation temperatures of $GaPO_4$ and, in particular, of quartz are significantly lower. Further, the availability of $GaPO_4$ is limited which might prevent its large-scale application. Therefore, the followings sections are focussed exclusively on langasite.

In order to take advantage of the high mass sensitivity of langasite resonators, gas atmosphere-independent operation must to be ensured. According to Chapter 5, frequency fluctuations equivalent to noise of ± 4 Hz are defined as criterion to determine the range of stable operation of 5 MHz resonators. Extreme conditions such as

- High temperatures or low oxygen partial pressures and
- High concentrations of hydrogen containing species

potentially cause changes in the most relevant parameters c_{66}, ρ_R, σ_R and η_R and, thereby, frequency shifts larger than the limit mentioned above. The frequency shift might be explained by different scenarios including

- Formation of vacancies which primary impacts the density and potentially the strength of the interatomic bonds leading to modified elastic constants,
- Incorporation of hydrogenous species and
- Increase of the viscosity and conductivity due to the movement of ionic and electronic charge carriers. Thereby, moving ions are expected to show a stronger effect than electrons.

Based on the knowledge of the defect chemistry and the atomistic transport the operation limits as function of temperature have to be explored. Further, the range of oxygen partial pressure independent operation and the impact of hydrogenous species should be derived. If the corresponding defect mech-

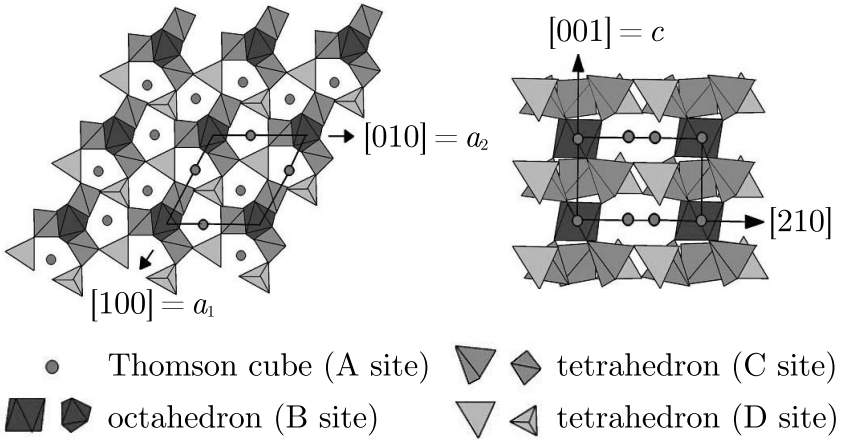

Figure 6.1: $Ca_3Ga_2Ge_4O_{14}$-type crystal structure [26].

anisms are understood, means for achieving improvements of the resonator material can be defined. Such suggestions include e.g. appropriate dopants.

In the following sections it is intended to establish the nature of the carriers contributing to both mass and charge transport. These phenomena are expected to cause reversible variations in stoichiometry of langasite and, thereby, drift of the resonator properties. Other effects which potentially lead to irreversible degradation like gallium evaporation are discussed in Section 7.5.

6.1 Cation Sites

Langasite belongs to the structure type of the trigonal calcium gallium germanate $Ca_3Ga_2Ge_4O_{14}$ as visualized in Fig. 6.1. Due to the presence of four distinct cation sites according to $A_3BC_3D_2O_{14}$, the langasite structure is very complex and allows, therefore, several substitutions. In this regard, langasite is particularly suited as model compound since nearly every size cation can be accommodated on one of its four different cation sites [26]. Layers of vertice-connected C- and D-tetrahedra alternate with layers of A-site Thomson cubes and B-octahedra. A special feature of the langasite structure is the appearance of gallium in the differently coordinated B- and C-sites [88]. The corresponding ions, oxygen coordination numbers and ionic radii are shown in Tab. 6.1.

Appropriate growth conditions have to be chosen to suppress microstructural defects. Nowadays, large and high quality crystals can be grown [11, 21, 89, 90]. Beyond that, the composition of the melt determines the properties of the crystals. Two issues have to be regarded. First and most obviously, the stoichiometry and the purity of the oxide mixture used for the Czochral-

ski growth impacts the defect chemistry. Secondly, the growth process itself impacts the melt composition. Here, the crucial factors are the segregation coefficients and the mass ratio of crystal and melt. Stoichiometry derivations of the melt composition are commonly compensated by the formation of either cation or anion vacancies [32, 91]. For example, the activation energy of the electrical conductivity varies depending on the position where the specimen is taken from the crystal boule (seed end, central part, tail end) by up to about 0.1 eV [32]. The fact underlines that even samples from the same crystal boule exhibit significant differences in their properties. The situation might be even worth if crystals of different size or purchased samples are compared. Here, the mass ratio of crystal and melt and the position in the crystal are under question. In order to exclude the latter problems to some extend, crystals from a single manufacturer (IKZ Berlin, see Appendix C.1) are used predominantly.

Langasite can be doped by a variety of cations. The sites where they substitute into are known [26, 92–94]. Based on the ionic radii and the coordination numbers strontium or praseodymium dopants occupy La^{3+} sites (A site). Under these circumstances, strontium acts as acceptor whereas praseodymium is a neutral substituent or a donor. Niobium replaces Ga^{3+} thereby acting as donor.

Rhodium impurities originating from the growth process in Pt/Rh crucibles are expected to occupy Ga^{3+} sites and act as donor for Rh^{4+} or Rh^{5+} valence states. In case of the absence of acceptors, the charge compensation would be fulfilled by electrons. Another option is the appearance of Rh^{3+} which does not change the charge with respect to the lattice.

Tab. 6.2 lists potential dopants, their coordination numbers and ionic radii. These substitutions are in accordance with the subsequently presented defect model which reflects the effect of these dopants consistently.

Table 6.1: Sites and oxygen coordination of the cations in langasite as well as ionic radii of the cations [74].

site	A	B	C	D	
occupation	La^{3+}	Ga^{3+}	Ga^{3+}	50 % Ga^{3+}	50 % Si^{4+}
oxygen coordination	8	6	4	4	
ionic radii [10^{-10} m]	1.16	0.62	0.47	0.47	0.26

Table 6.2: Sites, potential dopants, their oxygen coordination and ionic radii [74].

site	dopant	oxygen coordination	ionic radii [10^{-10} m]	effect
A	Sr^{2+}	8	1.26	acceptor
A	Pr^{3+}	8	1.13	neutral
A	Pr^{4+}	8	0.96	donor
B	Nb^{4+}	6	0.68	donor
B	Nb^{5+}	6	0.64	donor
C,D	Nb^{5+}	4	0.48	donor
B	Rh^{3+}	6	0.67	neutral
B	Rh^{4+}	6	0.60	donor
B	Rh^{5+}	6	0.55	donor

6.2 Hydrogen Free Atmospheres

Initially, atmospheres containing residual amounts of hydrogen are regarded. In particular, the remaining hydrogen or hydrogenous species should impact the defect chemistry of langasite in a minor way. To realize that, the oxygen partial pressure (p_{O2}) is adjusted by CO/CO_2 gas mixtures.

6.2.1 General Approach

The defect model presented in this section summarizes parts of the detailed description given in [43, 95–97][1]. Key defect reactions are selected whereby the formation of oxygen vacancies $V_O^{\bullet\bullet}$ (Kröger-Vink notation [98]) at low p_{O2} is the most relevant feature with respect to mass changes of the resonator material leading potentially to frequency shifts of resonator devices. These reactions and their mass action laws are the

- Reduction,

$$O_O^{\times} \leftrightarrow V_O^{\bullet\bullet} + 2e' + 1/2\, O_2 \tag{6.1}$$

$$k_R = [V_O^{\bullet\bullet}]\; n^2 p_{O2}^{1/2} \tag{6.2}$$

- Oxidation,

$$1/2\, O_2 + V_O^{\bullet\bullet} \leftrightarrow O_O^{\times} + 2h^{\bullet} \tag{6.3}$$

$$k_O = p^2\, [V_O^{\bullet\bullet}]^{-1}\; p_{O2}^{-1/2} \tag{6.4}$$

- Generation of electrons and holes,

$$null \leftrightarrow h^{\bullet} + e' \tag{6.5}$$

[1] In the following the dissertation [43] is cited, only. It includes essentially the other publications.

$$k_E = n\,p \tag{6.6}$$

- Schottky reaction and

$$null \leftrightarrow 14V_O^{\bullet\bullet} + 3V_{La}''' + 5V_{Ga}''' + V_{Si}'''' \tag{6.7}$$

$$k_S = [V_O^{\bullet\bullet}]^{14} + [V_{La}''']^3 + [V_{Ga}''']^5 + [V_{Si}''''] \tag{6.8}$$

- Anion Frenkel reaction.

$$O_O^\times \leftrightarrow V_O^{\bullet\bullet} + O_i'' \tag{6.9}$$

$$k_F = [V_O^{\bullet\bullet}]\;[O_i'']\,. \tag{6.10}$$

Further, for dopants additional reactions and mass action laws for the

- Ionization of acceptors and

$$A \leftrightarrow A_C' + h^\bullet \tag{6.11}$$

$$k_A = [A_C']\;p \tag{6.12}$$

- Ionization of donors

$$D \leftrightarrow D_C^\bullet + e' \tag{6.13}$$

$$k_D = [D_C^\bullet]\;n \tag{6.14}$$

apply. The subscript C represents cation sites. Manifold charges with respect to the lattice do not have to be introduced since the model describes the experimental findings consistently.

Finally, the general neutrality equation for electrical charges in the crystals

$$2\,[V_O^{\bullet\bullet}] + p + [D_C^\bullet] = 2\,[O_i''] + n + [A_C'] \tag{6.15}$$

must be fulfilled.

The solution of the above set of equations provides the relation between temperature, oxygen partial pressure, dopant level and concentrations c_l of charge carriers indexed by l. The latter enable the calculation of the partial conductivities σ_l provided that their charges q_l and mobilities μ_l are known. Thus, the experimentally accessible total conductivity σ_B follows from[2]

$$\sigma_B = \sum_l \sigma_l = \sum_l q_l\,\mu_l\,c_l. \tag{6.16}$$

The complexity of the set of equations can be reduced by applying the Brouwer approximation [99] where a dominating defect relation is regarded in restricted ranges of temperature and p_{O2}. Accordingly, the neutrality equation includes a single dominating type of positive and negative charge carrier, only.

[2]The property σ_B reflects the bulk conductivity of polycrystalline or single crystalline langasite. In the latter case σ_B equals σ_R.

Even nominally undoped langasite is expected to exhibit some intrinsic non-stoichiometry and, therefore, to behave like net donor or acceptor doped material. Under such circumstances, typical defect regions and their neutrality equations are the

- Reduction,

$$n \approx 2\,[V_O^{\bullet\bullet}] \tag{6.17}$$

- Ionic compensation,

$$2\,[V_O^{\bullet\bullet}] \approx [A'_C] \qquad \text{for} \qquad [A'_C] > [D_C^{\bullet}] \tag{6.18}$$

$$2\,[O_i''] \approx [D_C^{\bullet}] \qquad \text{for} \qquad [D_C^{\bullet}] > [A'_C] \tag{6.19}$$

- Electronic Compensation and

$$p \approx [A'_C] \qquad \text{for} \qquad [A'_C] > [D_C^{\bullet}] \tag{6.20}$$

$$n \approx [D_C^{\bullet}] \qquad \text{for} \qquad [D_C^{\bullet}] > [A'_C] \tag{6.21}$$

- Oxidation.

$$p \approx 2\,[O_i''] \tag{6.22}$$

Among other conclusions, these equations enable the calculation of the p_{O2}-dependence of the charge carrier concentrations. Criteria to identify the partial conductivity σ_l which dominates the total conductivity σ_B are the concentration and the mobility of the different charge carriers. The concentrations can be taken from the defect model. The mobilities of the ions follow from the diffusivities presented in Section 7.1. It turns out that oxygen vacancies are the only ionic carriers which contribute substantially to the conductivity. Of course, electrons (and holes) must be considered since they are in general significantly more mobile than ions.

Taking net acceptor doped material as example, the concentration of oxygen vacancies is fixed according to Eq. 6.18 at sufficiently high p_{O2}. Further, electrons are suppressed which results in predominant ionic conduction carried by oxygen vacancies. Consequently, the dominating charge transport is p_{O2} independent

$$\sigma_B \sim [V_O^{\bullet\bullet}] \neq f(p_{O2}). \tag{6.23}$$

With decreasing p_{O2} electrons are generated and take over the conductivity σ_B even if their concentration is lower than that of oxygen vacancies. The former are expected to be more mobile than oxygen vacancies. Under such circumstances, the p_{O2}-dependence of the electron concentration and, thereby, of the conductivity follow from Eqs. 6.2 and 6.18

$$\sigma_B \sim n \sim p_{O2}^{-1/4}. \tag{6.24}$$

At very low p_{O2} the reduction reaction controls the formation of electrons and oxygen vacancies. The combination of Eqs. 6.2 and 6.17 results in the p_{O2}-dependence

$$\sigma_B \sim n \sim p_{O2}^{-1/6}. \tag{6.25}$$

The slope of the p_{O2}-dependence of the electron concentration in the subsequently presented log-log plots is $\Delta \log n / \Delta \log p_{O2}$ = -1/6.

Calculations for the complete set of equations are presented in [43]. In the following these results are summarized by the Kröger-Vink diagrams for net acceptor and donor doped langasite and given in Figs. 6.2 and 6.3, respectively. The defect regions mentioned above are separated by vertical dashed lines and denoted by the dominating neutrality relation above the diagrams. Further, the modulus of the slope of the curves is indicated in the bottom part of the figures. The appropriate sign and vanishing slopes become obvious from the curves themselves. The example concerning acceptor doped langasite from above corresponds to the left hand regions in Fig. 6.2.

6.2.2 Oxygen Partial Pressure Ranges of Operation

The p_{O2} ranges of operation of langasite must be explored with respect to the general defect model. Chapter 7 provides the corresponding experimental results. At this point it is important to note that the accessible p_{O2} ($1 \ldots 10^{-25}$ bar) and temperature ranges ($700 \ldots 1000$°C) lead to the following regions of operation [43] denoted by

- *AD* in Fig. 6.2 for acceptor (1 % Sr) doped langasite[3].
  Acceptor doped langasite exhibits mixed ionic-electronic conductivity. At low and medium p_{O2}, the charge transport is dominated by mobile oxygen vacancies. The ionic conductivity is fixed by the acceptors, thereby being p_{O2} independent. With increasing p_{O2} p-type electronic conduction takes over the bulk conductivity. The n-type conductivity is fully suppressed.

- *UD* in Fig. 6.2 for nominally undoped langasite.
  Nominally undoped langasite, prepared by ceramic processing routes, shows ionic conduction at medium and high p_{O2}. At low p_{O2}, n-type electronic conductivity becomes pronounced due to the generation of electrons by reduction. The situation corresponds to slightly acceptor doped material. As a consequence, the p_{O2} range of operation is shifted to lower values with respect to the intentionally acceptor doped material.

[3]The amount of dopant is always given as molecular percentage of the target cation site. Strontium and praseodymium dopants refer to lanthanum. Niobium dopants are given with respect to gallium.

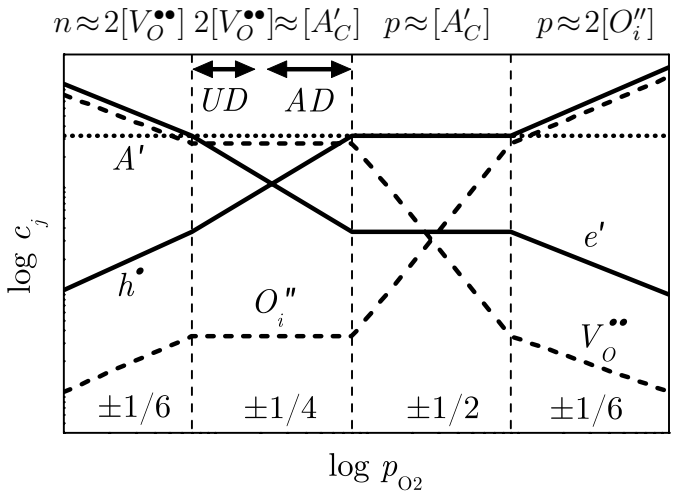

Figure 6.2: Kröger-Vink diagram for net acceptor doped langasite and ranges of operation for nominally undoped (UD) and acceptor doped (AD) langasite taken from [43].

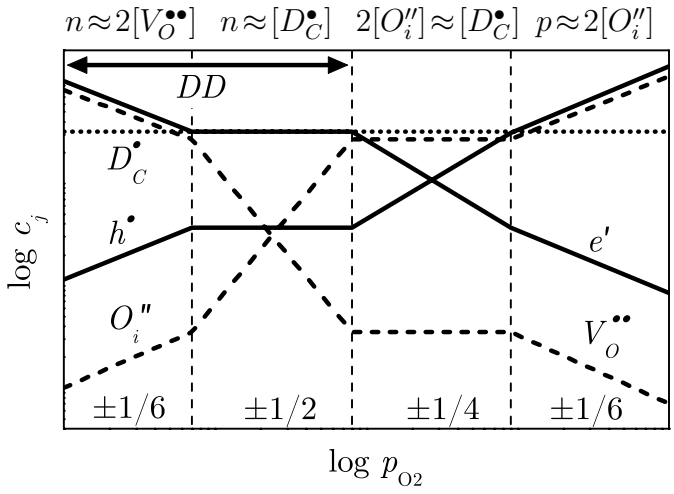

Figure 6.3: Kröger-Vink diagram for net donor doped langasite and range of operation for donor doped (DD) langasite taken from [43].

Table 6.3: Dominating charge carriers in langasite for different net dopant types in the experimentally accessible p_{O2} range and conductivity of langasite as function of p_{O2}.

	nominally undoped[a] $[A'_C] > [D^\bullet_C]$		acceptor doped $[A'_C] > [D^\bullet_C]$		donor doped $[D^\bullet_C] > [A'_C]$	
p_{O2}	neutrality	conduction	neutrality	conduction	neutrality	conduction
low		$n > [V^{\bullet\bullet}_O]$ $\sigma_e > \sigma_V$ $\rightarrow$ electronic $\sigma_B \sim p_{O2}^{-1/4}$				$\mu_n > \mu_V$ $\sigma_e > \sigma_V$ $\rightarrow$ electronic $\sigma_B \sim p_{O2}^{-1/6}$
$\downarrow$				$[V^{\bullet\bullet}_O] \gg n$ $\sigma_V > \sigma_e$ $\rightarrow$ ionic $\sigma_B \neq f(p_{O2})$	$n \approx 2[V^{\bullet\bullet}_O]$	
medium	$2[V^{\bullet\bullet}_O] \approx [A'_C]$		$2[V^{\bullet\bullet}_O] \approx [A'_C]$			
		$[V^{\bullet\bullet}_O] \gg n$ $\sigma_V > \sigma_e$ $\rightarrow$ ionic $\sigma_B \neq f(p_{O2})$				$n > [V^{\bullet\bullet}_O]$ $\sigma_e > \sigma_V$ $\rightarrow$ electronic $\sigma_B \neq f(p_{O2})$
$\downarrow$				$p > [V^{\bullet\bullet}_O]$ $\sigma_e > \sigma_V$ $\rightarrow$ electronic $\sigma_B \sim p_{O2}^{1/4}$	$n \approx [D^\bullet_C]$	
high						

[a] Prepared by ceramic processing routes.

- *DD* in Fig. 6.3 for donor (5 % Nb) doped langasite.
  Donor doped langasite is a n-type electronic conductor in the entire accessible p_{O2} range. At low p_{O2}, the generation of electrons leads to to an increased conductivity with respect to the situation at medium and high p_{O2} where the electron concentration is fixed by the donor doping.

The analytical relations between p_{O2} and total conductivity summarized in Tab. 6.3 are restricted to the specific p_{O2} regions of operation mentioned above. As intermediate information, neutrality equations and dominating charge carriers in langasite are given for the experimentally accessible p_{O2} ranges.

So far, the discussion refers to the temperature and oxygen partial pressure dependence of the bulk conductivity. However, both types of dopants lead to regions of p_{O2} independent conduction determined by either oxygen vacancies or electrons. Consequently, conductivity measurements as function of p_{O2} by oneself are not suited to identify the predominant charge carrier in the entire p_{O2} range. Therefore, accompanying experimental methods are applied and presented in [43] to support the defect model. In particular, thermoelectric power and concentration cell measurements are performed to confirm sign and concentration of the dominant charge carriers and to determine reaction constants and mobilities.

6.2.3 Conductivity Prediction

The detailed analysis presented in [43] enables, for example, to predict the bulk conductivity of langasite as a function of net dopant concentration $[A'_C] - [D^{\bullet}_C]$ for a given temperature. Fig. 6.4 shows the results for 800 and 1000°C which follow essentially the same pattern[4]. As already mentioned, acceptor doped langasite exhibits mixed ionic-electronic conductivity with predominant ionic contributions. Consequently, a weak p_{O2} dependence of the conductivity is observed. Donor doped langasite shows electronic conductivity at all p_{O2} leading to enhanced conduction at low p_{O2}. To reduce the conductivity to a minimum in air, a perfectly compensated langasite is required. This region is indicated in Fig. 6.4 by a gray bar. According to the slope of the curves around $[A'_C] - [D^{\bullet}_C] = 0$, it is, a priori, difficult to predict whether materials processing will result in a predominant ionic or electronic conductivity. For example, nominally undoped polycrystalline langasite prepared by ceramic processing routes, behaves like acceptor doped langasite. The fact applies not necessarily for single crystalline langasite prepared be the Czochralski technique.

Further, the analysis in [43] includes a qualitative description of the oxygen vacancy concentration which enables to calculate mass changes of the

[4] At 800°C the curves for $p_{O2} = 1$ and 10^{-10} bar are almost identical. At 800°C and $p_{O2} = 10^{-20}$ bar the branch for $[A'_C] - [D^{\bullet}_C] < 0$ is not shown in order to avoid confusion because of overlapping curves. It is a nearly horizontal line at $\sigma_B \approx 6 \times 10^{-3}$ S/m.

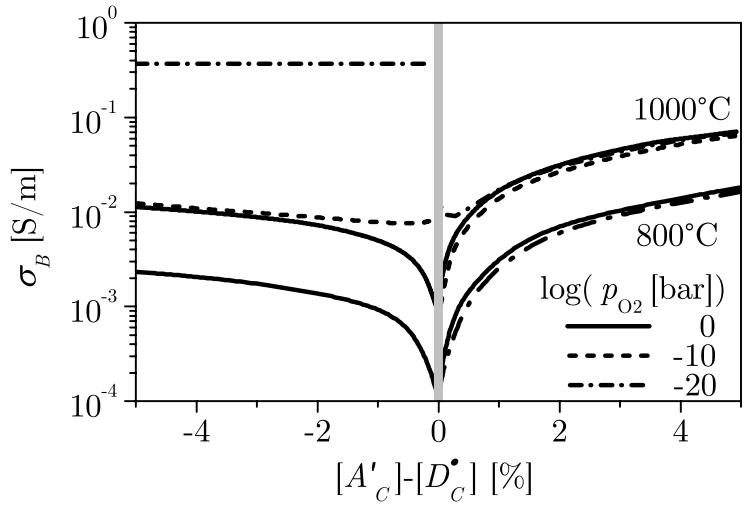

Figure 6.4: Bulk conductivity prediction for langasite at different oxygen partial pressures at 800 and 1000°C as function of net dopant level taken from [43].

resonator material. The formation of oxygen vacancies and electrons follows from the reaction constant according to Eq. 6.2

$$k_{R,A} = [V_O^{\bullet\bullet}]\, n^2 p_{O2}^{1/2} = 10^{67} e^{-5.7\,\mathrm{eV}/k_B T}\ \mathrm{cm}^{-9}\,\mathrm{bar}^{1/2}. \tag{6.26}$$

for acceptor and

$$k_{R,D} = [V_O^{\bullet\bullet}]\, n^2 p_{O2}^{1/2} = 10^{71} e^{-6.57\,\mathrm{eV}/k_B T}\ \mathrm{cm}^{-9}\,\mathrm{bar}^{1/2}. \tag{6.27}$$

for donor doped langasite, respectively. Changes in $[V_O^{\bullet\bullet}]$ can be calculated in concert with the general neutrality condition $2\,[V_O^{\bullet\bullet}] + [D_C^{\bullet}] = n + [A_C']$ applying at low p_{O2}. The related mass change and the resulting frequency shift of langasite resonators are discussed in Chapter 8.

6.3 Hydrogen Containing Atmospheres

The experimental results found in nominally hydrogen free atmospheres are consistent with the defect model presented so far. However, atmospheres containing substantial amounts of hydrogen lead to contradictions if the p_{O2} is lowered. In particular, the conductivity decreases with decreasing p_{O2} as shown by the corresponding experimental results in Section 7.4.2.

Hydrogenous atmospheres are created by H_2/H_2O gas mixtures where the amount of H_2 provided to the reaction chamber ($\sim p_{H2}^{RT}$) is kept constant. As described in Appendix C.2, this condition results in

$$p_{H2O}^{\alpha} \sim p_{O2} \tag{6.28}$$

with $\alpha = 2$ in the marginal case of very low p_{O2}. With increasing p_{O2}, α becomes p_{O2} dependent and increases slightly.

Since langasite belongs to the same crystal class as α-quartz, similar impact of hydrogenous species is expected. In particular, the diffusion along the z-axis should be much faster than in other directions. Oxygen tunnels may be formed [100] where water reacts with e.g. Si-O-Si bonds. From the reaction of water incorporation into the crystal structure via

$$H_2O + O_O \leftrightarrow (2OH)_O, \tag{6.29}$$

the dependence of the conductivity along the z-axis as function of the water vapor partial pressure p_{H2O} is estimated to be

$$\sigma_Z \sim [(OH)_O] \sim p_{\mathrm{H2O}}^{1/2}. \tag{6.30}$$

Eq. 6.30 does not contains effectively charged particles. However, protons can migrate in the electrical field since the OH-groups are polar [101–103].

Further, hydrogen may react with e.g. Si-O-Si bonds according to

$$H_2 + O_O \leftrightarrow (H, OH)_O. \tag{6.31}$$

If both hydrogen atoms contribute to the charge transport in form of mobile protons, the mass action law and Eq. C.3 result in

$$\sigma_Z \sim p_{\mathrm{H2O}}^{1/4}. \tag{6.32}$$

For geometrical reasons, conduction of water through oxygen tunnels is not expected in the y-direction. Defect and transport mechanisms reported e.g. for perovskites [104] can be applied here. There, water incorporation relies on the existence of oxygen vacancies via the reaction

$$H_2O + V_O^{\bullet\bullet} + O_O \leftrightarrow 2(OH)_O^{\bullet}. \tag{6.33}$$

The conductivity depends on both, the water partial pressure and the concentration of oxygen vacancies

$$\sigma_Y \sim [(OH)_O^{\bullet}] \sim p_{\mathrm{H2O}}^{1/2} [V_O^{\bullet\bullet}]^{1/2}. \tag{6.34}$$

At low temperatures, where $[V_O^{\bullet\bullet}]$ is frozen in or where $[V_O^{\bullet\bullet}]$ is fixed by acceptors,

$$\sigma_Y \sim [(OH)_O^{\bullet}] \sim p_{\mathrm{H2O}}^{1/2} \tag{6.35}$$

is expected. With increasing temperature the concentration of oxygen vacancies at sufficiently low p_{O2} depends on the oxygen partial pressure according to $[V_O^{\bullet\bullet}] \sim p_{O2}^{-1/6}$ (see Eqs. 6.2 and 6.17). Using Eq. 6.28, the dependence of σ_Y from p_{H2O} follows

$$\sigma_Y \sim [(OH)_O^{\bullet}] \sim p_{\mathrm{H2O}}^{1/2-\alpha/12}. \tag{6.36}$$

In the limiting case of very low p_{O2} from $\alpha = 2$ results

$$[(OH)_O^\bullet] \sim p_{H2O}^{1/2-0.17}. \tag{6.37}$$

For higher p_{O2} with $\alpha \gtrsim 2$ smaller exponents are expected.

Another option is the formation of protons at the surface of langasite according to

$$H_2 \leftrightarrow 2H^\bullet + 2e'. \tag{6.38}$$

In this case, the conductivity depends on the hydrogen partial pressure p_{H2} as follows

$$\sigma_Y \sim p_{H2}^{1/4} \tag{6.39}$$

and can be related to p_{H2O} using Eqs. C.3 and C.4

$$\sigma_Y \sim p_{H2O}^{1/4-\alpha/8}. \tag{6.40}$$

For very low p_{O2}'s ($\alpha = 2$) a p_{H2O} independent conductivity results if the latter reaction applies. With increasing p_{O2} ($\alpha > 2$) a negative exponent, i.e. decreasing conductivities with increasing p_{H2O} is expected.

The appropriate reactions must be identified experimentally as presented in Section 7.4.2.

Table 6.4: Potential reactions and corresponding p_{H2O} dependent conductivities of langasite.

direction	reaction	conductivity	remark
z	$H_2O + O_O \leftrightarrow (2OH)_O$	$\sigma_Z \sim [(OH)_O] \sim p_{\mathrm{H2O}}^{1/2}$	
	$H_2 + O_O \leftrightarrow (H, OH)_O$	$\sigma_Z \sim p_{\mathrm{H2O}}^{1/4}$	
y	$H_2O + V_O^{\bullet\bullet} + O_O \leftrightarrow 2(OH)_O^{\bullet}$	$\sigma_Y \sim p_{\mathrm{H2O}}^{1/2}$	low temperature ($[V_O^{\bullet\bullet}] = const$)
		$\sigma_Y \sim [(OH)_O^{\bullet}] \sim p_{\mathrm{H2O}}^{1/2-\alpha/12}$	high temperature ($[V_O^{\bullet\bullet}] \sim p_{\mathrm{O2}}^{-1/6}$)
y	$H_2 \leftrightarrow 2H^{\bullet} + 2e'$	$\sigma_Y \sim p_{\mathrm{H2O}}^{1/4-\alpha/8}$	high p_{O2} ($\alpha > 2$)
		$\sigma_Y = const.$	low p_{O2} ($\alpha = 2$)

Chapter 7

Mass and Charge Transport

Mass and charge transport in langasite are evaluated to support the defect model. First, the diffusivities of the relevant constituents and of potential dopants are presented. These results point to the most mobile charge carriers and enable to calculate the time constants of equilibration processes. Secondly, conductivity measurements in nominally hydrogen free and in hydrogenous atmospheres are determined and discussed in concert with the defect model. Further, the impact of dopants is demonstrated.

Whenever possible, diffusion experiments and conductivity measurements are performed using langasite single crystals. However, the preparation of doped samples and the need to achieve reasonable equilibration times require, in some cases, the application of polycrystalline samples.

7.1 Diffusive Transport

7.1.1 Oxygen Diffusion

The oxygen self-diffusion in langasite is studied in the temperature range from 600 to 1000°C by oxygen isotope exchange experiments using $^{18}O_2$ enriched atmospheres and subsequent analysis of the ^{18}O depth profiles by secondary ion mass spectrometry (SIMS). Details about the experiments and the data evaluation are given in Appendix C.5. The correlation factor for the diffusion of the oxygen tracer is close to unity for a vacancy mechanism. Therefore, the tracer diffusion coefficient and the chemical diffusion coefficient are are not distinguished.

Fig. 7.1 shows the results for single crystalline (*sc*) and polycrystalline (*pc*) langasite in form of an Arrhenius plot. For the single crystals, the diffusion coefficients along the y-direction are given[1]. The plot indicates that oxygen diffusion is controlled by a single mechanism in the temperature range

[1]The values for the z-direction are slightly larger (not shown).

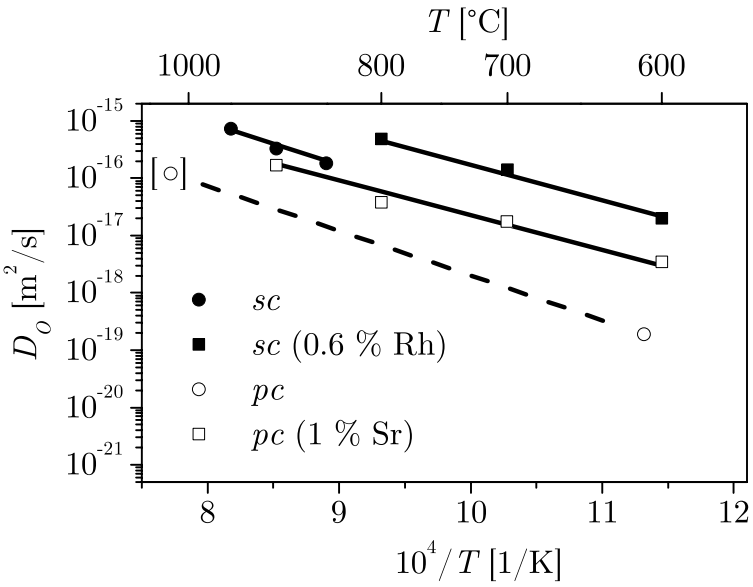

Figure 7.1: Arrhenius plot of the oxygen diffusion coefficients. The curves denoted by *pc* and *sc* correspond to polycrystalline and single crystalline material, respectively. Considerable amounts of dopants are given in parenthesis.

from 600 to about 1000°C, i.e. the activation energy E_A according to

$$D_O = D_0 e^{-E_A/k_B T} \tag{7.1}$$

is constant for the respective sample. Tab. 7.1 summarizes the values of E_A and of the temperature independent pre-exponential factor D_0.

Small differences in magnitude and activation energy of the oxygen diffusion coefficients are observed for nominally undoped and 0.6 % Rh containing langasite single crystals. According to Tab. 6.2, rhodium impurities could be neutral or act as donor. In the latter case, the electron concentration is

Table 7.1: Activation energy and pre-exponential factor of diffusion in langasite.

langasite	species	E_A [eV]	D_0 [m^2/s]	temperature range [°C]
sc	^{18}O	1.25	7.6×10^{-6}	750 . . . 950
sc (0.6 % Rh)	^{18}O	1.22	2.5×10^{-6}	600 . . . 800
pc (1 % Sr)	^{18}O	1.20	2.6×10^{-7}	600 . . . 900
sc	^{71}Ga	3.33	9.1×10^{-8}	750 . . . 1000
sc	Sr, Pr	4.50	1.1×10^{-4}	1200 . . . 1450
sc	Nb	1.83	2.8×10^{-8}	900 . . . 1400

expected to be increased thereby suppressing the oxygen vacancy concentration and oxygen diffusion. The facts become obvious from Eqs. 6.21 and 6.2, respectively. However, the experimental findings point to the inverse case leading to the conclusion that rhodium is neutral. The differences observed in Fig. 7.1 may be related to other background impurities, intrinsic non-stoichiometries of the crystals or insufficient pre-annealing of the samples.

The calculated diffusion coefficients of polycrystalline langasite are lower than that of the single crystals. This discrepancy is potentially caused by the large error in estimation of diffusion coefficients in polycrystalline samples using the technique described in Appendix C.5. The approach requires high quality data. For the polycrystalline specimens which show a relatively low density, tracer diffuses rapidly through the pores by gas phase diffusion, thereby implying a very high boundary diffusion which effectively masks bulk contributions. Therefore, only two (less reliable) data points could be extracted for nominally undoped polycrystals. Niobium doped langasite shows even higher porosities which prevents any reasonable data evaluation.

Sr doped samples could be evaluated. The addition of the acceptor, in this specific example 1 % Sr, markedly increases the oxygen diffusion. The observation supports the defect model since acceptor doped langasite is expected to show an even higher ionic conductivity due to the increased oxygen vacancy concentration according to Eq. 6.18.

For completeness, the surface exchange coefficients K_O of nominally undoped langasite crystals are given in Fig. 7.2. Most important, the oxygen transport is dominated by diffusion as it becomes obvious by comparison of the surface exchange related flux with the diffusive flux in the vicinity of the surface. The relation

$$k_O \left(c_G - c_S\right) > D \frac{\partial c}{\partial x_2}\bigg|_{x_2=0} \tag{7.2}$$

is fulfilled for the experimental conditions chosen here. Thereby, the concentration of the tracer in the gas phase and the concentration of the tracer in the sample close to the surface are denoted by c_G and c_S, respectively. In contrast to the oxygen diffusivity, the surface exchange kinetics is found to be slightly p_{O2} dependent.

The values of the oxygen diffusion coefficients are possibly underestimated due to insufficient equilibrium of the oxygen stoichiometry. The pre-annealing runs are performed at the same temperature as the subsequent diffusion runs, only. The situation might correspond to some extend to the electrical conductivity of insufficiently pre-annealed as described in Section 7.2.

7.1.2 Hydrogen Diffusion

Hydrogen or hydrogenous species are generally suspected to contribute substantially to the mass and charge transport [105]. Therefore, their chemical

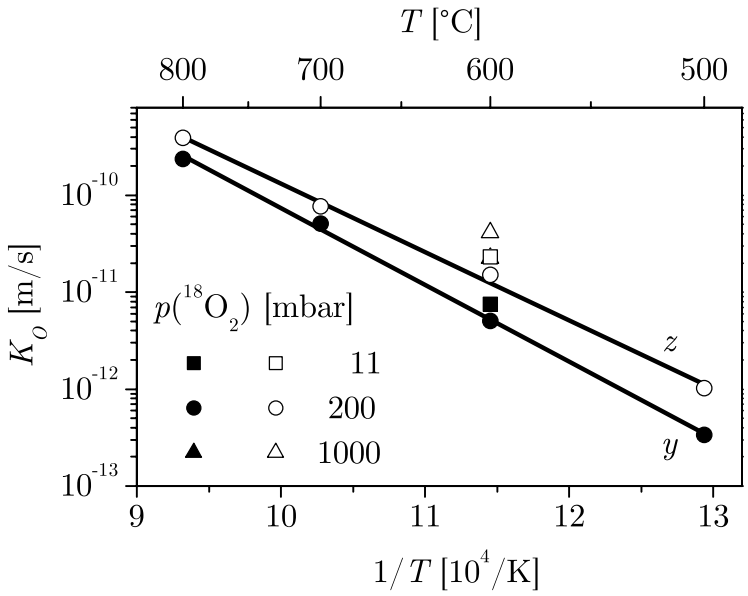

Figure 7.2: Oxygen surface exchange coefficients of nominally undoped langasite crystals in y- and z-direction.

diffusion is investigated. The annealing of the samples in 6 % H_2/Ar results in very flat depth profiles even if the annealing time is in the order of minutes, only. Within the depth accessible by SIMS[2], the concentration does not show significant changes. Further, the penetration of hydrogenous species from both surfaces of the sample overlaps potentially. As a consequence, the data cannot be evaluated using Fick's second law. Alternatively, the time dependent hydrogen content inside the samples can be used to estimate the diffusion coefficient. The approach bases on the description of the total content of the diffusing species as function of its diffusion coefficient and annealing time. The approach and its reduction to practice using the actual samples are described in [106] and [80], respectively. Thereby, the OH-content is determined by Fourier Transform InfraRed (FT-IR) spectroscopy using the absorption peak at 3400 cm^{-1}. The 0.5 mm thick samples are annealed in 6 % H_2/Ar at 600°C for different periods of time and subsequently analyzed. The resulting normalized OH-content is shown in Fig. 7.3. For reference, the OH-content is determined by SIMS. However, the data are not reliable since the system was operated close to the resolution limits. The fact causes the large scattering of these data points in Fig. 7.3.

The diffusion coefficient found at 600°C is 1.12×10^{-11} m^2/s. The value is orders of magnitude higher than that of oxygen. Therefore, a dominant role of hydrogen must be encountered.

[2]In practice, the depth of measurement is limited to several micrometers. Line scans are not considered due to the need to prepare cross-sections of the samples.

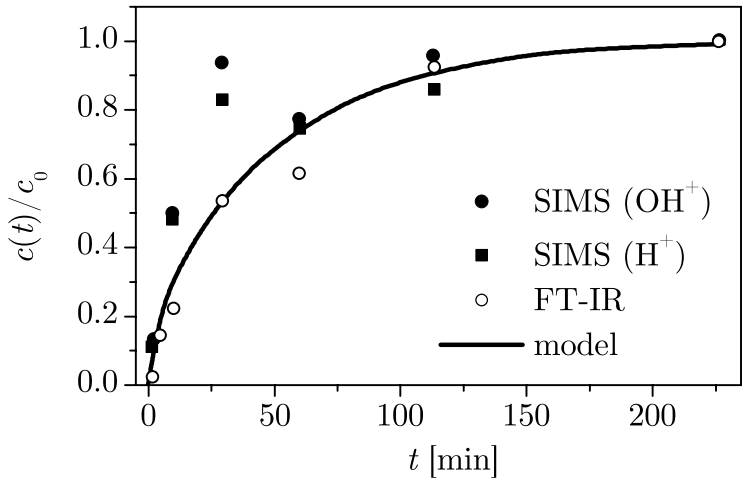

Figure 7.3: Normalized OH-content of single crystalline langasite as function of time during annealing in 6 % H_2/Ar at 600°C [80].

7.1.3 Cation Diffusion

Gallium is known to contribute substantially to the ionic conduction in systems such as $NdAlO_3$-$NdGaO_3$ [107] and (La,Sr)(Ga,Ni)O_3 [108] and, therefore, suspected to play a significant role in langasite. Consequently, the diffusivity of gallium must be determined to evaluate its contribution to the ionic conductivity. Contrary, silicon is, in general, covalent and lanthanum is large. Therefore, it is unlikely that both ions migrate easily within langasite.

The gallium self-diffusivity is determined in single crystalline langasite by implantation of the stable isotope ^{71}Ga, subsequent annealing and depth profile analysis. Details about the data evaluation are given in Appendix C.5.

Fig. 7.4 shows the resulting diffusion coefficients. The activation energy of 3.13 eV is significantly higher than that of oxygen diffusion. Moreover, the gallium diffusion is orders of magnitude less than the oxygen diffusion. Therefore, gallium does not contribute significantly to conduction and can be dismissed from that standpoint. The related surface exchange coefficient is discussed in Section 7.5.

Further, the chemical diffusion of potential dopants is investigated. Their diffusivity is of interest since local doping is an option to form highly conductive areas or to modify the rate of chemical etch processes. These diffusion coefficients are determined using thin films as source for the diffusing species.

The diffusion coefficients of strontium, praseodymium and niobium are fairly small as shown in Fig. 7.4. Remarkably, strontium and praseodymium exhibit virtually the same diffusivity which is consistent with their similar ionic radii and the occupation of the same site in the langasite lattice.

The characteristic diffusion depth along the y-axis y_D can be estimated

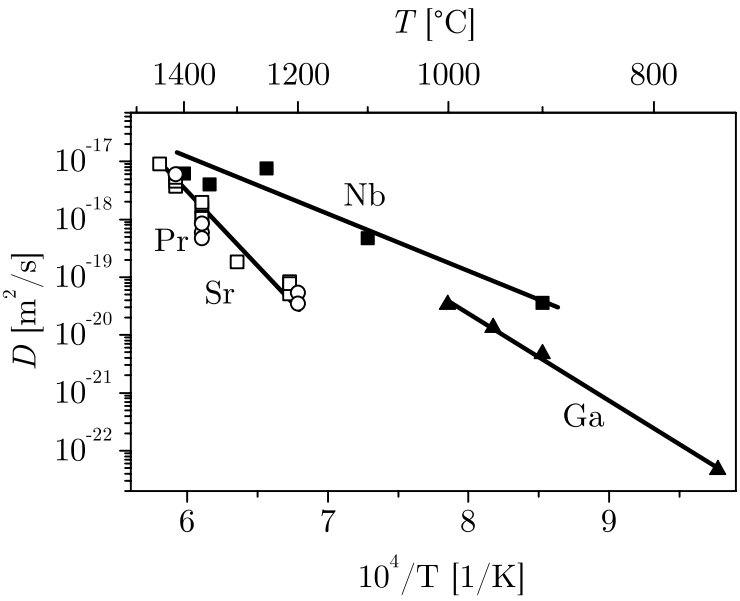

Figure 7.4: Arrhenius plot of the diffusion coefficients of gallium and potential dopants along the y-direction in langasite single crystals.

from the diffusion coefficient and the annealing time t according to

$$y_D = 2\sqrt{Dt}. \tag{7.3}$$

At 1400°C, where the diffusion coefficients of strontium, praseodymium and niobium are quite similar, a diffusion depth of 5 μm requires annealing periods of several days. Consequently, the preparation of locally doped langasite samples by thermal diffusion might be time consuming and prevent the application of the method. Alternatives are the epitaxial deposition of doped langasite layers [109] or the field enhanced diffusion. Contrary, once the doping is performed, operation temperatures of 900°C virtually do not change the extent of the doped region. For example, y_D increases for strontium or praseodymium from 3.0 to 3.1 μm within 4000 years.

7.2 Equilibration Times

7.2.1 Oxygen Diffusion

Single crystalline langasite samples exhibit time dependent materials properties as long as they are not heated to high temperatures. To quantify this fact, the minimum temperature for achieving equilibrium conditions of the oxygen stoichiometry can be estimated by solving Eq. 7.3 for $D(T)$. Taking the thickness of a 5 MHz langasite resonator $y_D = d_R/2 \approx 135$ μm and equilibration times in the order of several hours as example, temperatures of at

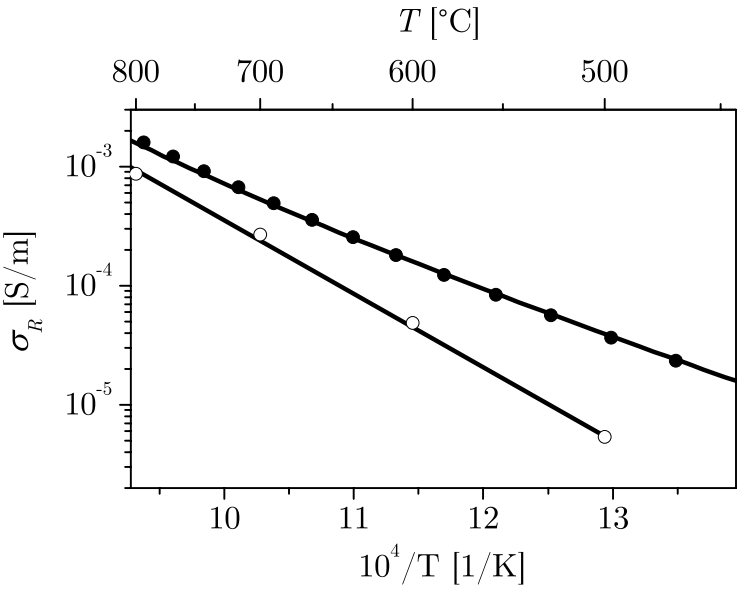

Figure 7.5: Electrical conductivity of single crystalline langasite without (open symbols) and with pre-annealing at 1050°C (solid symbols).

least 1050°C are required[3]. As a consequence, the single crystalline samples presented in this work are pre-annealed for at least 24 h at or above 1050°C. Exceptions are indicated.

Contrary, below about 1000°C equilibrium conditions for oxygen stoichiometry cannot be expected within reasonable periods of time for the given dimensions of the langasite crystals. The fact is particulary unfavorable for p_{O2} dependent conductivity measurements. Dimensions in the order of few micrometers would be required[4]. Alternatively, polycrystalline langasite samples obviously providing fast transport paths can be used for such measurements. These insights motivate the fundamental decision to evaluate the defect chemistry of langasite based on polycrystalline samples.

However, polycrystalline samples do not enable the investigation of piezoelectric properties. Single crystals must be applied which results to some extend in time dependent materials properties. One example is already given in the context of the dielectric constant in Section 4.2.1. Another example is shown in Fig. 7.5 where the first annealing for several hours at 1050°C shifts the conductivity to higher values.

Pre-annealing does not solve the problem of non-equilibration at medium and low temperatures. However, relatively strong fluctuations of the materials properties occurring during the first annealing are not observed anymore.

[3]Use of an extrapolated oxygen diffusion coefficient according to Eq. 7.1.

[4]Micro-machined langasite samples with appropriate dimensions are just recently available and could be the subject for future investigation of the defect chemistry.

Therefore, the use of pre-annealed single crystalline samples is the only feasible option to determine the piezoelectric properties. In order to recognize potential errors, special attention must be drawn on time dependent fluctuations of the properties. At this point it should be noted that long term experiments at 600°C do not indicate fluctuations of the piezoelectric properties.

7.2.2 Hydrogen Diffusion

The hydrogen diffusion coefficient of 1.12×10^{-11} m^2/s at 600°C enables to estimate the time to saturate langasite with hydrogen or hydrogenous species at that temperature. Taking again the thickness of a 5 MHz langasite resonator $y_D = d_R/2 \approx 135$ μm, the calculation according to Eq. 7.3 results in 108 min. The saturation time at higher temperatures is even shorter. Consequently, time independent conditions with respect to the hydrogen content of the samples could be realized easily during the experiments in hydrogenous atmospheres.

7.3 Ionic Conductivity

The cation diffusion data indicate that oxygen ions are the only ionic charge carriers which might contribute significantly to the total electrical conductivity. Assuming an oxygen transport mechanism via oxygen vacancies, the contribution of oxygen transport

$$\sigma_O = q_V [V_O^{\bullet\bullet}] \mu_V \tag{7.4}$$

to the total conductivity may be calculated based on the measured oxygen tracer diffusion. The oxygen vacancy concentration $[V_O^{\bullet\bullet}]$ and mobility μ_V can be eliminated using the Einstein relation [110, 111]

$$\frac{k_B T}{q_V} \mu_V = D_V \tag{7.5}$$

and

$$D_O [O_O] = D_V [V_O^{\bullet\bullet}] \tag{7.6}$$

where k_B, T, $[O_O]$, $q_V = 2q$ and D_V are the Boltzmann constant, the absolute temperature, the oxygen concentration, the charge of the mobile species and vacancy diffusion coefficient, respectively. The calculation yields

$$\sigma_O = \frac{(2q)^2}{k_B T} [O_O] D_O. \tag{7.7}$$

At 800°C, σ_O results in 2.1×10^{-4} S/m. The value corresponds to about 15 % of the total conductivity as it can be seen in Fig. 7.6. At 600°C an ionic

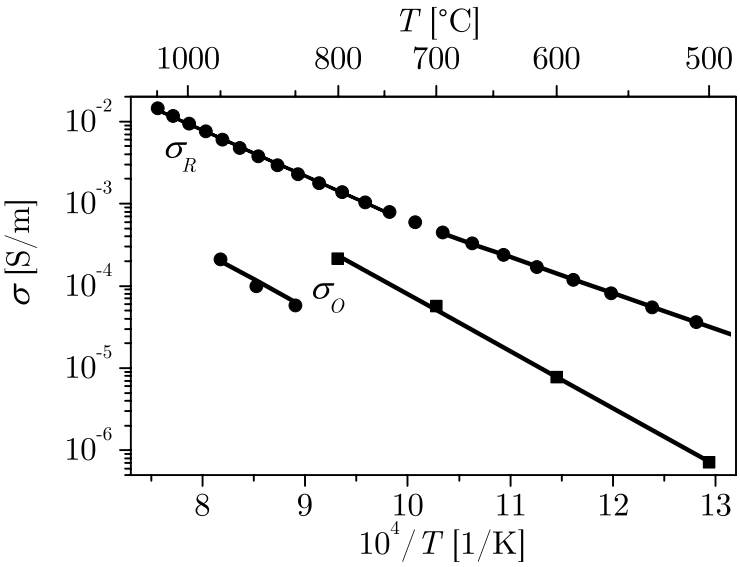

Figure 7.6: Total bulk and oxygen ion conductivities in langasite as a function of reciprocal temperatures.

contribution of 5 % is found. These values are possibly underestimated as discussed in Section 7.1.1. Therefore, the ionic conduction might contribute even stronger to the total conductivity.

7.4 Electrical Conductivity

The electrical conductivity of langasite is measured in the temperature range from 400 to 1050°C. In the first part of this section, the conductivity data of polycrystalline langasite presented in [43] are summarized. These results are compared with that of single crystalline langasite in the second part.

Assuming diffusive transport which is appropriate for either ionic or electron hopping, the activation energy of the process is preferably derived from the temperature dependence of the conductivity-temperature product (see Eq. 7.5). In case of e.g. electron migration, the activation energy is directly related to the conductivity and extracted from its temperature dependence. Since the dominant process is, a priori, not clear the plots show in general the conductivity. Nevertheless, the activation energy is determined from the conductivity-temperature product whenever applies.

7.4.1 Hydrogen Free Atmospheres

Polycrystalline Langasite

Nominally undoped polycrystalline langasite exhibits p_{O2} independent conductivity at medium and high p_{O2} as visualized in Fig. 7.7. Accompanying concentration cell and thermoelectric power measurements confirmed the dominance of ionic conduction [43].

With decreasing p_{O2}, the conductivity increases indicating predominant electronic conduction. The $-1/4$ slope in the log−log plot as predicted by Eq. 6.24 (see also Tab. 6.3) becomes obvious by subtracting the ionic part from the total conductivity (not shown).

Donor doped polycrystalline langasite shows a p_{O2} independent conductivity at medium and high p_{O2}, too. However, the accompanying concentration cell and thermoelectric power measurements points to predominant electronic conduction. With decreasing p_{O2}, the defect model predicts an even enhanced electronic conduction with a $-1/6$ slope which is confirmed in Fig. 7.8.

The conductivity of acceptor doped langasite is shown in Fig. 7.9. In contrast to the nominally undoped and the donor doped material, the p_{O2} independent conductivity occurs at low and medium p_{O2}. Here, ionic conduction dominates. Further, the plot indicates p-type electronic conduction at high p_{O2}. The expected 1/4 slope (see Tab. 6.3) becomes obvious by subtracting the ionic part from the total conductivity (not shown).

The comparison of Figs. 7.7–7.9 shows almost identical conductivities of nominally undoped and donor doped polycrystalline langasite in the p_{O2} independent range, i.e. at medium p_{O2}. The equality is seen as coincidental phenomenon since the predominant charge carrier type differs. At low p_{O2}, donor doping leads to enhanced electronic conduction.

Acceptor doping increases the conductivity by about one order of magnitude at medium p_{O2} as illustrated in Fig. 7.10. The fact goes along with the increase in oxygen diffusion by about one order of magnitude as seen in Fig. 7.1 for polycrystalline langasite and confirms the dominance of ionic conduction. Further, the result corresponds to the conductivity prediction according to Fig. 6.4 for an increase in net donor concentration from $[A'_C] - [D^{\bullet}_C] \gtrsim 0$ to 1 % Sr. These statements remain largely true for high p_{O2}. Even at $p_{O2} = 0.2$ bar, the p-type electronic conduction causes an increase in conductivity of about 7 %, only. Fully p-type conduction is expected for higher doping levels and/or higher p_{O2}.

In the p_{O2} independent range, the temperature dependence of the conductivity-temperature product enables to extract the activation energy of the ionic transport in nominally undoped and acceptor doped langasite. The property is visualized in Fig. 7.11. The activation energy of the electron transport in donor doped langasite is found to be 0.91 eV which is interpreted as sum of donor ionization and electron migration energies [43]. The

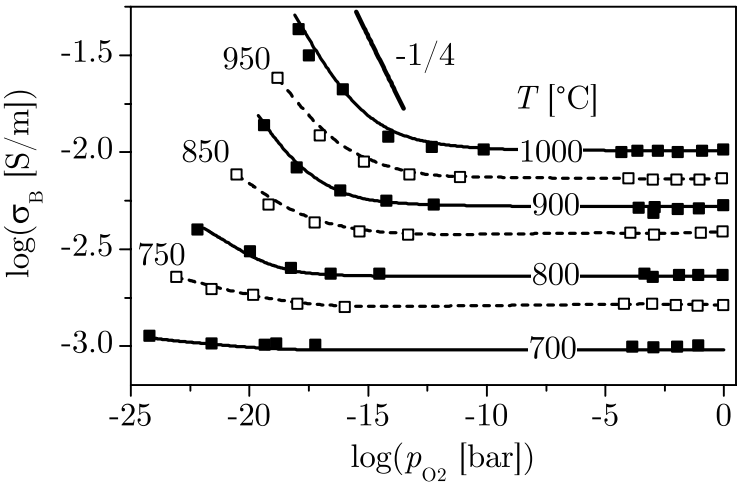

Figure 7.7: Oxygen partial pressure dependent conductivity of nominally undoped polycrystalline langasite taken from [43].

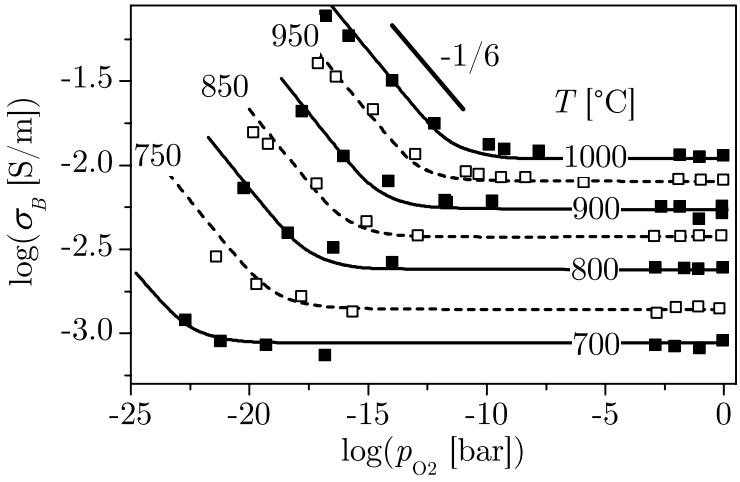

Figure 7.8: Oxygen partial pressure dependent conductivity of donor doped polycrystalline langasite (5 % Nb) taken from [43].

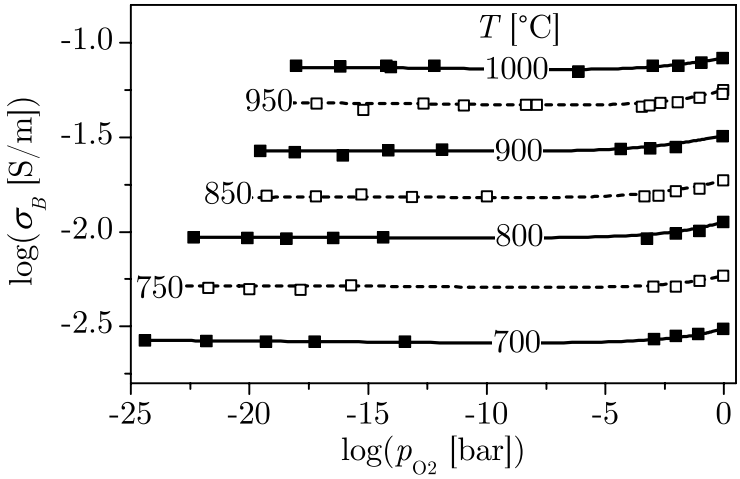

Figure 7.9: Oxygen partial pressure dependent conductivity of acceptor doped polycrystalline langasite (1 % Sr) taken from [43].

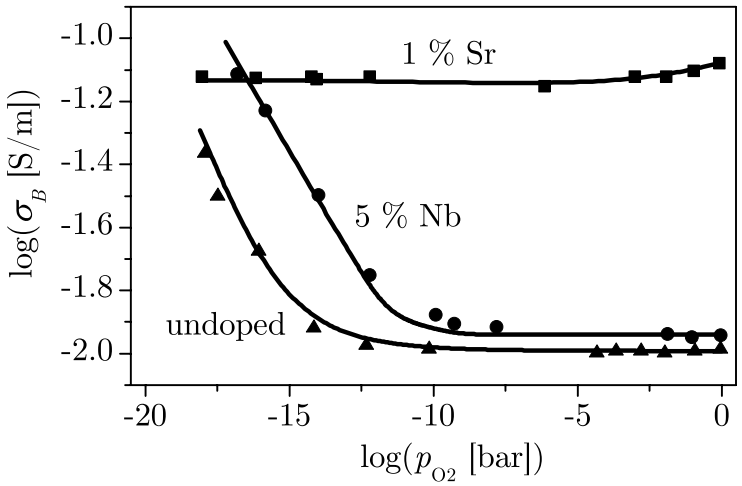

Figure 7.10: Oxygen partial pressure dependent conductivity at 1000°C for nominally undoped, acceptor (1 % Sr) and donor (5 % Nb) doped polycrystalline langasite.

activation energy for strontium doped langasite is significantly larger which goes along with the activation energy of the oxygen diffusion. Numerical values for the activation energies are summarized in Tab. 7.2.

Single Crystalline Langasite

First, the magnitude of the conductivity of nominally undoped single crystalline and polycrystalline langasite is compared. Fig. 7.12 shows orientation dependent conductivities for the single crystalline material which differ by about one order of magnitude. The effective conductivity of polycrystalline materials results from the statistical orientation of the grains. The limits are given by [112]

$$\sqrt[3]{\sigma_x^2 \sigma_z} \leq \sigma_B \leq \frac{1}{3}(2\sigma_x + \sigma_z) \tag{7.8}$$

and indicated in Fig. 7.12. It is clearly obvious that the measured conductivity of polycrystalline langasite falls within these limits. Consequently, the differently prepared materials satisfy this condition necessary to be comparable.

The electrical conductivity of undoped langasite as presented in Fig. 7.13 shows a clear change in activation energy at about 700°C. The observation is highly remarkable since it indicates a change in the dominant conduction mechanism. The suspicion is supported by the following arguments:

- The electronic conduction dominates below about 700°C. The comparison with the ionic conductivity as done in Section 7.3 supports this

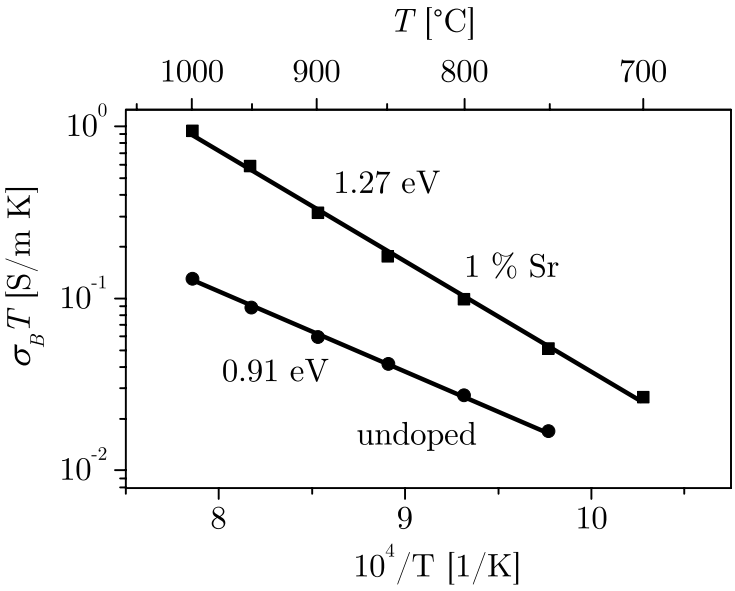

Figure 7.11: Arrhenius plot of the conductivity-temperature product for nominally undoped and acceptor (1 % Sr) doped polycrystalline langasite in the p_{O2} independent range and indication of the respective activation energy.

Table 7.2: Activation energy of the conductivity in langasite in the p_{O2} independent range.

langasite	property	E_A [eV]	temperature range [°C]
sc	σ_B	0.82	400 ... 700
	$\sigma_B T$	1.15	700 ... 1050
sc (0.5 % Sr)	$\sigma_B T$	0.98	400 ... 550
	$\sigma_B T$	1.39	550 ... 950
sc (0.5 % Nb)	σ_B	0.91	400 ... 550
	σ_B	1.29	550 ... 950
pc	$\sigma_B T$	0.91	750 ... 1000
pc (1 % Sr)	$\sigma_B T$	1.27	700 ... 1000
pc (5 % Nb)	σ_B	0.91	700 ... 1000

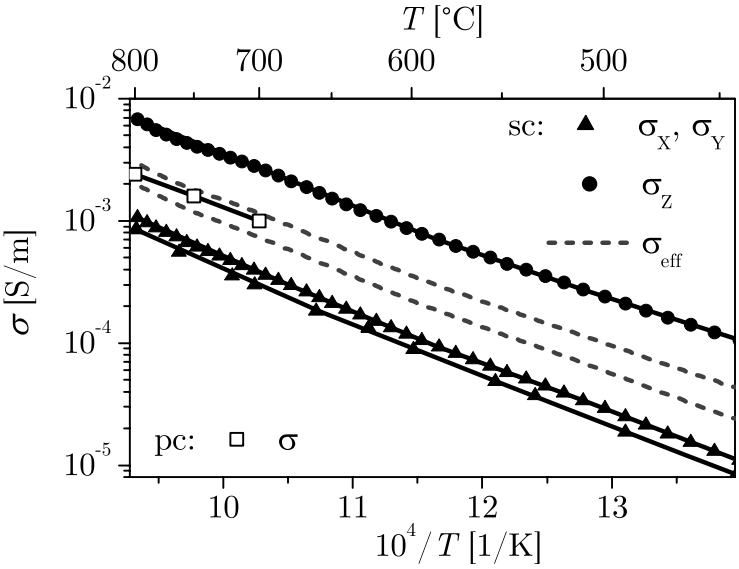

Figure 7.12: Electrical conductivity of langasite single crystals ($\sigma_x = \sigma_y$ and σ_z) and of polycrystalline langasite (σ_B) at $p_{O2} = 0.2$ bar. The predicted range of the effective conductivity of polycrystalline langasite (σ_{eff}) is indicated.

statement. Further, the activation energy of the total conductivity of n-type polycrystalline (donor doped) and single crystalline langasite is close and, in particular, lower than that of the oxygen diffusion. The facts become obvious by the values in Tabs. 7.2 and 7.1.

- The ionic conduction takes over the total conductivity above about 700°C. The activation energy of the oxygen diffusion is found to be higher than that of the electronic conduction which leads to an increased impact of the former with increasing temperature. Further, similar activation energies of the total conductivity and the oxygen diffusion are observed in this temperature range.
- The previous arguments are strongly supported by a direct demonstration of the change in dominating charge carrier type by measurements of the ionic transfer number [113]. The effect is shown at 720°C for the langasite-related compound langatate ($La_3Ta_{0.5}Ga_{5.5}O_{14}$).

These arguments turn the above mentioned suspicion in a fact, i.e. the conduction in the nominally undoped langasite prepared by the Czochralski technique is dominated by electronic carriers below 700°C and turns in predominant ionic conduction above that temperature. In other words, the material behaves like net donor and acceptor doped langasite below and above 700°C, respectively. Since undoped langasite is always operated close to this transition, the presumably strong effect of moving oxygen ions on damping must be expected even at low temperatures.

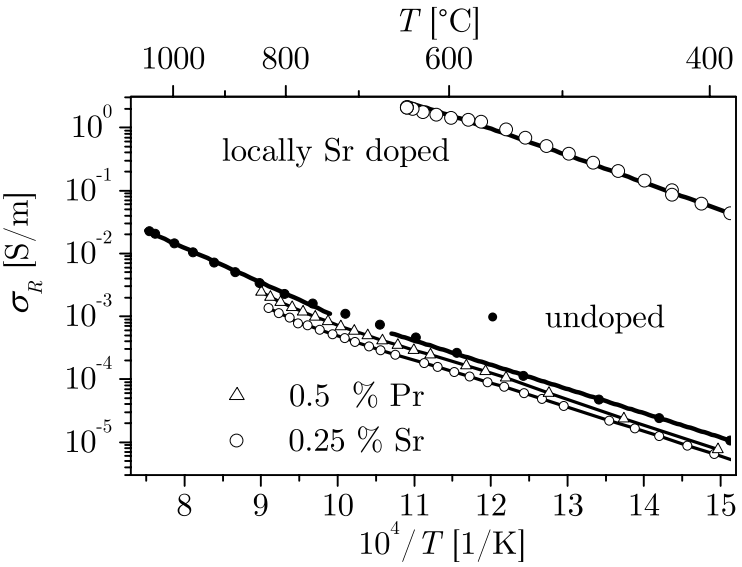

Figure 7.13: Conductivity of nominally undoped, 0.25 % Sr and 0.5 % Pr doped single crystalline langasite as well as conductivity of a strontium doped layer at $p_{O2} = 0.2$ bar.

Further, the impact of dopants must be discussed. Fig. 7.13 compares the conductivity of nominally undoped, 0.25 % Sr and 0.5 % Pr doped langasite single crystals. It becomes obvious that light doping changes the conductivity in a minor way. The defect model predicts a relatively weak impact of the dopant concentration if the material is not perfectly compensated. Assuming for example $[A'_C] - [D^{\bullet}_C] = -1$ %, the increase of the acceptor concentration by 0.25 % would decrease the conductivity by a factor of 0.84 (see Fig. 6.4). Donor doping by 0.5 % would increase the conductivity by a factor of 1.18. Such changes are hardly measurable. The conductivity change of niobium doped langasite goes along with the expected trend. The letter statement does not apply for praseodymium doped langasite. Therefore, it is under question, if praseodymium is ionized thereby acting as donor (see Tab. 6.2). In order to exclude the latter option, further attempts to dope langasite by donors are done using niobium. Its effect on the conductivity is already demonstrated in case of polycrystalline langasite.

The expected effect of strontium on the conductivity is verified by locally doped areas which are prepared by inward diffusion of strontium using SrO as source. The langasite samples evaluated here exhibit a strontium concentration of up to $6{\times}10^{21}$ cm^{-3} in an effectively 2.7 μm thick surface layer. About 60 % of lanthanum are expected to be replaced by strontium which is in agreement with the option to replace lanthanum largely [26]. The conduc-

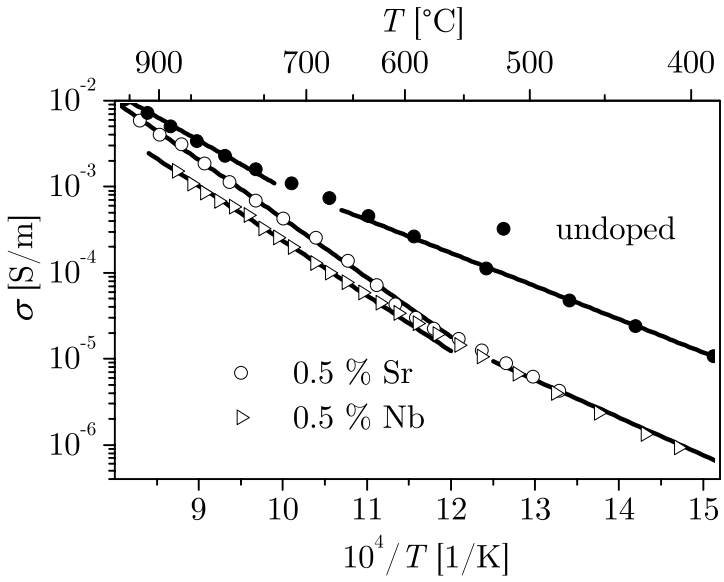

Figure 7.14: Conductivity of nominally undoped, 0.5 % Sr and 0.5 % Nb doped single crystalline langasite at $p_{O2} = 0.2$ bar.

tivity prediction according to Fig. 6.4 points to an increase in conductivity by some orders in magnitude if langasite is highly acceptor doped. The expectation corresponds to the measured change in conductivity of the locally doped area by three to four orders in magnitude as visualized in Fig. 7.13[5]. The result confirms the effect of strontium doping predicted by the defect model. However, quantitative comparisons should not be given since the extrapolation of the conductivity prediction to high dopant levels as well as the determination of the conductivity of the doped area is a rough estimation, only.

Further, a second homogenously doped langasite crystal containing 0.5 % Sr is investigated. The material shows a considerable decrease in conductivity as visualized in Fig. 7.14. However, it cannot be decided whether the material is net donor or acceptor doped. The two branches for $[A'_C] - [D^{\bullet}_C] \lessgtr 0$ in Fig. 6.4 show identical conductivities for doping levels of different sign. The activation energy delivers the required information. The value of 1.39 eV for σT (see Tab. 7.2) indicates ionic conduction in the temperature range from 550 to 950°C since it corresponds roughly to the activation energy of the oxygen diffusion and the conductivity of strontium doped polycrystalline material.

Doping with 0.5 % Nb is performed in order to explore the effect of donors. Niobium doped langasite shows a lower conductivity than undoped single crystals. Obviously, the material is effectively compensated. Remarkably, the

[5]The impact of the underlaying undoped langasite is corrected.

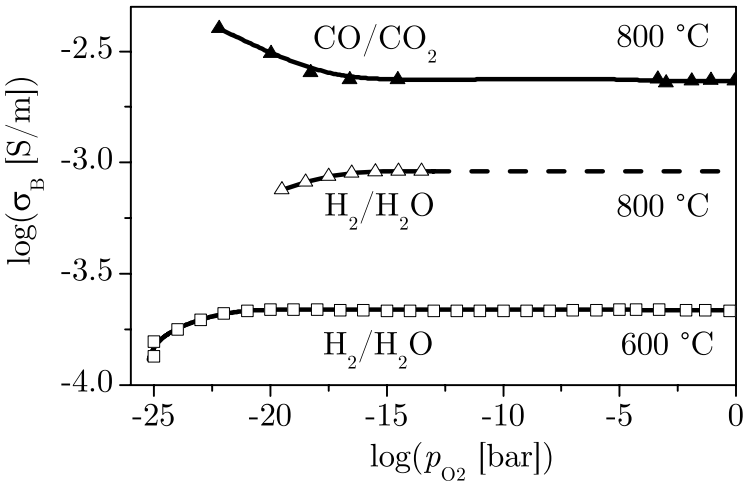

Figure 7.15: Oxygen partial pressure dependent conductivity of langasite in hydrogenous and nominally hydrogen free atmospheres.

activation energy of the conduction is lower than that of strontium doped langasite thereby indicating suppressed ionic conduction. The observation supports the defect model. As a consequence, the material is expected to show lower losses than nominally undoped or strontium doped langasite. The statement originates from the presumably stronger interaction of moving oxygen ions and lattice in comparison to that of electrons and lattice. Related discussions follow in Section 8.

7.4.2 Hydrogen Containing Atmospheres

The p_{O2}-dependence of the conductivity in hydrogenous atmospheres differs from that in nominally hydrogen free atmospheres. The fact is visualized in Fig. 7.15 where the conductivity decreases with decreasing p_{O2}. The difference in conductivity by about half an order of magnitude at 800°C goes along with the fact that y-cut single crystalline and polycrystalline langasite are compared. Consequently, the origin of the decreasing conductivity with decreasing p_{O2} remains to be explained. The further discussion is preferably done using the p_{H2O}-dependence of the conductivity since the corresponding equations for z-cut and y-cut langasite introduced in Section 6.3 show distinct relations (Eq. 6.34 and Eq. 6.30, respectively).

The experimental results presented in Fig. 7.16 indicate a 1/2 dependence of the conductivity along the z-axis at 800°C in the log−log plot. The same applies at 600°C (not shown). Thereby the water incorporation according to Eq. 6.29 is confirmed.

For the actual resonators, the properties along the y-axis are of particular interest. Here, Fig. 7.16 shows a $1/2 - 0.07$ and $1/2 - 0.3$ dependence at

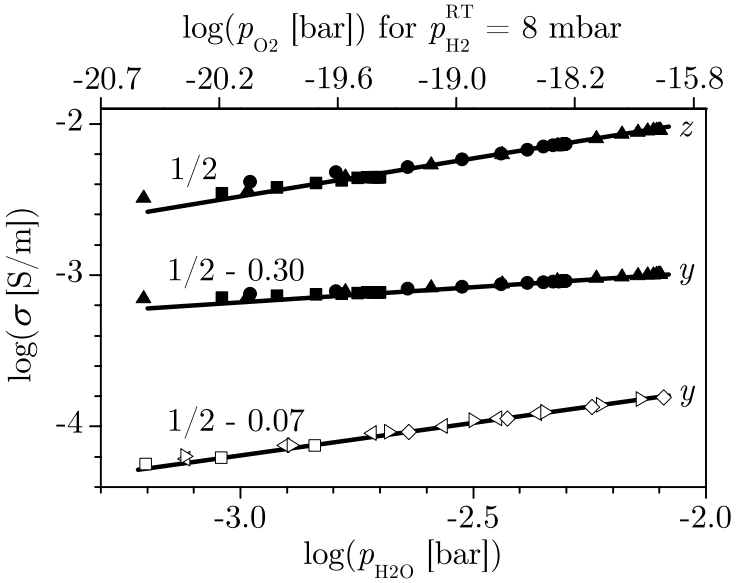

Figure 7.16: Water vapor pressure dependent conductivity of single crystalline langasite at 800 (solid symbols) and 600°C (open symbols). The shape of the symbols corresponds to different levels of hydrogen provided to the reaction chamber ($p_{H2}^{RT} = 2 \ldots 18$ mbar) [80, 114].

600 and 800°C, respectively. The exponent at 600°C is very close to 1/2 thereby confirming Eq. 6.35 which describes the conductivity for fixed oxygen vacancy concentration. At 800°C, the exponent found in the experiment indicates an impact of the oxygen vacancy concentration. It corresponds to the predicted value for proton conduction for $\alpha = 3.6$ (see Eq. 6.36) and confirms the reaction according to Eq. 6.33. Numerous other tested models could not fulfill the experimentally determined p_{H2O}-dependence of σ_Y and the p_{H2}^{RT} independence of the conductivity. The latter becomes obvious by the different symbols in Fig. 7.16 which lie on a line for a given orientation and temperature.

7.5 Gallium Loss

So far, reversible changes in materials properties of langasite are reported. However, unfavorable conditions such as extremely high temperatures and low oxygen partial pressures are suspected to reduce the material or to result in gallium loss. Reduction of langasite leading to irreversible modifications is not observed for the experimental conditions described in the previous sections. In contrast, gallium loss occurs at 900°C at or below $p_{O2} = 10^{-17}$ bar in CO/CO_2 atmospheres. Fig. 7.17 presents SIMS depth profiles for the cations gallium, lanthanum and silicon. Thereby, the acquired data are nor-

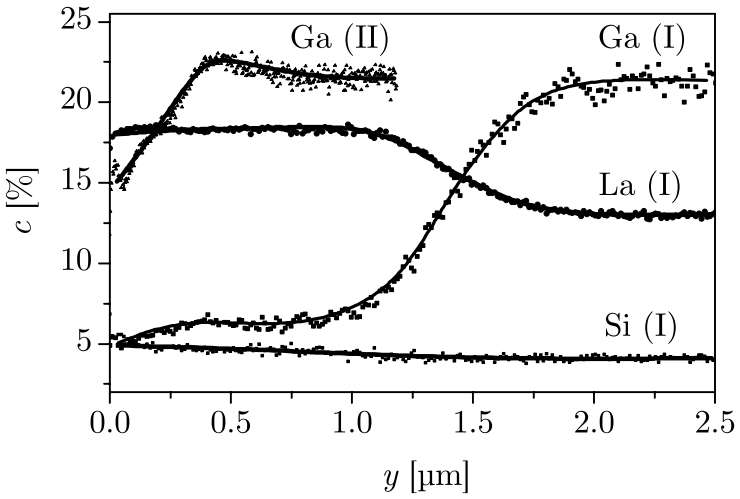

Figure 7.17: Concentration depth profiles for the gallium, lanthanum and silicon after different annealing steps (see text) determined by SIMS.

Table 7.3: Surface concentration after annealing (900°C, $p_{O2} = 10^{-17}$ bar, 24 h) determined by Wavelength Dispersive X-ray spectroscopy (WDX).

concentration c [%]				c_{Ga}/c_{Si}
La	Ga	Si	O	
26.01	9.44	8.94	55.62	1.06

malized to the background concentration of given elements within langasite. The curves denoted by (1) are determined after annealing of single crystalline langasite for 24 h at the conditions mentioned above. A significant decrease in gallium concentration is observed in a surface region of about 1.5 μm. Obviously, the gallium concentration forms a plateau near the surface and does not fall below about 5 % which corresponds to the ratio of gallium to silicon of about unity at the surface (see Tab. 7.3). The observations imply that only sixfold coordinated gallium at the B-sites remains in the sample. The occurrence of the B-site is 4.3 %. In other words, the fourfold coordinated gallium is obviously removed from the lattice. Unfortunately, analysis by X-Ray Diffractometry (XRD) do not deliver conclusive information about the phase at the surface.

A second annealing of the same sample in air (900°C, 24 h) results in an increase in gallium concentration at the surface. In particular, the formerly gallium-depleted area is almost filled by outward diffusion of gallium. The curve denoted by Ga(II) in Fig. 7.17 visualizes the situation. Consequently, the gallium loss at the surface must be largely suppressed at high p_{O2}. The

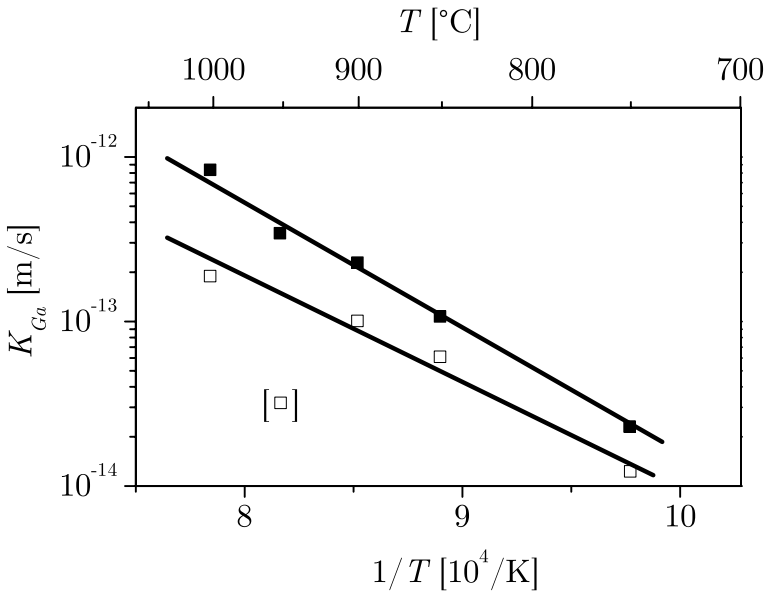

Figure 7.18: Gallium surface exchange coefficients for single crystalline langasite at ambient oxygen partial pressure.

observation goes along with that for Ga_2O_3 reported in [115] where the partial pressure of the volatile gallium suboxide Ga_2O decreases with increasing p_{O2}.

The annealing leads to a decrease of the total gallium content. An uniform decrease is expected for low evaporation rates where the chemical diffusion maintains a nearly constant gallium concentration. However, small changes as estimated for the actual sample cannot be detected due to the limited resolution of the analytical tools. Therefore, the gallium loss is determined using the surface exchange coefficient K_{Ga} which is a secondary result of the diffusion measurements[6]. It must be noted that the diffusion annealing is performed in air. In order to bach up the approach, the surface exchange coefficients are calculated from the difference in the integrals of the gallium concentration profiles determined by SIMS before and after annealing. The difference provides information about the gallium loss for a given annealing time. The surface exchange coefficients determined by both approaches are presented in Fig. 7.18. The difference of the results is fairly small and can be explained by the errors of measurement.

If the surface exchange determines the gallium loss solely, samples held at 750 and 900°C in air lose one monolayer of gallium (6.6×10^{14} atoms/cm^2) within 10 and 1 h, respectively. Therefore, the gallium loss is negligible at 750°C and high p_{O2}. Even at 900°C a surface layer of 1.5 μm would be

[6]Comments about the data evaluation are given in Sections C.5.

depleted within 160 days, only[7]. The situation changes in reducing CO/CO_2 atmospheres as demonstrated above. At 900°C, the gallium loss is increased by a factor of 160.

An essential consequence for the operation of langasite-related compounds under extreme conditions, i.e. high temperatures *and* reducing CO/CO_2 atmospheres, is to use compositions which contain less gallium. A possibly suited gallium-free material is $La_3SbZn_3Ge_2O_{14}$ [116]. Compounds like $La_3Ga_{5-x}Al_xSiO_{14}$ [117], $Ca_3NbGa_3Si_2O_{14}$ [118, 119], $Ca_3TaGa_3Si_2O_{14}$ [120]. $Sr_3TaGa_3Si_2O_{14}$ [121] and $Sr_3NbGa_3Si_2O_{14}$ [122] contain less gallium which is, however, predominantly accommodated at its C-site. Provided that the above mentioned suspicion about the stability of gallium at the B-site is true, the latter materials would not be advantageous. Related investigations are, however, not the subject of this work.

[7]The estimation ignores the chemical diffusion of gallium within langasite.

Chapter 8

Correlation of Electromechanical Properties and Defect Chemistry

In this chapter the electromechanical properties and the defect chemistry of langasite described in in the previous sections is correlated.

8.1 Gas Atmosphere Dependent Frequency

In order to take advantage of the high mass resolution of langasite resonators, atmosphere-independence of the resonance frequency must to be ensured. Therefore, this section focuses on mapping the regimes of gas insensitive operation of langasite resonators and the correlation to langasite's defect chemistry for temperatures up to 1000°C. For the discussion, frequency fluctuations equivalent to noise of ± 4 Hz (see Section 5.5) are taken as criterion to determine the p_{O2} range of stable operation.

8.1.1 Hydrogen Free Atmospheres

First, CO/CO_2 atmospheres are regarded since additional mass loads are expected due to the incorporation oh hydrogen or OH-groups. In the absence of hydrogen, the most relevant feature of the defect model vis-a-vis analysis of resonator operation is the formation of oxygen vacancies $[V_O^{\bullet\bullet}]$ at low p_{O2}.

In case of net acceptor concentration $[A'_C] > [D_C^{\bullet}]$, the concentration of oxygen vacancies is fixed according to Eq. 6.18 by $2[V_O^{\bullet\bullet}] \approx [A'_C]$ at high p_{O2}. Consequently, mass and frequency of langasite resonators are expected to be constant. With decreasing p_{O2}, the reduction reaction controls the concentration of electrons and oxygen vacancies. Based on the neutrality condition $2[V_O^{\bullet\bullet}] = n + [A'_C]$ and the reaction constant according to Eq. 6.26, changes in $[V_O^{\bullet\bullet}]$ are calculated and converted into a fractional density change $(\Delta\rho_R/\rho_R)$ by relating the mass of formed $[V_O^{\bullet\bullet}]$ $(\sim \Delta\rho_R)$ and the mass of the resonator material $(\sim \rho_R)$. The corresponding frequency shift Δf is calculated using Eq. 5.11 and visualized in Fig. 8.1 for $f = 5$ MHz.

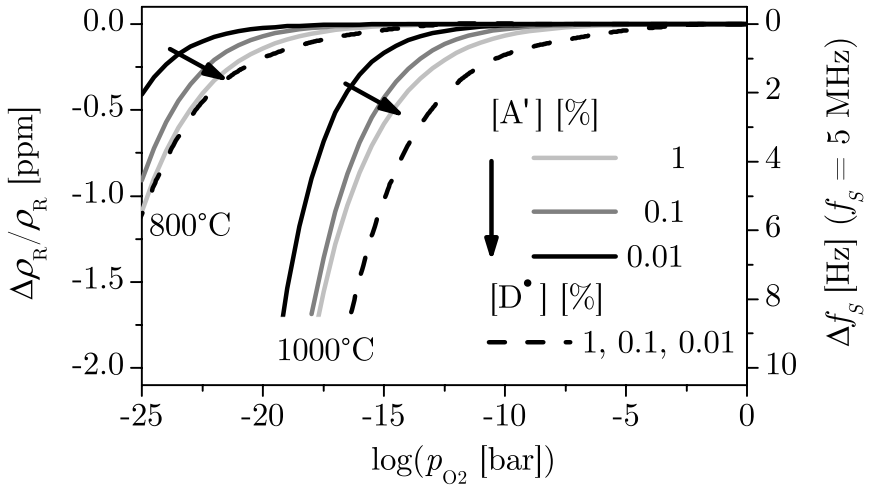

Figure 8.1: Calculated relative mass change and frequency shift of 5 MHz langasite resonators as function of oxygen partial pressure for different acceptor and donor concentrations at 800 and 1000°C.

At 1000°C, the calculated frequency shift exceeds the limit of ± 4 Hz below $p_{O2} = 10^{-17}$ bar, whereas resonators are expected to be stable down to 10^{-24} and 10^{-36} bar at 800 and 600°C, respectively. Fig. 8.1 shows further that the mass change, i.e. the formation of oxygen vacancies, already begins ($\Delta[V_O^{\bullet\bullet}] > 10^{15}$ cm^{-3}) at about 10^{-5} and 10^{-14} bar at 1000 and 800°C, respectively. In contrast, the oxygen vacancy concentration remains unchanged ($\Delta[V_O^{\bullet\bullet}] < 10^{15}$ cm^{-3}) down to 10^{-25} bar at 600°C (not shown in Fig. 8.1). In case of net donor doped langasite, a similar approach can be followed and results in a slightly smaller range of independent operation (dashed lines in Fig. 8.1).

8.1.2 Hydrogen Containing Atmospheres

So far, the impact of hydrogenous species on the conductivity is presented. The reaction according to Eq. 6.33 includes the incorporation of OH-groups. Therefore, frequency shifts related to the resonator density are expected. Under the experimental conditions chosen here, p_{H2O} is fixed ($\Delta \log(p_{H2O}[\text{bar}] < 10^{-3}$) due to the H_2/H_2O buffer above $p_{O2} \approx 10^{-20}$ and 10^{-13} bar at 600 and 800°C, respectively. Therefore, a constant frequency is expected above that p_{O2}'s.

The frequency shift is investigated experimentally by tracing the resonance frequency for $p_{O2} = 10^{-6} \ldots 10^{-25}$ bar at 600°C. Thereby, a 2.1 MHz resonator is used. The observed resonance frequency shift $\Delta f_{2.1} = f_{2.1}(p_{O2}) - f_{2.1}(p^0_{O2})$ is converted into values for 5 MHz resonators Δf by

$$\Delta f(p_{O2}) = \frac{5 \text{ MHz}}{f_{2.1}(p^0_{O2})} \Delta f_{2.1}(p_{O2}) \tag{8.1}$$

thus enabling a direct comparison with the standard resonators. Thereby, p^0_{O2} is chosen to be 10^{-10} bar. The result is shown in the upper part of Fig. 8.2. The resonance frequency remains constant above about $p_{O2} = 10^{-20}$ bar. Below that p_{O2}, the resonance shifts to higher frequencies. At $p_{O2} = 10^{-25}$ bar, $\Delta f \approx 1200$ Hz is found. The change occurs at a p_{O2} significantly higher than $p_{O2} = 10^{-36}$ bar which is the lower limit of constant conductivity in CO/CO_2 atmospheres at 600°C. The fact indicates a minor impact of mechanisms which determine the conductivity under these circumstances. In particular, the concentration of oxygen vacancies $[V_O^{\bullet\bullet}]$ is expected to be virtually constant.

A detailed discussion requires the separation of the materials parameter related contributions to the frequency shift. For that purpose, the resonance spectra are analyzed using the one-dimensional physical model. First, the BvD parameters are extracted and converted into the materials parameters as described in Section 2.3.4. Intermediate results are their relative changes $\Delta[..]/[..]$ as function of p_{O2}. Secondly, Eq. 3.1 is rewritten to determine the frequency shift

$$\Delta f = \frac{\partial f}{\partial [..]} \Delta [..] = f \kappa_{[..]} \frac{\Delta [..]}{[..]}. \tag{8.2}$$

The calculation refers to 5 MHz resonators, i.e. f is chosen to be 5 MHz. The values of the relative derivatives $\kappa_{[..]}$ required for the calculation are taken from Section 5.6 (see e.g. Figs. 5.4, 5.8, 5.9 and 5.10). It must be noted that frequency shifts related to changes in shear modulus and density cannot be separated. The fact becomes obvious from Eq. 5.7. Therefore, the calculation is initially done for $\rho = const.$ The related change in density follows from

$$\rho_R(p_{O2}) = \rho_R(p^0_{O2}) \, \frac{c_{66}(p^0_{O2})}{c_{66}(p_{O2})}. \tag{8.3}$$

The central part of Fig. 8.2 shows the frequency shift caused by the p_{O2} dependence of the materials parameters. The result indicates a predominant impact of c_{66} or ρ_R. Changes caused by the other materials parameters are almost negligible (σ_R and ε_R) or small (e_R). Tab. 8.1 presents the numerical results, since accurate numbers cannot be taken from the plots.

Finally, the question must be discussed whether changes in shear modulus or density determine the frequency shift predominantly. The left and right hand scale in the bottom part of Fig. 8.2 indicate their p_{O2}-dependence, respectively, if the other property is fixed.

According to Eq. 6.33, H_2O is removed from the lattice with decreasing p_{H2O}. The situation corresponds to decreasing p_{O2}'s. Consequently, the calculated decrease in density goes along with the model which is already confirmed by the p_{H2O}-dependence of the conductivity (Fig. 7.16). Further, from $\Delta\rho_R/\rho_R = -5.2 \times 10^{-4}$ follows $\Delta n_{H2O} \approx -10^{20}$ cm^{-3} which requires the existence of about 10^{20} oxygen vacancies per cm^{-3}. The latter sounds about reasonable with respect to

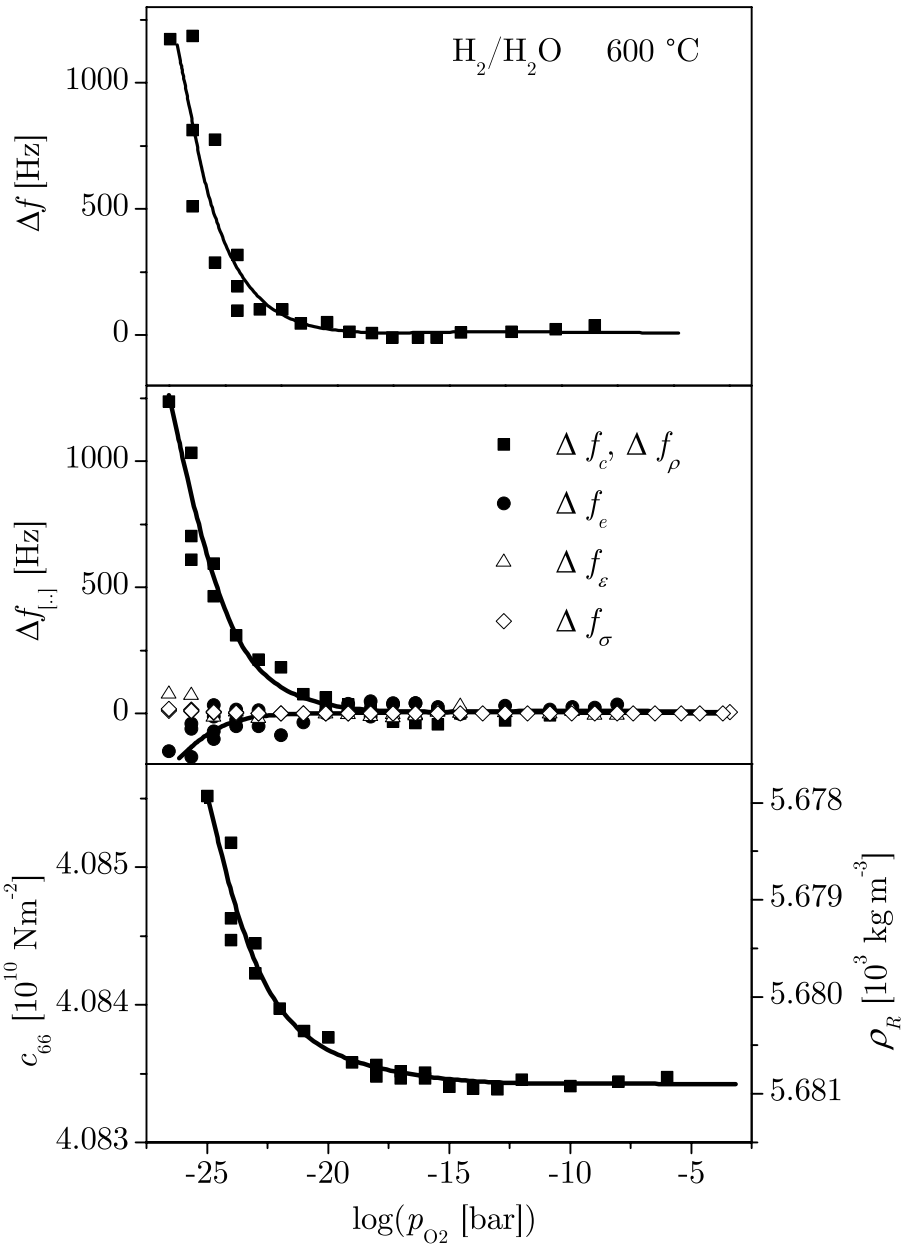

Figure 8.2: Resonance frequency shift (top), materials parameters related frequency shift contributions (center), shear modulus and density (bottom) as function of p_{O2} in hydrogen containing atmospheres at 600°C. Note the inverse scale for ρ_R.

Table 8.1: Relative derivatives of the materials properties, relative changes in materials properties and absolute frequency shift contributions of 5 MHz resonators for changes in p_{O2} from 10^{-10} to 10^{-25} bar in hydrogen containing atmospheres at 600°C.

[..]	c_{66}	(ρ_R)	e_R	ε_R	σ_R
$\kappa_{[..]}$	0.49		6.2×10^{-3}	-3.1×10^{-3}	-8.2×10^{-6}
$\Delta[..]/[..]$	5.2×10^{-4}	(-5.2×10^{-4})	-6.1×10^{-3}	-5.3×10^{-3}	3.8×10^{-2}
Δf [Hz]		1300	-190	82	-2

- The oxygen sites available in langasite (5×10^{22} cm^{-3}) and
- The oxygen vacancy concentration reported in [32] for nominally undoped single crystalline langasite of 10^{19} cm^{-3}.

Based on these insights, the frequency shift can be described by the removal of OH-groups at low p_{O2}. The model is in accordance with conductivity changes which makes it a likely explanation. However, an impact of p_{O2} on the shear modulus can not be excluded entirely.

At 800°C, density changes and related frequency shifts are expected be even stronger. More important, 5 MHz langasite resonators are already operated close to its dielectric relaxation frequency. Consequently, the impact of conductivity changes on the resonance frequency becomes pronounced. With $\kappa_\sigma = -5.5 \times 10^{-4}$ (see Fig. 5.8) and $\Delta\sigma/\sigma = 0.19$ (see Fig. 7.15) follows $\Delta f = -522$ Hz. Such frequency shifts prevent the application of langasite resonators as resonant sensors. Consequently, operation frequencies far off the dielectric relaxation frequency have to be chosen (see also Section 8.2.1).

As discussed in Section 7.4.1, the calculated frequency shift induced by redox related reactions in nominally hydrogen free atmospheres only exceeds the limit of ± 4 Hz at fairly low p_{O2}'s. Water vapor is found to shift the resonance frequency already at higher p_{O2}'s. In the hydrogen containing atmospheres applied here, langasite can be regarded as a stable resonator material above oxygen partial pressures of about 10^{-20} and 10^{-13} bar at 600 and 800°C, respectively.

8.2 Correlation of Loss and Conductivity

8.2.1 Dielectric Relaxation Frequency

Mechanical losses include contributions related to the electrical conductivity. Piezoelectric coupling causes this impact of electrical properties as already

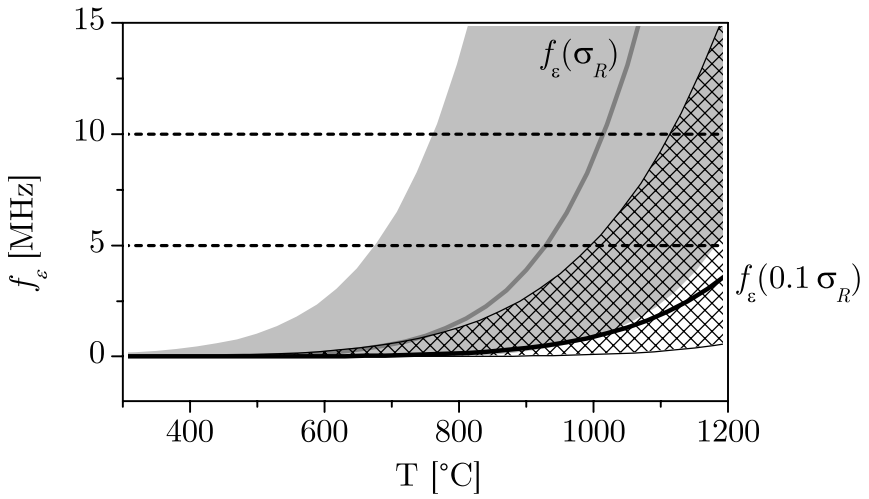

Figure 8.3: Dielectric relaxation frequency f_ε calculated for the conductivity of nominally undoped langasite ($f_\varepsilon(\sigma_R)$) and for a conductivity reduced by a factor of 10 ($f_\varepsilon(0.1\,\sigma_R)$). The corresponding ranges of pronounced conductivity related frequency shifts are indicated by the gray and hatched area, respectively.

mentioned in Section 2.2.2. Its maximum is found at the (angular) dielectric relaxation frequency $\omega_\varepsilon = \sigma_R/\varepsilon_R$. The corresponding frequency $f_\varepsilon = \omega_\varepsilon/(2\pi)$ for nominally undoped langasite is denoted by $f_\varepsilon(\sigma_R)$ in Fig. 8.3[1]. Any operation frequency off that curve is advantageous since the contribution of the conductivity to the mechanical loss would be low.

Further, the resonance frequency is influenced by the conductivity in the vicinity of the dielectric relaxation frequency. Detailed insights provide the relative derivatives κ_σ in Fig. 5.8. A temperature difference ΔT of at least 250 K between maximum (at 925°C) and small impact (below 675°C) of the conductivity can be estimated. Assuming the same temperature difference of $\pm\,250$ K for other operation frequencies than 5 MHz, the unfavorable range of conductivity affected resonance frequencies follows. It corresponds to the gray area in Fig. 8.3. For example, 5, 10 and 15 MHz resonators should be used up to about 675, 760 and 810°C, only. Consequently, the choice of an increased resonance frequency does not increase the recommended temperature limit significantly. One option to overcome the problem is to modify the conductivity as presented in Section 7.4. For a conductivity reduced by a factor of 10 with respect to nominally undoped langasite, the dielectric relaxation frequency denoted by $f_\varepsilon(0.1\,\sigma_R)$ in Fig. 8.3 is calculated. The corresponding range of strongly conductivity affected frequencies is given by the hatched area. The effect of the decreased conductivity is clearly obvious. The recommended operation temperatures are shifted to significantly higher

[1]Frequencies given above 1050°C base on extrapolated values for σ_R and ε_R.

values, namely 1000, 1110 and 1185°C for 5, 10 and 15 MHz resonators, respectively.

Thinking reverse, low frequency resonators can be operated at temperatures above the unfavorable range. For example, 5 MHz resonators are expected to be usable again above about 1200°C. Despite of increased viscosity and bulk conductivity related losses, the approach might be reasonable since

- The viscosity related loss plays a minor role above about 650°C (see Fig. 5.5) and
- The increase of G_S ($\sim \sigma_R$) might lead to tolerable restrictions of the accuracy in frequency determination (see Fig. 2.8).

The discussion clearly underlines the importance to tailor the conductivity of langasite depending on the anticipated operation temperature and frequency.

8.2.2 Nominally Undoped Langasite

In this section, the activation energies of loss and conductivity are compared in order to decide if both properties are potentially determined by the same microscopic mechanism.

Initially, temperature ranges appropriate for that comparison must be identified. The experimental results (Fig. 5.5) in concert with the parameter study (Figs. 3.11, 3.12 and 3.19) predict distinct temperature ranges where different phenomena dominate the loss of 5 MHz langasite resonators:

(1) Room temperature to 350°C.

A local loss maximum is observed at about 250°C (see Fig. 5.5). The extend of the peak depends on the thermal history of the sample as also reported in [79, 123]. Further, the observation is in general agreement with results presented in [81]. An activation energy of 0.34 eV for point-defect relaxation and an Arrhenius like background behavior with an activation energy of 0.1 eV (see Fig. 8.6) are reported at temperatures up to about 350°C. This loss peak is of minor interest for this work since other mechanisms overwhelm its effect at high temperatures.

(2) 350 to 650°C.

The loss is governed by the viscosity[2]. However, the previously described loss peak influences the slope of the viscosity in this temperature range. The situation is shown schematically in Fig. 8.4. At some elevated temperature, the curve for η appears to be nearly linear in the Arrhenius plot[3]. With decreasing temperature, the curve becomes

[2]Related loss contributions are R_η and $Q_{c,\eta}$ in Figs. 3.10 and 3.19, respectively.
[3]The subscript of η_R is skipped in this section.

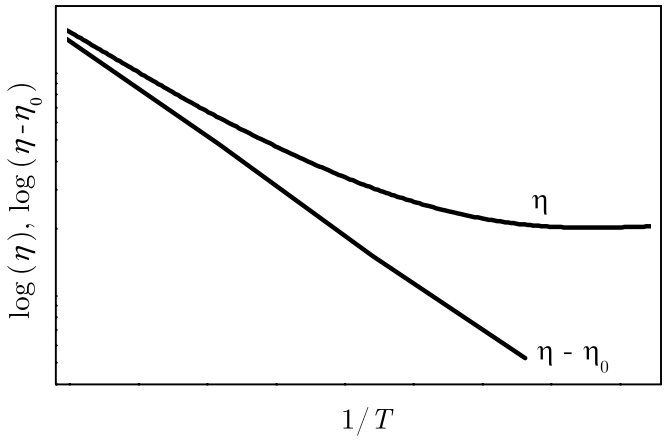

Figure 8.4: Scheme of the viscosity with (η) and without ($\eta - \eta_0$) its temperature independent contribution η_0.

flatter. A temperature independent contribution η_0 can be subtracted which results in an Arrhenius like behavior of $\eta - \eta_0$ as shown in Fig. 8.4. This contribution is interpreted as sum of losses applying in range (1) and losses caused by imperfect resonator design, manufacturing, electrodes and mounting. An analogous subtraction of the background loss is chosen in [81] and [83] for langasite and quartz, respectively[4].

The modified viscosity $\eta - \eta_0$ is not impacted by either background contributions, conductivity related mechanical loss[5] or bulk conductivity and enables to extract the activation energy of the dominant mechanism as done at the end of this section.

(3) 650 to 1050°C.

The loss is governed by the viscosity, conductivity related mechanical loss and bulk conductivity. Thus, a single activation energy cannot be extracted.

In Summary, the intended comparison of the activation energies can be done only in range (2) where the loss is determined solely by the viscosity. Fig. 8.5 presents $\eta - \eta_0$ as function of the inverse temperature and the related activation energy. The value of 0.83 eV corresponds very well to that of the conductivity (see Tab. 8.2). Consequently, it is highly likely that the predominant conductivity mechanism also controls mechanical loss in temperature range (2). Based on the apparent correlation of conductivity and viscosity, lowering the electrical conductivity should result in lowering of damping and is, therefore, desirable.

[4]In both publications, the inverse resonator quality factor is used to describe the loss.
[5]Piezoelectric coupling in the vicinity of the dielectric relaxation frequency.

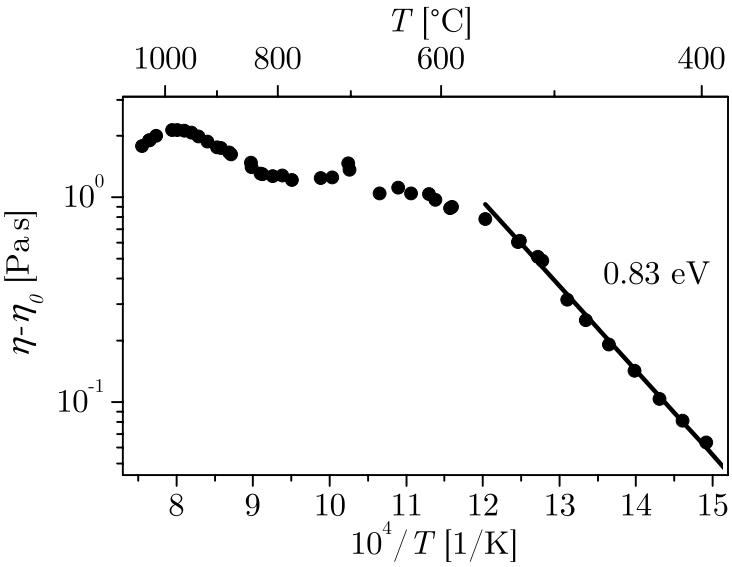

Figure 8.5: Viscosity of undoped langasite without its temperature independent contribution.

The latter conclusion applies in range (3) without any restrictions since conductivity related losses dominate (see Fig. 5.5).

8.2.3 Strontium and Niobium Doped Langasite

The effect of dopants on the loss is discussed separately for temperature ranges (2) and (3).

Temperature range (2) from 350 to 650°C

In order to provide comprehensive information, the loss of nominally undoped, strontium and niobium doped langasite is presented in form of the uncorrected viscosity in Fig. 8.6. The doped crystals show significantly lower background losses than the undoped material. This fact concerns temperature range (1) and is, therefore, not subject of the further discussion.

Fig. 8.7 presents the corrected viscosities. Niobium doped langasite exhibits a decreased viscosity and, therefore, a decreased loss with respect to undoped langasite. Contrary, strontium doped langasite does not show any change in viscosity. The observation must be discussed in concert with the conductivity of the differently doped crystals. They exhibit about the same change with respect to undoped langasite as seen in Fig. 7.14. Consequently, decreased conductivities go along with decreased losses in case of donor doping, only. In other words, the suppression of oxygen vacancies by donors decreases the loss. The observation confirms the expected stronger interaction

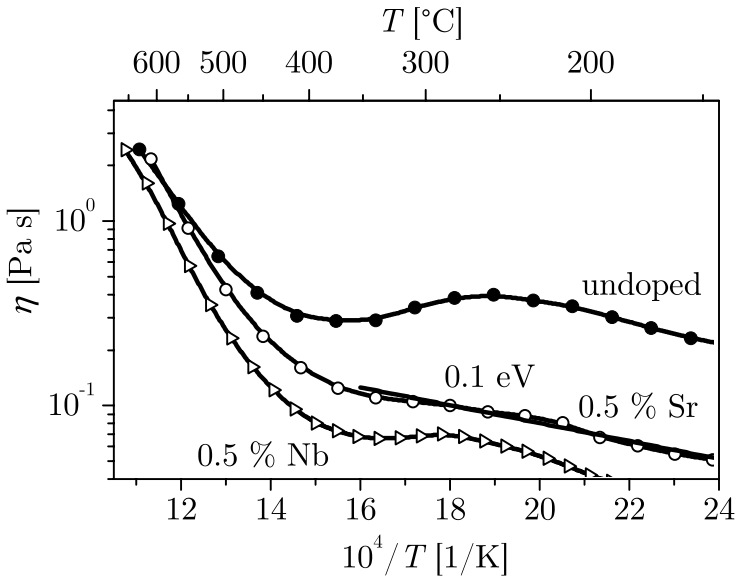

Figure 8.6: Viscosity of nominally undoped, strontium and niobium doped langasite.

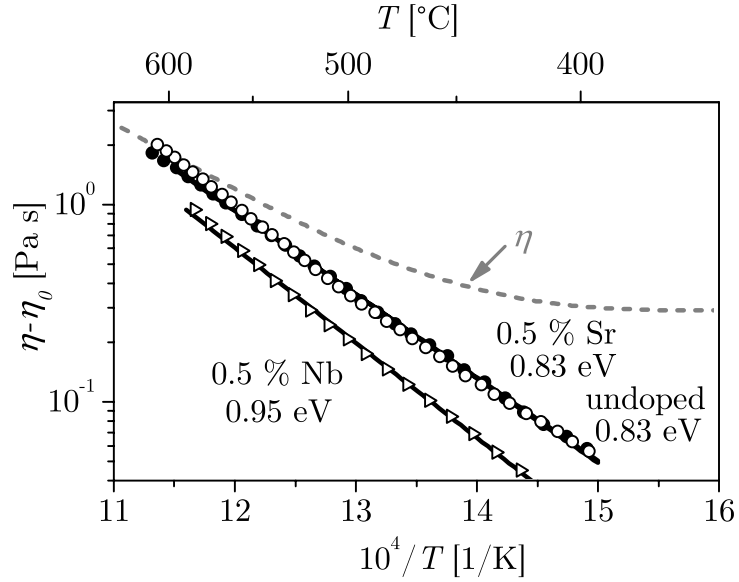

Figure 8.7: Viscosity of nominally undoped, strontium and niobium doped langasite without its temperature independent contribution.

Table 8.2: Activation energy of viscosity and conductivity in langasite.

langasite	property	E_A [eV]	temperature range [°C]
sc	σ_B	0.82	400 ... 700
	$\eta - \eta_0$	0.83	400 ... 600
sc (0.5 % Nb)	σ_B	0.91	400 ... 550
	$\eta - \eta_0$	0.95	420 ... 580
sc (0.5 % Sr)	$\sigma_B T$	0.98	400 ... 550
	$\eta - \eta_0$	0.83	400 ... 600

of moving oxygen ions and lattice in comparison to that of electrons and lattice. Most remarkably, minimized losses do not require generally minimized total conductivity. In particular, the ionic contribution must be lowered in temperature range (2).

Further, similar activation energies of σ_B and $\eta - \eta_0$ are observed for undoped and niobium doped langasite, respectively. The statement becomes obvious from the numerical values summarized in Tab. 8.2. The fact indicates the control of both processes by the same mechanism. Contrary, the activation energies of $\sigma_B T$ and $\eta - \eta_0$ differ in case of strontium doped langasite thereby indicating different mechanisms.

Temperature range (3) from 650 to 1050°C

In temperature range (3), the loss is described by the (inverse) Q-factor since the sum of different loss phenomena have to be regarded.

Fig. 8.8 compares the loss of undoped and doped langasite. Strontium doping decreases the loss slightly whereas niobium doping causes strong lowering of loss. The observed pattern in magnitude corresponds to that of the conductivity in temperature range (3) as presented in Fig. 7.14. Consequently, lowering the conductivity results generally in decreased losses.

The latter statement corresponds to the dominance of conductivity related losses in the actual temperature range for undoped langasite. The validity of the statement for doped langasite can be seen from the comparison of Q^{-1} and η as presented in Fig. 8.9[6]. The results indicate the dominance of conductivity related loss above about 650 and 700°C for strontium and niobium doped langasite, respectively.

[6]The alignment of the left and right hand axis is done for data points in temperature range (2) where the viscosity dominates the loss solely (see also Fig. 5.5).

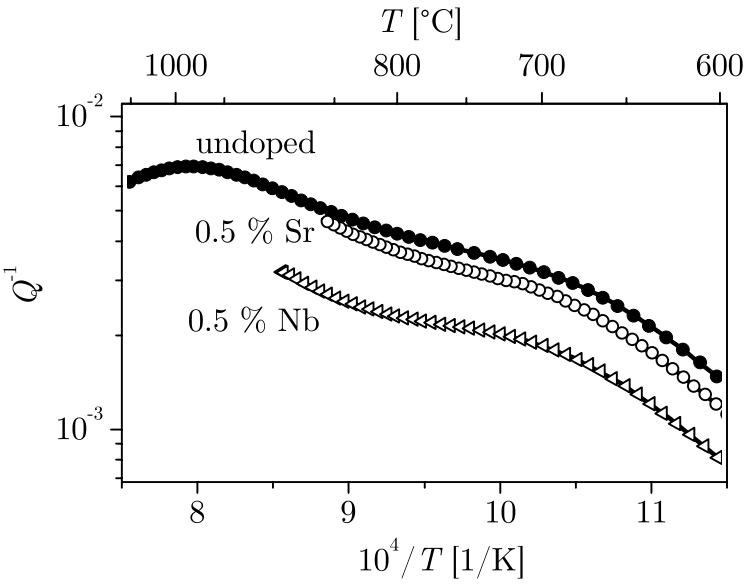

Figure 8.8: Resonator quality factor of undoped, strontium and niobium doped langasite.

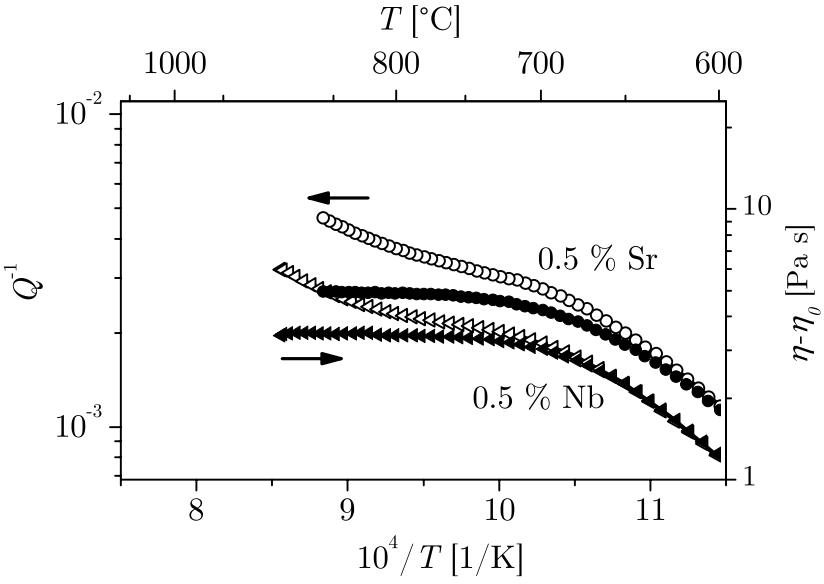

Figure 8.9: Resonator quality factor (Q, open symbols) and viscosity ($\eta - \eta_0$, solid symbols) of strontium and niobium doped langasite.

Part III

Application Relevant Studies and Outlook

Chapter 9

Application Relevant Studies

Application relevant studies are performed in parallel to the investigation of the electromechanical properties and defect chemistry presented so far. The following sections summarize this results thereby underlining the application capabilities of high-temperature stable piezoelectric materials. The corresponding details are described in the references given below.

9.1 Gas Sensor Applications

The section demonstrates the gas sensing capabilities of sensor film coated langasite resonator devices at 600°C. It is already shown that the electromechanical properties of undoped langasite are suited for the operation of 5 MHz resonators at this temperature.

Stoichiometry changes induced in metal oxide films and related surface adsorption phenomena can be used for gas sensing at elevated temperatures. Variations in the composition of the surrounding gas atmosphere are expected to influence simultaneously the mechanical and electrical properties of the sensor film, in particular its mass, and its electrical conductivity (see Appendix B) thereby providing often orthogonal information about the gas. In order to increase the gas selectivity, the simultaneous measurement of changes in mechanical and electrical sensor film properties is desirable.

The effect of both properties is detected using $TiO_{2-\delta}$ coated langasite resonators with specially adapted electrode geometries. Platinum electrodes with different diameters are deposited on the opposite faces of the resonators as schematically shown in the upper part of Fig. 9.1. Thereby, resonator (M) is operated in the conventional microbalance mode. Changes in $TiO_{2-\delta}$ conductivity do not influence the resonance behavior since the underlying platinum electrode is larger than the platinum film. Contrary, resonator (E) reflects changes in the $TiO_{2-\delta}$ conductivity due to its influence on the effective electrode size. In this case, the $TiO_{2-\delta}$ film exceeds the underlying platinum electrode. The electrode layout and the related effects are explained in detail in [45, 124].

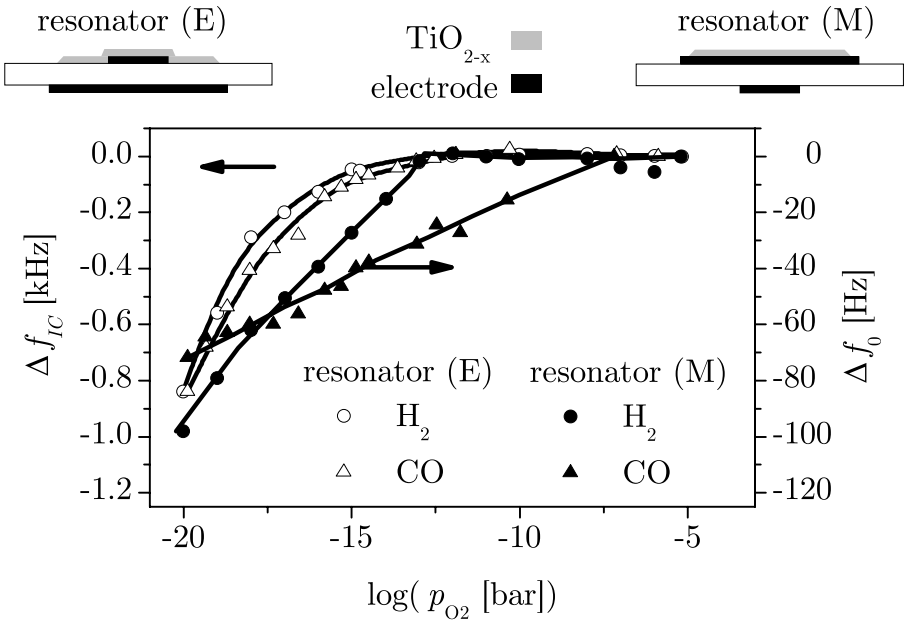

Figure 9.1: Resonance frequency of $TiO_{2-\delta}$ coated langasite resonators with different electrode design as function of oxygen partial pressure at 600°C in different H_2/H_2O and CO/CO_2 containing atmospheres.

The existence of a combined conductivity and mass related sensor response motivates the attempt to distinguish between CO and H_2 containing gases. Fig. 9.1 presents temperature-compensated frequency shifts Δf_{IC} obtained as a function of the oxygen partial pressure at about 600°C for gas mixtures of H_2/H_2O and CO/CO_2 with Ar as buffer gas. While the response of resonator (E) appears to be influenced only by the p_{O2}, resonator (M) reflects the type of gas. In practice, where the p_{O2} is unknown, the signal of resonator (E) has to be used to acquire this information. Most important, the different slope and magnitude of the frequency shift of both resonators enables the detection of CO in hydrogen containing atmospheres in the p_{O2} range from 10^{-13} to 10^{-20} bar. Further investigations include other sensor film materials such as CeO_2 which enable gas detection at higher p_{O2}'s [39, 125].

9.2 Micro-Electromechanical Structures

The availability of large size langasite wafers enables micromachining of this high-temperature stable piezoelectric material. Special emphasizes is taken on the development of monolithic structures to overcome problems originating from thermal stress. The concept includes the local doping of langasite by niobium, strontium and praseodymium. The doping is expected to result

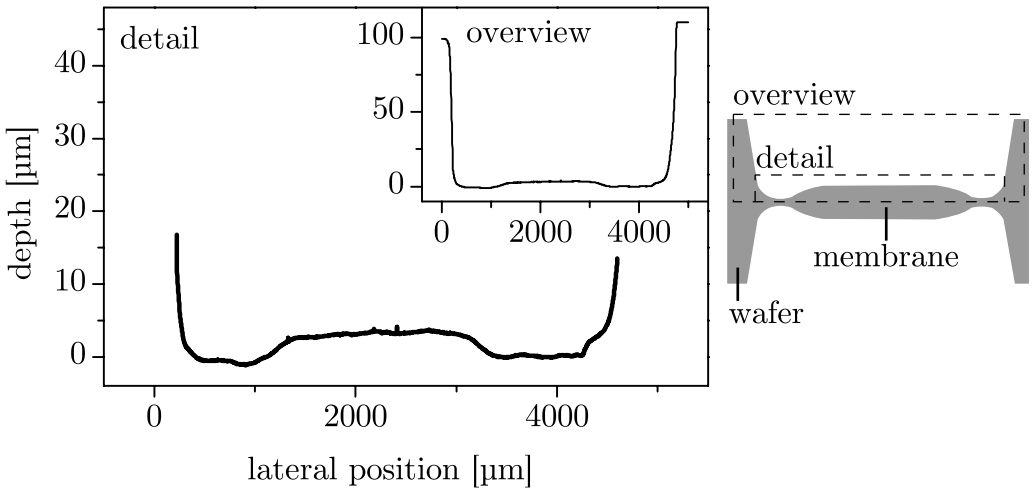

Figure 9.2: Depth profiles of a biconvex langasite membrane prepared by wet chemical etching (left) and schematic cross section of the membrane indicating the areas of the depth profiles (right).

in locally increased conductivities to form electrodes. Another anticipated effect is the modification of the rate of wet chemical etching and, thereby, the option to etch the material locally.

To demonstrate the etching process and the potential of langasite as substrate for bulk micro-machining, micro-cantilever beams [126, 127] and membranes [38, 128] are designed and structured. As an example, the depth profile of a biconvex membrane is shown in Fig. 9.2. Such membranes exhibit higher Q-factors than the planar membrane type.

Further, the temperature dependent resonance frequency and Q-factor of an about 23 μm thick langasite membrane are given in Fig. 9.3. Due to the high resonance frequency, such membranes are operated far above their dielectric relaxation frequency (see Fig. 8.3) leading to relatively low electrical losses [128].

9.3 High-temperature Stable Electrodes

Thin film platinum electrodes used in this work are prepared by PLD. They impact the resonance behavior very little due to their thickness of typically 200 nm, only. However, evaporation of volatile platinum suboxides and agglomeration of platinum [129] are a major concerns if thin films are used. As a consequence, the operation temperature is limited to about 1000°C. Mesh-printed platinum electrodes can be used at higher temperatures. Such films are significantly thicker which results in less pronounced relative changes of their properties for a given period of time and temperature. However, the

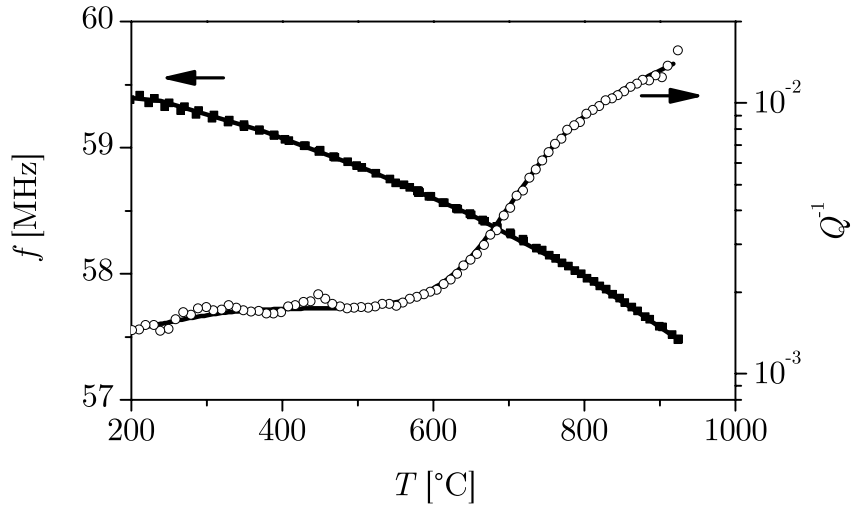

Figure 9.3: Temperature dependent resonance frequency and resonator quality factor of an about 23 μm thick langasite membrane.

fundamental problem of platinum loss is not solved.

An alternative approach is the application of ceramic electrodes. Low conductivities of such materials occurring at low temperatures are not relevant as long as the operation temperature is high. In order to demonstrate this option, lanthanum strontium manganate ($(La_{0.8}Sr_{0.2})_{0.98}MnO_{2-d}$) electrodes are applied. Fig. 9.4 shows the resulting temperature dependence of resonance frequency and Q-factor up to 1350°C. The resonance frequency is not affected by the alternative electrode material as it becomes obvious by the comparison with the gray dashed line which is taken from measurements using thin film platinum electrodes (T = room temperature...1000°C). In contrast, the temperature dependence of the Q-factor shows distinct differences with respect to resonators wearing metal electrodes. High losses are observed at low temperatures since the LSM electrodes exhibit low conduction. With increasing temperature the electrodes become highly conductive which results in increased Q-factors. Most remarkably, a Q-factor of 50 is observed even at 1350°C.

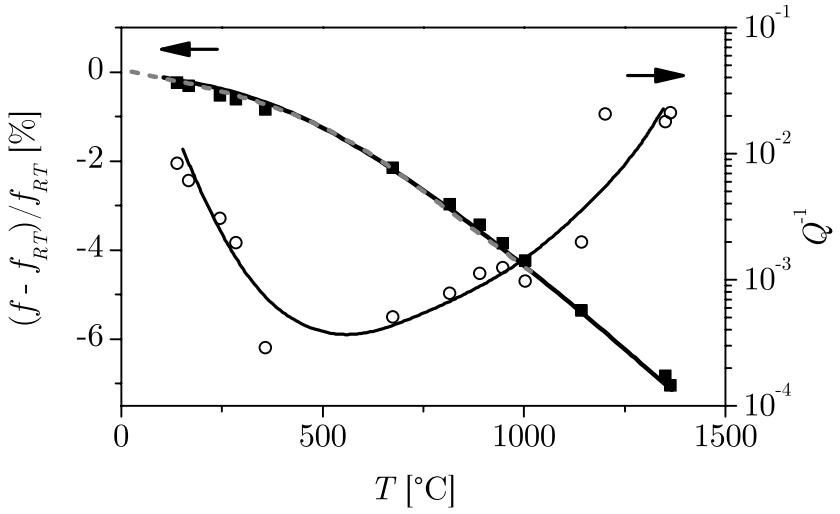

Figure 9.4: Temperature dependent resonance frequency and resonator quality factor of a 5 MHz langasite resonator wearing ceramic electrodes.

Chapter 10

Outlook

The subsequently discussed issues are not investigated in the frame of this study. Further ongoing work is presented in Chapter 9.

10.1 Models

The modeling of the BAW resonators bases on a one-dimensional model. Consequently, out-of-plane deformation of the devices and its effect on the resonance behavior cannot be accounted. The fact prevents accurate data evaluation in case of the presence of mechanical stress caused by e.g.

- Differences in CTE of resonator and thick film electrodes or sensor materials,
- Volume changes of the sensor material due to environmental dependent stoichiometry or phase transformation,
- Different pressure on both sides of the resonator or
- Mechanical stress due to the resonator mounting.

In particular, asymmetric electrodes or sensor films are expected to cause relevant stress.

The applicability of models and approximations known for quartz resonators presented for example in [130–132] must be proven. Detailed understanding of stress related phenomena broadens the application range of high-temperature resonators. The availability of stress compensated crystal cuts is preferred to investigate, for example, mass changes of thick sensor films. Contrary, crystal cuts showing large impact of mechanical stress are suited for in-situ monitoring of stress related to film deposition or temperature changes.

10.2 Materials

The investigations presented so far are focussed on langasite since the material is regarded as model compound for the related family of crystals. Consequently, the acquired knowledge can be applied to determine the operation limits of other promising compounds or to improve their applicability by e.g. appropriate doping. Candidate materials are compounds containing no or less gallium as already mentioned in Section 7.5.

$GaPO_4$ is part of this study since it shows extremely low losses. However, even if its operation temperature limit of about 900°C does not restrict the applicability, difficulties to growth large and high-quality crystals prevent its large scale application. Provided that maximum operation temperatures of about 900°C match the requirements, the use of $LiNbO_3$ might be an alternative option. Improved crystal growth technologies such as the Vapor Transport Equilibration (VTE) enable the preparation of stoichiometric $LiNbO_3$. The newly available material contains less crystal defects and does not tend to decompose. Preliminary tests indicated operation temperature limits which are much above that of conventional non-stoichiometric material. Detailed investigations are required.

Polycrystalline piezoelectric materials are not regarded as option for high temperature application. The Curie temperature of most advanced materials such as lead metaniobate ($PbNb_2O_6$) is in the order of 570°C which is far below the anticipated operation limits. Further, application of such lead containing materials is generally under question due to environmental concerns.

Summary

Langasite and gallium phosphate crystals are shown to exhibit bulk acoustic waves up to at least 1400 and 900°C, respectively. Therefore, a wide range of high-temperature applications becomes feasible provided that the resonators can be operated environmentally independent. Most critical issues are stoichiometry changes of the resonator materials and high losses.

First, a one-dimensional physical model is developed to describe the electromechanical behavior of thickness shear mode resonators at elevated temperatures. Finite lateral dimensions of such devices require the introduction of areas which reflect the effective amplitude of the mechanical vibration and the effective electrode area. Most remarkably, both areas differ by a factor of about two. The accurate description of high-temperature resonators must consider this fact. Further, the physical model includes losses in form of imaginary parts of the materials constants. The analysis of the resonance spectra showed that the loss of the resonators can be described satisfactorily by the mechanical and electric contributions expressed as effective viscosity and finite bulk conductivity, respectively. Contrary, losses related to the imaginary part of the piezoelectric constant does not have to be included.

An equivalent electrical circuit for high-temperature resonator devices is derived based on the one-dimensional physical model. The approach makes the model handy for routine data evaluation. Further, low- and high-temperature approximations are introduced. Thereby, the structure of the equivalent circuit corresponds to the Butterworth-van Dyke equivalent circuit extended by a finite bulk resistance. Assignments of the lumped elements to the physical properties are given. In case of langasite resonators the low-temperature approximation is valid up to about 900°C.

A parameter study is performed to evaluate the impact of the materials properties on the resonance behavior. Using the physical model and experimentally determined materials parameters, the impact of the latter on the key resonator properties, namely the resonance frequency and the quality factor, is given quantitatively. These expressions can be regarded as generalized Sauerbrey equations. Properties most relevant for environmentally dependent frequency shifts and losses are identified to be shear modulus, density, electrical conductivity and effective viscosity.

The contribution of viscosity and conductivity to the total loss is analyzed using idealized data. Their magnitude corresponds to some extend to the data of langasite. However, single activation energies are assumed to

exclude e.g. local loss peaks. The approach is chosen to study the fundamental behavior of resonator devices at elevated temperatures. The essential result is the appearance of three distinct temperature ranges dominated by mechanical losses related to the viscosity, mechanical losses related to the electrical conductivity and electric losses. Most remarkably, the mechanical loss is significantly impacted by the electrical conductivity due to the piezoelectric coupling. That loss contribution shows a maximum which is found at the dielectric relaxation frequency. Minimization of the conductivity or the resonator operation off that frequency is recommended. The effect of the piezoelectric coupling on the loss is negligible for gallium phosphate since it shows an extremely low electrical conductivity. Measured data of langasite indicate dominant viscoelastic losses up to about 650°C while the dielectric loss dominates about that temperature. The loss peak related to the piezoelectric coupling is observed at 925°C for 5 MHz resonators.

The materials data of the piezoelectric crystals and the resonance characteristics of 5 MHz resonators are presented up to 1050 and 900°C for langasite and gallium phosphate, respectively. The mass sensitivity at elevated temperatures is about as high as that of quartz at room temperature. Temperature related frequency fluctuations can be compensated almost entirely by using higher vibration modes. Within its operation temperature range, gallium phosphate shows significantly lower losses than langasite. Even at 1050°C the resonator quality factor of langasite resonators equals about 100 which is is sufficiently large to determine the resonance frequency using active methods such as network analysis.

In order to explore the operation limits and options to improve the resonance properties of langasite its defect chemistry is investigated. Thereby, a defect model developed using polycrystalline langasite is found to be valid for single crystals. Most remarkably, the electrical conductivity of nominally undoped langasite prepared by the Czochralski technique is dominated by n-type electronic carriers below 700°C and turns in predominant oxygen ion conduction above that temperature. The activation energy of the oxygen diffusion is found to be higher than that of the electronic conduction and almost equal to the activation energy of the total conductivity above 700°C. The former statements apply for high oxygen partial pressure. With decreasing oxygen partial pressure n-type electronic conduction becomes always dominant, e.g. below below 10^{-24} bar at 800°C. Mobile anions do not impact the electrical conductivity as verified by measurements of the gallium diffusion.

Moving oxygen ions are always present even if they do not govern the electrical conductivity. Therefore, their presumably strong effect on damping is expected also at low temperatures. Consequently, donor doping appears to

be always appropriate to decrease the loss. Donors are expected to suppress the oxygen vacancy concentration and, thereby, the oxygen movement. The prediction is proven by niobium doping and found to be valid. The loss could be decreased in the entire temperature range of investigation.

Acceptor doping results in decreased electrical conductivity provided that perfectly compensated crystals are created. However, its effect on the loss depends on the predominant charge carrier type and, therefore, on the actual temperature. Below about 700°C, a decreased conductivity does not go along with lower losses. Above that temperature the loss is determined by the electrical conductivity which results in slightly lower losses with decreased conductivity. Since the effect is weak and limited to the high-temperature range, donor doping is preferred to decrease the loss.

In the absence of hydrogen, the formation of oxygen vacancies limits the stable operation of langasite at fairly low oxygen partial pressures. The material shows increased *n*-type electronic conduction with decreasing oxygen partial pressure. Above e.g. 10^{-17}, 10^{-24} and 10^{-36} bar at 1000, 800 and 600 °C, respectively, the oxygen vacancy concentration remains almost constant and a stable resonance frequency is expected. In contrast, hydrogenous atmospheres cause a different behavior. The conductivity decreases with decreasing oxygen partial pressure. The behavior is preferably discussed using the water vapor pressure dependence of the conductivity. The incorporation of OH-groups in oxygen vacancies results in a distinct correlation which is experimentally confirmed. Essentially, at low oxygen partial pressures the OH-groups are removed from the lattice which lowers the concentration of mobile hydrogen containing carriers and, thereby, the conductivity. The related frequency shift starts at higher oxygen partial pressures than in nominally hydrogen free atmospheres, i.e. below about 10^{-13} and 10^{-20} bar at 800 and 600°C, respectively. The frequency shift of langasite resonators is in accordance with conductivity changes which supports the model.

Application examples are summarized to demonstrate the capabilities of high-temperature stable piezoelectric materials. For example, the simultaneous determination of mechanical and electrical properties of thin sensor films by resonant sensors enables detection of CO in hydrogen containing atmospheres.

In recapitulating, a comprehensive view on high-temperature piezoelectric materials with special emphasis on the correlation of electromechanical properties and defect chemistry is given.

Appendix A

Materials Data

A.1 Piezoelectric Materials

Tab. A.1 lists room temperature data of the piezoelectric materials from different publications. The materials constants of interest for the y-cut resonators are $\rho_R = \rho$, $\varepsilon_R = \varepsilon_{22} = \varepsilon_{11}$, $e_R = e_{26} = -e_{11}$ and c_{66}.

In order to provide independent materials data of the actual langasite crystals pulse-echo measurements are performed [77]. The key properties correspond to the literature data as it can be seen from the results given in parenthesis in Tab. A.1.

The thermal expansion of langasite is taken from [78] and extrapolated linearly as seen in Fig. A.1. Based on this data the temperature dependence of thickness and density is calculated. The values of $GaPO_4$ and quartz can be found in [40, 76] and [133], respectively.

A.2 Platinum Electrodes

Tab. A.2 presents the properties of the platinum electrodes at room temperature. Thereby, the density ρ_F and the clastic constant $c_F = c_{66}$ ($= c_{44}$, cubic crystal) are taken from [74].

A.3 Standard Resonators

This subsection summarizes materials properties and dimensions of the 5 MHz standard resonators used for the parameter study in Chapter 3. At room temperature, these calculations base on materials data from above. The viscosities and dimensions are given in Tab. A.3.

Some examples refer to 1 and 25 MHz resonators. In this cases, the thickness is modified, only. The capacitance and resistance of the sample holder chosen here are $C_L = 10$ pF and $R_L = 1\Omega$. respectively.

Table A.1: Room temperature materials constants of langasite, gallium phosphate and quartz.

		langasite [75]		$GaPO_4$ [40, 76]	quartz [48, 74]
ρ	$[10^3$ kg m$^{-3}]$	5.748		3.57	2.648
$\varepsilon_{11}/\varepsilon_0$		18.99		6.1	4.428
$\varepsilon_{33}/\varepsilon_0$		50.44		6.6	4.634
e_{11}	[C m^{-2}]	-0.436		0.209^a	0.171
e_{14}		0.092		0.107^a	0.041
c_{11}		18.924		6.658	8.674
c_{12}		10.489	(10.33)	2.181	0.699
c_{13}		9.782	(9.71)	2.487	1.191
c_{14}	$[10^{10}$ Nm$^{-2}]$	1.448	(1.50)	0.391	1.791
c_{33}		26.330	(26.19)	10.213	10.720
c_{44}		5.343	(5.33)	3.766	5.794
c_{66}		4.232	(4.28)	2.238	3.988

[a]Calculated from $e_{ip} = d_{iq}c_{qp}$ [48].

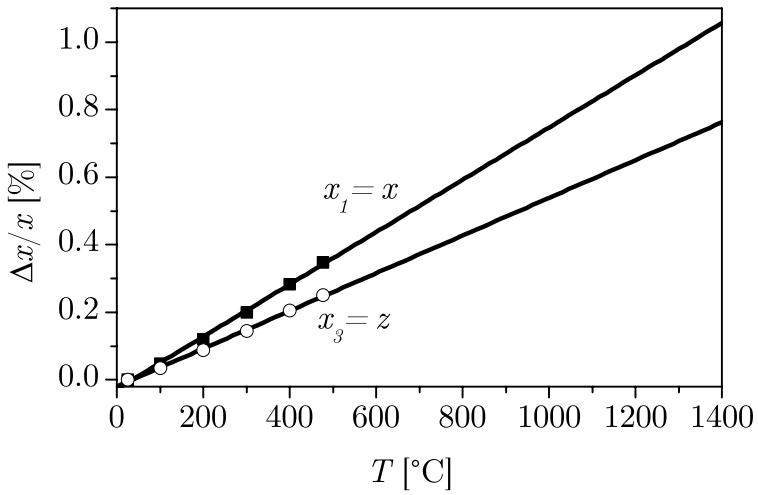

Figure A.1: Thermal expansion of langasite along the x- and z-direction according to [78] (symbols) and linear extrapolation up to 1400°C (solid lines).

Table A.2: Properties of the platinum electrodes.

d_F	[nm]	$\approx 200^a$
ρ_F	$[10^3\ \mathrm{kgm^{-3}}]$	21.5
c_F	$[10^{10}\ \mathrm{Nm^{-2}}]$	7.6
η_F		0

[a] Average electrode thickness. The value for the actual resonator is used.

Table A.3: Viscosities and dimensions of 5 MHz standard resonators at room temperature.

material	η_R [Pa s]	d_R [μm]	A_R [mm^2]	A_E [mm^2]
langasite	0.026	272.2	10	20
$GaPO_4$	0.038	248.6	10	20
quartz	0.046	385.2	10	20

The high-temperature data of the piezoelectric material used for the parameter study correspond to some extend to those of langasite. The extrapolation up to 1400°C is done

- Linearly for the thickness and density according to the data presented in Fig. A.1,
- Linearly for the dielectric constant and the piezoelectric coefficient as given for 500, 1000 and 1400°C in Tab. A.4,
- Parabolically for the shear modulus as given in Tab. A.4,
- Exponentially for the conductivity and viscosity according to $\sigma_R T = \sigma_0 e^{-E_\sigma/k_B T}$ and $\eta_R = \eta_0 e^{-E_\eta/k_B T}$ as given in Figs. A.2 and A.3, respectively.

A.4 $TiO_{2-\delta}$ Sensor Films

The density ρ_F and the shear modulus $c_F = c_{66}$ of the sensor film chosen for the parameter study correspond to those of titania (rutile) according to [74]. These values, the thickness and the effective viscosity are given in Tab. A.5.

Table A.4: Material constants used for the parameter study at elevated temperatures.

temperature [°C]	ε_R [10^{-10}]	η_R [Pa s]	e_R [Cm^{-2}]	c_{66} [10^{10} Nm^{-2}]
500	2.02	1.14	0.52	4.11
1000	2.33	2.57	0.61	3.87
1400	2.54	3.47	0.67	3.58

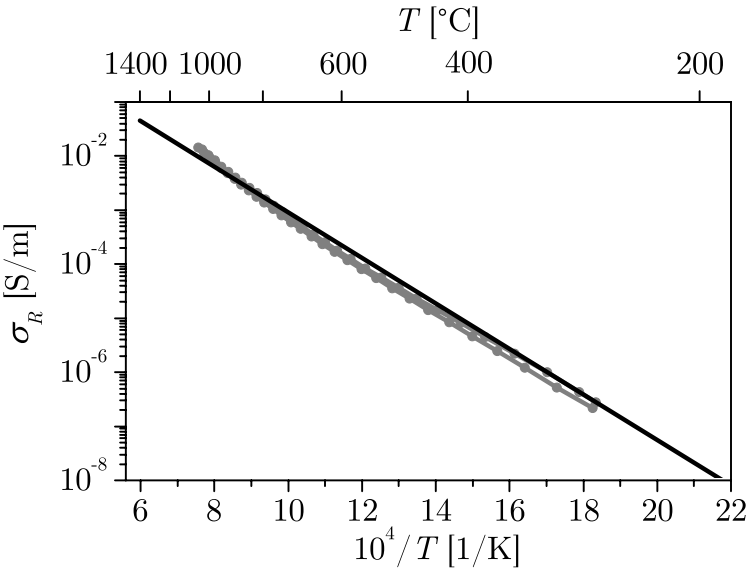

Figure A.2: Conductivity used for the parameter study at elevated temperatures (black line). For reference, the data of langasite are given (gray line and symbols).

Table A.5: Properties of the sensor film used for the parameter study.

ρ_F	[10^3 kgm^{-3}]	4.26
c_F	[10^{10} Nm^{-2}]	19.5
η_F	[Pa s]	0.05
d_F	[nm]	1000

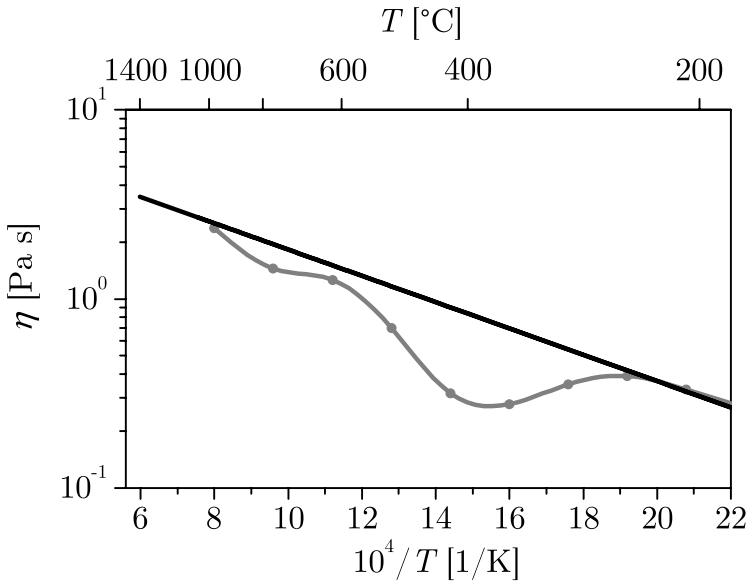

Figure A.3: Viscosity used for the parameter study at elevated temperatures (black line). For reference, the data of langasite are given (gray line and symbols).

Appendix B

Effective Electrode Area

B.1 Platinum Electrodes

The effective electrode area A_E is slightly larger than the geometrical electrode area. The fact is caused by fringing fields as indicated in Fig. B.1. Numerical values for the ratio of the effective and geometrical electrode area γ are determined by finite element methods using the software package *FEMLAB* (FEMLAB GmbH, Göttingen). The resistivity R_E of the resonator is calculated for actual dimensions of the key-hole shaped electrodes (see Fig. 1.1), langasite disk thickness d_R and conductivity σ_R. The platinum electrodes are assumed to exhibit infinite conductivity. Finally, the effective electrode area A_E is derived from

$$A_E = \frac{1}{\sigma_R}\frac{d_R}{R_E} \tag{B.1}$$

which represents a situation without fringing fields.

For the 5 MHz langasite resonators ($d_R \approx 273$ μm) with symmetrical electrodes the effective electrode area is 10.2 % larger than its geometrical area, i.e. $\gamma = 1.102$. For asymmetrical electrodes $\gamma = 1.135$ follows. These factors are used to calculate A_E of the resonators based on the dimension of their electrodes.

B.2 $TiO_{2-\delta}$ Films

Conductivity

The conductivity of the sensor film is a crucial property if its extend is larger than that of the underlaying platinum electrode. Under such circumstances, the effective electrode size varies as function of conductivity and impacts the resonance frequency as used for gas sensors (see Section 9.1).

The calculation of the effective electrode size requires the knowledge of the $TiO_{2-\delta}$ film conductivity. However, the property must be regarded in concert

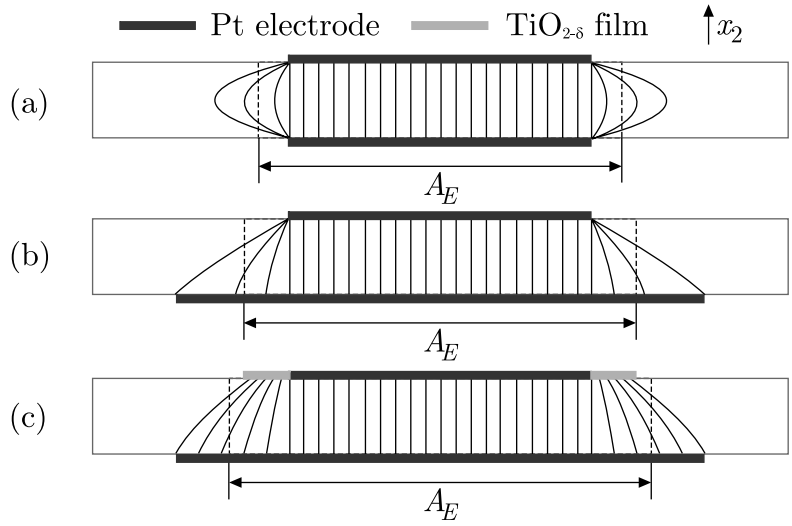

Figure B.1: Cross sections of circular TSM resonators and schematic view of the electric field for (a) symmetrical electrodes, (b) asymmetrical electrodes and (c) asymmetrical electrodes with additional $TiO_{2-\delta}$ film. The extent of the effective electrode area A_E which lies in the x_1–x_3 plane is indicated.

with the conductivity of the underlaying langasite substrate. The latter is expected to govern the overall behavior as long as $TiO_{2-\delta}$ is highly conductive. The fact follows immediately from the resistivity of a parallel arrangement of $TiO_{2-\delta}$ film and langasite crystal as visualized in Fig. B.2. These results are received by impedance spectroscopy using a langasite crystal with a $TiO_{2-\delta}$ film bridging two platinum electrodes located on one surface of the crystal. The constant resistivity above $p_{O2} \approx 10^{-16}$ bar indicates the dominance of the langasite substrate. Below that p_{O2} the conductivity of the $TiO_{2-\delta}$ film governs the overall resistivity. It must be noted that the measurements are performed in hydrogenous atmospheres at 600°C where the conductivity of langasite is p_{O2} independent above $p_{O2} \approx 10^{-20}$ bar, only. Consequently,

- $TiO_{2-\delta}$ films are expected to impact the resonance behavior below 10^{-16} bar for the thickness of film and substrate chosen here and
- The conductivity of $TiO_{2-\delta}$ can be extracted from this measurements between 10^{-16} and 10^{-20} bar, only.

In order to compare the conductivity of the $TiO_{2-\delta}$ films with literature data, the property is estimated taking into account the conductivity and dimensions of the underlaying langasite crystal. The results are shown in Fig B.3. Between 10^{-17} and 10^{-20} bar the negative slope of $-1/4$ in the log−log plot indicates n-type conduction behavior [99]. The mechanism corresponds to a partial reduction of the film. The conductivity can be described by

$$\sigma_F = \sigma_0 \, p_{O2}^{-1/4} \tag{B.2}$$

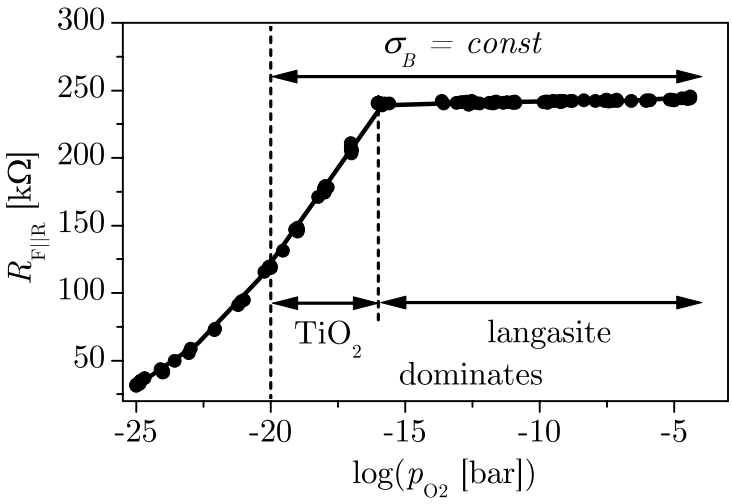

Figure B.2: Resistivity of a parallel arrangement of $TiO_{2-\delta}$ film and langasite resonator at 600°C.

with $\sigma_0 = 3.9 \times 10^{-4}$ S/m. Further, the magnitude of the conductivity corresponds to data published e.g. in [134, 135] where σ_0 ranges from 4.4×10^{-5} to 5.6×10^{-3} S/m. Below 10^{-20} bar, the slope in Fig B.3 is slightly altered which can be caused by impact of the langasite substrate or change of the predominant charge compensation mechanism in $TiO_{2-\delta}$.

In summary, the conductivity of the $TiO_{2-\delta}$ films used here fits into common patterns and shows, in particular, a p_{O2}-dependence of $-1/4$ in the log−log plot. The numerical values derived here are used in Appendix B to calculate the effective electrode size.

Effective Area

If the electrodes exhibit finite conductivity, the calculation must include the lateral resistance of the $TiO_{2-\delta}$ film which follows from Eq. B.2. The situation is illustrated in Fig. B.1c where the outer part of the top electrode consists of a $TiO_{2-\delta}$ film. Fig. B.4 presents the result for a 40 nm thick $TiO_{2-\delta}$ film. Remarkably, the area doubles if the p_{O2} approaches 10^{-20} bar. The calculation is confirmed by the measured change of the bulk resistivity presented as relative value R_S^0/R_S with $R_S^0 = \gamma R_S(10^{-6}$ bar).

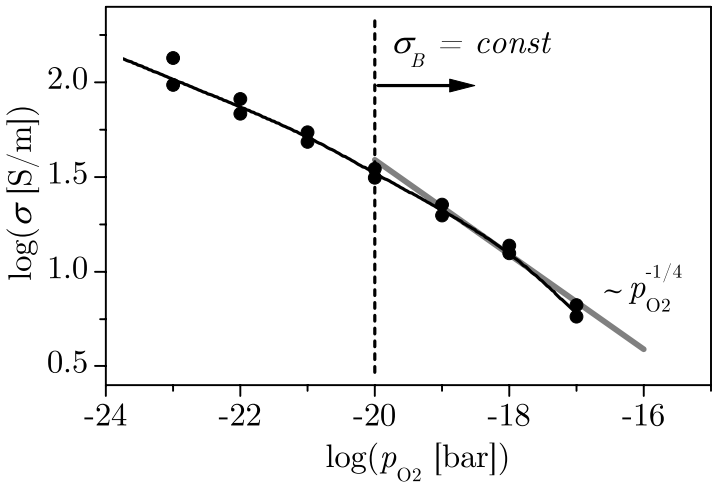

Figure B.3: Conductivity of the actual $TiO_{2-\delta}$ films as function of p_{O2}.

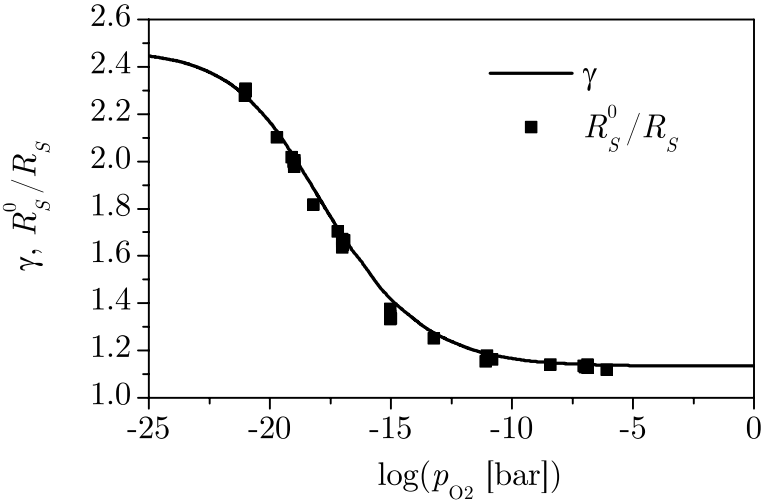

Figure B.4: Effective electrode area with respect to the geometrical area of the top platinum electrode calculated as function of p_{O2} for a 40 nm tick $TiO_{2-\delta}$ film and measured (relative) change of the bulk resistance.

Appendix C

Experimental Details

C.1 Sample Preparation

Single Crystalline Material

Crystal Growth

Nominally undoped and doped langasite single crystals are provided predominantly by the Institute for Crystal Growth, Berlin-Adlershof, Germany (IKZ Berlin) [30]. Furthermore, a single crystal is delivered by the Tohoku University, Institute for Materials Research, Japan [10]. These crystals are grown by the Czochralski technique. Thereby, starting powder is prepared by mixing stoichiometric amounts of La_2O_3, Ga_2O_3, and SiO_2 (purity 4N). After calcination, the material is charged into a crucible and heated. Subsequently, the crystals are pulled at a rate of 1.5 mm/h under N_2–2 % O_2. In addition, crystals purchased from AXTAL GmbH, Lobbach, Germany, and Mitsubishi Materials Corporation, Saitama, Japan, are included in initial investigations. Details about the growth process of the latter materials are not available. General information about the Czochralski method can be found in [26, 94, 136, 137].

Impurities and Dopants

The crystals from IKZ Berlin are grown in iridium crucibles. Undoped material appears transparent independent of its treatment in oxidizing or reducing atmospheres.

The crystal from Tohoku University is grown in a Pt-10 % Rh crucible which results in platinum and rhodium impurity concentrations of 0.08 and 0.6 %, respectively. The as grown material looks reddish and decolorizes by tempering in reducing atmospheres as confirmed by own experiments. The phenomenon is well known and does not influence the piezoelectric properties at room temperature [11]. The coloration can be attributed to color centers

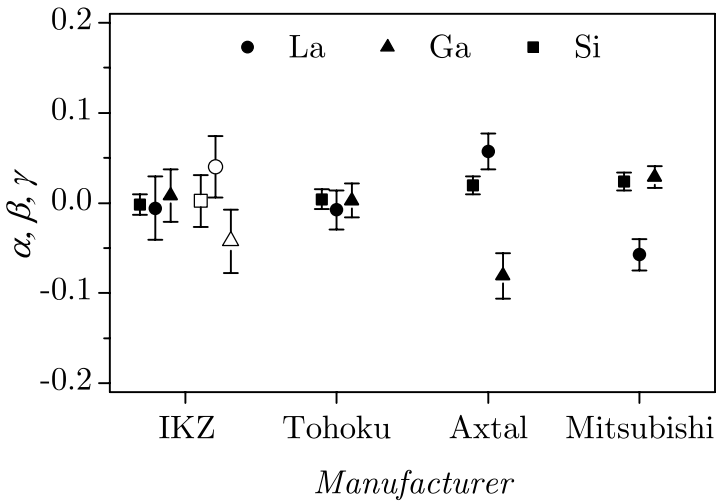

Figure C.1: Cation stoichiometry of langasite from different manufacturers according to $La_{3+\alpha}Ga_{5+\beta}Si_{1+\gamma}O_{14+\delta}$ determined by WDX (solid symbols) and ICP (open symbols).

which are formed by rhodium and OH-groups. Heating in oxygen increases the optical absorption at 0.58 μm and the transmission at 2.9 μm [138].

In particular large langasite crystals are suspected to show some fluctuation of their physical and chemical properties due to striation, inclusions, voids, dislocations and compositional variations. The latter can be caused by e.g. temperature fluctuations at the growth interface [89]. In order to evaluate the composition of the langasite crystals used here, WDX and ICP analysis is performed. Fig. C.1 shows the stoichiometry fluctuations for the cations[1] expressed as α, β and γ in the formula $La_{3+\alpha}Ga_{5+\beta}Si_{1+\gamma}O_{14+\delta}$. Obviously, only the crystals from IKZ Berlin and Tohoku University exhibit nearly stoichiometric compositions. Within a given crystal, the stoichiometry fluctuations are insignificant, i.e. smaller than the error bars given in Fig. C.1. The crystals from AXTAL and Mitsubishi Materials show significant deviations of the stoichiometric composition and are, therefore, largely excluded from further investigations.

Intentionally doped langasite single crystals are provided by IKZ Berlin. The growth process corresponds to that described above except for the partial replacement of lanthanum or gallium by the dopants, namely strontium, praseodymium and niobium.

[1]The oxygen content can not be determined satisfactorily by the methods applied here.

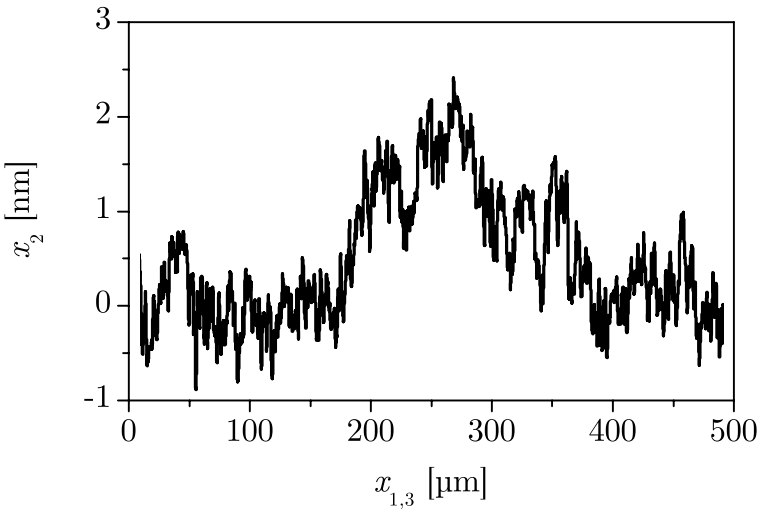

Figure C.2: Surface profile of a polished langasite resonator.

Polycrystalline Material

Further, polycrystalline langasite is provided by Dr. H. Seh, MIT. These samples are prepared by mixing and ball-milling stoichiometric amounts of La_2O_3, Ga_2O_3, and SiO_2. Subsequently, the powder is pressed into pellets and fired at 1450°C in air for 10 h. X-ray diffraction shows the material to be langasite with no observable second phases. Additionally, niobium, strontium and praseodymium doped samples are prepared. Densities of approximately 90 % are obtained while the grain size varied from 1 to 10 μm depending on the dopant. These samples are predominantly prepared for conductivity measurements as described in detail in [43]. Some of the polycrystalline samples are used in this work for the determination of the oxygen diffusion coefficients.

Resonator Device Preparation

The resonator preparation is performed by cutting langasite single crystals into circular plates and polishing. Thereby, special emphasis is taken on the parallelism of the surfaces. The surface roughness is in the order of a few nanometer as visualized in Fig. C.2. The thickness of the devices varied from about 200 to 800 μm.

Except stated otherwise, pre-annealing of the langasite samples in air is performed prior to the experiments in order to achieve oxygen equilibrium and, therefore, reproducible initial conditions. The minimum equilibration time is estimated according to Section 7.2. Since below 1000°C the resulting periods of time became infeasible, the minimum equilibration temperature applied here is 1050°C even if the subsequent experiments are performed at

lower temperatures.

Up to 400 nm thick key hole shaped platinum electrodes are deposited by pulsed laser deposition on both sides of the crystals. An intermediate titanium layer of about 10 nm improves the adhesive strength between the langasite plate and the platinum contact.

C.2 Experimental Setup

The experimental setup used to adjust temperature and gas atmosphere during the electrical characterization of the samples consists of a gas tight furnace with a nominal temperature accuracy of 0.1 K, a gas mixing system which provides Ar, O_2, H_2 and CO as well as an alumina sample holder with platinum wiring. During the high-temperature experiments, the gas atmosphere is essentially provided in two different fashions:

- Maintenance of a constant oxygen partial pressure for long periods of time. The gas flow rate is typically adjusted at 20 cm^3min^{-1}.
- Repeated switching of the atmosphere by pumping of rough vacuum and subsequent backfilling with either oxygen, argon or 6% H_2/Ar. The pumping process temporarily causes undefined temperature and pressure fluctuations.

The electrical measurements are performed either in ambient air, artificial air, CO/CO_2 or H_2/H_2O gas mixtures with Ar as carrier gas. The test of the sensing capabilities of coated langasite resonators is partially performed in atmospheres containing simultaneously CO and H_2.

CO, H_2 and Ar are premixed by a gas mixing system. Typical gas compositions and flow rates are 0.5 % H_2/Ar or 0.5 % CO/Ar and 20 cm^3min^{-1}, respectively. For the further calculations, the amount of gases provided to the reaction chamber is converted in their partial pressure.

In order to adjust the p_{O2}, oxygen is titrated into the reaction chamber via a zirconia oxygen ion pump (ZIROX GmbH, Greifswald, Germany). Thereby, a feedback-control unit enables maintenance of a constant oxygen partial pressure in the range from 1 to 10^{-25} bar. The system maintains the oxygen partial pressure with an accuracy of $\Delta\log(p_{O_2}[\text{bar}]) \leq 0.1$ at 600°C and above.

H_2/H_2O gas mixtures requires special attention. Beside the adjustment of the p_{O2} they enable reactions of hydrogenous species with the samples. During a given experiment, the amount of H_2 provided to the reaction chamber, denoted by p_{H2}^{RT}, is kept constant. Thus the resulting hydrogen partial pressure p_{H2} at elevated temperatures

$$p_{H2} = p_{H2}^{RT} - p_{H2O} \tag{C.1}$$

is reduced due to the formation of water vapor via

$$2\ H_2 + O_2 \rightarrow 2\ H_2O. \tag{C.2}$$

The equilibrium

$$p_{\mathrm{H2}}^2 p_{\mathrm{O2}} / p_{\mathrm{H2O}}^2 = const. \tag{C.3}$$

yields:

$$p_{H2O}^{\alpha} \sim p_{\mathrm{O2}} \tag{C.4}$$

with $\alpha = 2$ in the marginal case of very low p_{O2}. With increasing p_{O2}, α became p_{O2} dependent and increases.

C.3 Resonance Spectra

The electromechanical behavior of the resonators is investigated by monitoring the real and imaginary parts of the impedance spectra in the vicinity of the resonance frequency using a network analyzer (HP E5100A). This technique is useful even for heavily loaded resonators which could not support oscillations in an oscillator circuit. Further, it opens the possibility of studying more than the changes in resonance frequency.

The raw data are calibrated using the three-term calibration scheme described in [139].

C.4 Impedance Spectra

The electrical bulk resistance R_S and capacitance C_S of the samples are determined using an impedance analyzer (Solartron SI 1260). Both properties are part of the equivalent circuit as shown in Fig. 2.5a. The frequency range chosen for the measurements of 10 mHz to 1 MHz reflects the bulk properties and is much below the mechanical resonance frequency of the samples. Therefore, Z_M virtually does not impact the measurements.

The low frequency intercept of the $R_S - C_S$ semicircle in the complex impedance plane is interpreted as the bulk resistance and used to calculate the bulk conductivity σ_R according to Eq. 2.30.

The samples exhibit non-ideal behavior which is common and caused by e.g. rough surfaces or varying thickness of the samples [140]. As a result, the semicircles are slightly depressed. The fact requires the application of a constant phase element (CPE) instead of a pure capacitance for the actual fits. Its impedance Z_{CPE} can be described by the parameters T and P and the angular frequency ω

$$Z_{CPE} = \frac{1}{T\,(i\omega)^P}. \tag{C.5}$$

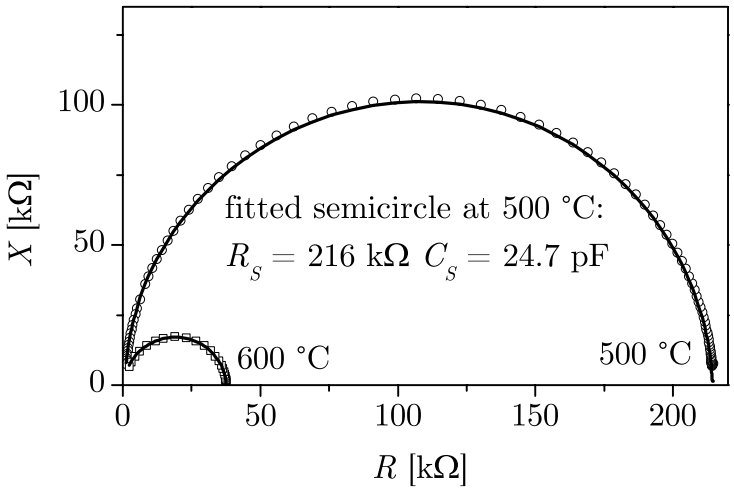

Figure C.3: Impedance of a langasite sample at 500 and 600°C in the low frequency range (10^{-1}–10^{6} Hz).

For further calculations, the complex part of the $R_{CPE}-Z_{CPE}$ circuit must be converted into a pure capacitance. Assuming identical resistances of ideal and depressed semicircle at low frequencies

$$R_S\,(\omega \to 0) = R_{CPE}\,(\omega \to 0) \tag{C.6}$$

and identical angular frequencies at the maximum of the respective semicircle

$$\omega_C\left(\frac{R_S}{2}\right) = \omega_{CPE}\left(\frac{R_S}{2}\right) \tag{C.7}$$

the capacitance C_S can be derived

$$C_S = R_S^{(1-P)/P} T^{1/P}. \tag{C.8}$$

Finally, the dielectric constant ε_R follows from Eq. 2.29.

Fig. C.3 shows an example for a fitted semicircle at 500 and 600 °C. At the latter temperature, the capacitance given in the plot corresponds to $C_S = (2.16\times10^5)^{(1-0.96)/0.96}(4.02\times10^{-11})^{1/0.96}$ F = 24.7 pF. For the specimen used here, the values for P range from 0.95 to 1.

C.5 Diffusion Coefficients

$^{16}O/^{18}O$ Exchange

Self-diffusion diffusion coefficients can be extracted by analysis of the movements of stable tracers within a given sample. Oxygen diffusion measurements base commonly on the exchange of the stable tracer isotope ^{18}O with

low natural abundance (0.206 at%), with that of naturally occurring ^{16}O in the solid.

In order to prepare the samples, pre-annealing runs are performed in artificial air at the same temperature and p_{O2} as the subsequent diffusion runs. Thereby, the period of time is chosen to be at least four times longer than that of the tracer diffusion. After pre-annealing, the samples are temporarily moved into a cooler area of the furnace ($\Delta T = 250°C$) to replace the gas atmosphere with $^{18}O_2$ enriched gas (typically 80...90 %). The samples are then exposed to the tracer at temperatures ranging from 500 up to 1000°C to achieve the $^{18}O - ^{16}O$ exchange. Subsequently, the resulting concentration profiles are determined by secondary ion mass spectrometry (SIMS, Cameca IMS 3f) or secondary neutral mass spectrometry (SNMS, VG SIMS Lab).

The ^{18}O concentration at the surface of the sample c_S is potentially lower than the concentration in the surrounding gas environment c_G. Therefore, the surface exchange kinetics must be taken into consideration.

Single Crystalline Material

The diffusion model given in [141] describes the such situations for a single diffusion mechanism. Here, the surface exchange kinetics and the bulk diffusion are expressed by K and D, respectively

$$k\,(c_G - c_S) = D\frac{\partial c}{\partial y}\bigg|_{y=0}. \tag{C.9}$$

The measured depth profiles are fitted by a least square regression procedure based upon the diffusion solution according to Eq. C.10

$$\frac{c(y,t)-c_{BG}}{c_G-c_{BG}} = \operatorname{erfc}\left(\frac{y}{2\sqrt{Dt}}\right) - \exp\left(\frac{k}{D}y+\frac{k^2}{D}t\right)\operatorname{erfc}\left(\frac{y}{2\sqrt{Dt}}+k\sqrt{\frac{t}{D}}\right) \tag{C.10}$$

where y, t and c_{BG} are the depth, the diffusion time and the natural background ^{18}O concentration, respectively.

Good agreement between the model and experimental data of the langasite single crystals could be achieved thereby confirming the occurrence of a single diffusion mechanism.

Polycrystalline Materials

The analytical solution in the form of Eq. C.10 cannot be applied if more than one diffusion mechanism takes place simultaneously. For example, polycrystalline samples exhibit diffusion in the volume and the grain boundaries.

The common way to plot the corresponding diffusion profiles is to express the logarithm of the concentration as a function of depth to the power of 6/5. The grain boundary term is then visible as the linear part of the concentration

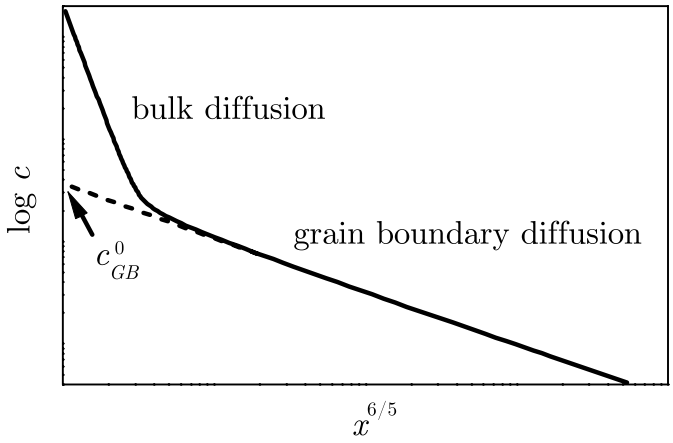

Figure C.4: Schematic concentration profile for tracer diffusion in polycrystalline materials.

profile, and from the slope the grain boundary diffusion coefficient can be calculated [142] when the volume diffusion coefficient is known. In this study, the analytical approach proposed in [143] is used. The linear part of the depth profile, plotted versus $x^{6/5}$ and extrapolated to $x = 0$, represents the contribution of grain boundaries, c^0_{GB} , approximated by

$$c^0_{GB} = 0.9\, c_G \lambda\, 2\sqrt{Dt}. \tag{C.11}$$

Here, λ and D are the grain boundary length per unit area and the bulk diffusion coefficient, respectively. Fig. C.4 visualizes the contributions of bulk and grain boundary diffusion to the diffusion profile. The grain boundary length may be extracted by processing cross sections of the specimen. Examples for diffusion profiles and cross sections of the specimen are given in [144]. A typical grain boundary length per unit area is $\lambda = (\,0.7 \pm 0.1)\ \mu\mathrm{m}^{-1}$.

Ion Implantation

The determination of the gallium diffusion coefficients can be performed using the stable isotope ^{71}Ga. The small difference in abundance of the gallium isotopes ^{69}Ga and ^{71}Ga (61 and 39 at%, respectively) requires the application of large quantities of ^{71}Ga. Nevertheless, a poor signal resolution during analysis has to be expected.

The isotope ^{71}Ga is implanted into the specimens at the Universität Frankfurt, Germany. The tracer, extracted from a gallium arsenate plasma, is accelerated to 50 keV and focused on the surface of y-cut langasite plates. The total amount of implanted ^{71}Ga ions is about $8{\times}10^{16}$ ions/cm^2. To

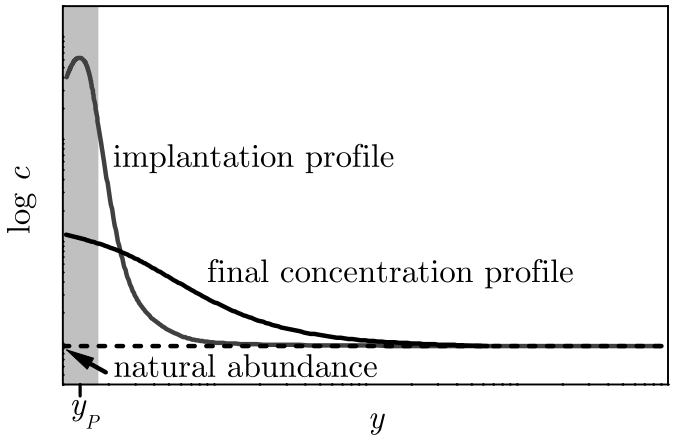

Figure C.5: Schematic concentration profile for ^{71}Ga where the tracer is implanted at the surface region of the sample. The area of damaged crystal structure is gray shaded.

avoid electrical charging of the surface, the samples are treated with an additional electron beam. The subsequent diffusion runs are performed in air at temperatures from 700 up to 1000°C.

^{71}Ga is implanted by a 50 keV accelerator. Damage of the lattice in the implanted region is, therefore, expected and the evaluation of the diffusion coefficients must account for the damaged region. A schematic implantation profile is shown in Fig. C.5.

Fick's second law still describes the transport. But the equation has to be solved numerically by e.g. using the Crank-Nicolson scheme [73]. As boundary condition, the flux of particles at the surface is described by the surface exchange coefficient K_{Ga} according to Eq. C.9 with c_G and c_S as the concentration of ^{71}Ga in the gas phase and the in the sample close to the surface, respectively. It should be noted that this expression can be used to estimate the rate of gallium loss from the surface by evaporation. Further, there is no particle flux assumed at positions which are at least twice as deep as the penetration depth of the implanted ions (assumption of semi-infinite solid). The initial condition is given by the concentration profile of ^{71}Ga, obtained from the sample before annealing. The determination of the gallium diffusion coefficient is performed using a simplex fit algorithm [73] which minimizes χ^2, i.e. the sum of the squared differences of data and fit function is minimized. Fit parameters are the surface exchange coefficient K and two diffusion coefficients, D^D_{Ga} and D_{Ga}. They describe the ^{71}Ga diffusion in the damaged surface region and the langasite lattice, respectively. D^D_{Ga} is introduced to allow a reasonable fit and is applied in a depth range from $y = 0$ to $y = 2x_P$, where x_P is the position of maximum of the initial ^{71}Ga concentration as indicated in Fig. C.5).

Appendix D

Terms and Acronyms

Terms and conventions used in this work are defined. Further, symbols and acronyms are listed.

D.1 Terms and Conventions

α-quartz is commonly denoted by *quartz*, only.

Complex quantities are not indicated explicitly except they have to be distinguished from their real or imaginary part. If the latter is required, the complex quantity is marked by a hat as seen e.g. in Eq. 2.15.

Concentrations of dopants etc. are given as molecular percentage.

Indices of the EC parameters refer to the physical property therein having the strongest impact in the respective context (e.g. temperature dependence).

Overtones are denoted by (odd) numbers corresponding to the vibration nodes. For example, the fundamental mode and the 1^{st} overtone are indexed by $N = 1$ and 3 , respectively. Frequencies without index refer to the fundamental mode.

Resonance spectra are impedance spectra acquired in the vicinity of the resonance frequency.

Undoped or nominally undoped langasite crystals are not intentionally doped. Independent of the potential presence of impurities they are denoted as *undoped*.

D.2 Symbols

A_E	Effective area of the electrodes
A_R	Effective area of the resonator device
B	Susceptance, imaginary part of the admittance
$c^{[N]}$	Linear temperature coefficient of overtone N
c_0, c_1, c_2	Temperature coefficients in polynomial expressions
c_{66}	Shear modulus
$c_{66[..]}$	Approximation of c_{66} for high [+] and low temperatures [-]
C_c	Capacitance in X_c
c_F	Shear modulus of the film material
c_G, c_S	Concentration in the gas phase and the sample, respectively
c_{ij}	Mechanical stiffness
C_L	Stray capacitance
C_M	Motional capacitance of the resonator device
$C_{M[..]}$	Approximation of C_M for high [+] and low temperatures [-]
c_R	Piezoelectrically stiffened shear modulus of the resonator material(x_2-direction)
c_{RT}	c_{66} at room temperature
C_S	Static capacitance of the resonator device
$c_{[..]}$	Concentration of species [..]
$C_{\sigma-}$	Capacitance in $X_{\sigma-}$
C_ε	Capacitance in X_σ
d	Piezoelectric constant [C/N]
D	Electrical displacement
D_0	Pre-exponential factor
d_R, d_F	Thickness of resonator and film, respectively
$D_{[..]}$	Diffusion coefficient of species [..]
e	Piezoelectric constant [C/m^2]
E_A	Activation energy
e_R	Piezoelectric constant of the resonator material(x_2-direction)
$e_{R[..]}$	Approximation of e_R for high [+] and low temperatures [-], respectively
E	Electrical field
E_D	Dissipated energy
E_S	Stored energy
f_{EP}, f_{IC}	Temperature compensated frequency by external and internal temperature measurement, respectively
$f_P^{[N]}$	Parallel resonance frequency of overtone N
f_{RT}	Resonance frequency at room temperature
$f_S^{[N]}, f^{[N]}$	Series resonance frequency of overtone N
G	Conductance, real part of the admittance
I	Electrical current

I_S, I_M	Current through the static and the motional arm, respectively
k_B	Boltzmann constant
K^2	Electromechanical coupling coefficient of the resonator material
$k_{[..]}$	Reaction constant for reaction denoted by [..]
$k_{R,A}, k_{R,D}$	Reaction constants for reduction in the presence of acceptors and donors, respectively
K, $K_{[..]}$	Surface exchange coefficient, surface exchange coefficient of species [..]
L_M	Motional inductance of the resonator device
$L_{M[..]}$	Approximation of L_M for high [+] and low temperatures [-]
L_ρ	Inductance in X_ρ
L_σ	Inductance in X_σ
$L_{\sigma+}$	Inductance in $X_{\sigma+}$
M_R	Resonator mass
n	Concentration of electrons
N	Overtone number
p	Concentration of holes
p_{H2}	Hydrogen partial pressure
p_{H2}^{RT}	Hydrogen partial pressure at room temperature
p_{H2O}	Water vapor partial pressure
p_{O2}	Oxygen partial pressure
Q	Resonator quality factor (Q-factor)
Q_0	Q-factor for the motional arm
Q_{BvD}	Q-factor derived from the BvD model
Q_{BW}	Q-factor derived from the bandwidth approach
$Q_{BvD[..]}$	Approximation of Q_{BvD}, for high [+] and low temperatures [-]
Q_c, Q_e	Q-factor related to the mechanical loss and to the imaginary part of the piezoelectric constant, respectively
$Q_{c,\eta}, Q_{c,\sigma}$	Dissipation factor related to mechanical losses; viscosity and conductivity contribution, respectively
$q_{[..]}$	Charge of species [..]
R	Resistance, real part of the impedance
r_E	Radius of the electrode
R_L	Lead resistance
R_M	Real part of Z_M^R
R_{M+}	Approximation of R_M for high temperatures
$R^{[N]}$	Mass resolution of overtone N
R_S	Static resistance of the resonator device
R_η, R_σ	Contribution to R_M, dominated by η_R and σ_R, respectively
$R_{\sigma[..]}$	Contribution to R_σ with positive [+] and negative temperature coefficient [-]
S	Mechanical strain
S_{IC}	Mass sensitivity after internal temperature compensation
$S_m^{[N]}$	Mass sensitivity of overtone N

t	Time
T	Mechanical stress, temperature
T_0	Nominal operation temperature
T_{TC}	Turnover temperature
u	Displacement
x	Space coordinates ($x_1 = x,\ x_2 = y,\ x_3 = z$)
X	Reactance, imaginary part of the impedance
X_c,X_ρ,X_σ	Contribution to X_M dominated by c_R, ρ_R and σ_R, respectively
X_M	Imaginary part of Z_M^R
$X_{\sigma[..]}$	Approximations of X_σ for high [+] and low temperatures [-]
Y	Admittance
Z	Electrical impedance, impedance of the resonator
Z_M	Motional impedance of the resonator device
Z_M^E	Motional impedance of the resonator wearing identical films on both sides
Z_M^F	Motional impedance of the film
Z_M^R	Motional impedance of the unperturbed resonator
Z_M^S	Motional impedance of the resonator wearing a film on one side
Z_S	Static impedance of the resonator device
Z_T	Impedance of resonator and holder
$\|Z\|$	Impedance modulus
α	Exponent describing the correlation of partial pressures
α_R, α_F	Acoustic phase shift inside resonator and film, respectively
χ^2	Sum of the squared differences of data and fit function
δ	Dissipation factor
δ_c	Dissipation factor related to mechanical losses
ϵ_R	Imaginary part of the piezoelectric constant of the resonator material
η_0	Temperature independent contribution of the effective viscosity
η_F	Effective viscosity of the film material
η_R	Effective viscosity of the resonator material
$\eta_{R[..]}$	Approximation of η_R for high [+] and low temperatures [-]
$\kappa_{[..]}$	Relative derivative of the frequency for the parameter [..]
$\mu_{[..]}$	Mobility of species [..]
$\nu_{[..]}$	Relative derivative of the Q-factor for the parameter [..]
ω	Angular frequency
ϕ	Electrical potential
$\varphi(f)$	Phase angle
ρ_F	Density of the film material
ρ_R	Density of the resonator material
σ_B	Electrical bulk conductivity
σ_f	Standard derivation
σ_R	Electrical conductivity of the resonator material
ε	Dielectric constant

ε_R	Dielectric constant of the resonator material (x_2-direction)
ζ_{Fn}	Normalized acoustic load impedance

D.3 Acronyms

BAW	Bulk Acoustic Wave
BvD	Butterworth-van Dyke
CPE	Constant Phase Element
CTE	Coefficient of Thermal Expansion
EC	Equivalent Circuit
FTIR	Fourier Transform InfraRed spectroscopy
HTMB	High-Temperature Micro Balance
ICP	Inductive Coupled Plasma
LSM	Lanthanum Strontium Manganate
pc	Polycrystalline
PLD	Pulsed Laser Deposition
QCM	Quartz Crystal Microbalance
Q	Resonator quality factor (Q-factor)
RT	Room Temperature
SAW	Surface Acoustic Wave
sc	Single crystalline
SIMS	Secondary Ion Mass Spectrometry
SNMS	Secondary Neutral Mass Spectrometry
TSM	Thickness Shear Mode
WDX	Wavelength Dispersive X-ray spectroscopy
VTE	Vapor Transport Equilibration
XRD	X-Ray Diffractometry

Bibliography

[1] G. Sauerbrey, *Verwendung von Schwingquarzen zur Wägung dünner Schichten und zur Mikrowägung*, Z. Phys. **155** (1959) 206–222.

[2] E. Benes, *Improved quartz microbalance technique*, J. Appl. Phys. **56** (1984) 608–626.

[3] S. S. Narine, A. J. Slavin, *Use of the quartz crystal microbalance to measure the mass of submonolayer deposits: Measuring the stoichiometry of surface oxides*, J. Vac. Sci. Technol. **A16** (1998) 1857–1862.

[4] O. Knacke, O. Kubaschewski, H. Hesselmann, *Thermochemical Properties of Inorganic Substances*, Springer, 1991.

[5] R. W. Cernosek, J. R. Bigbie, M. T. Anderson, J. H. Small, P. S. Sawyer, *High Temperature Hydrocarbon Gas Sensing with Mesoporous SiO_2 Thin Films on TSM Resonators*, presented at: Solid-State Sensor and Actuator Workshop, Hilton Head Island, South Carolina, Nov. 8-11, 1998.

[6] D. Damjanovic, *Materials for High Temperature Piezoelectric Transducers*, Curr. Opin. Solid State Mat. Sci. **3** (1998) 469–473.

[7] L. Reindl, G. Scholl, T. Ostertag, H. Scherr, U. Wolff, F. Schmidt, *Theory and application of passive SAW radio transponder as sensors*, IEEE Trans. Ultrason. Ferroel. Freq. Contr. **45** (1998) 1281–1292.

[8] R. Fachberger, G. Bruckner, G. Knoll, R. Hauser, J. Biniasch, L. Reindl, *Applicability of $LiNbO_3$, Langasite and $GaPO_4$ in High Temperature SAW Sensors Operating at Radio Frequencies*, IEEE Trans. Ultrason. Ferroel. Freq. Contr. (2004) 1427–1431.

[9] D. P. Birnie III, *Analysis of diffusion in lithium niobate*, J. Mat. Sci. **28** (1993) 302–315.

[10] K. Shimamura, H. Takeda, T. Kohno, T. Fukuda, *Growth and Characterization of Lanthanum Gallium Silicate $La_3Ga_5SiO_{14}$ Single Crystals for Piezoelectric Applications*, J. Cryst. Growth **163** (1996) 388–392.

[11] B. Chai, J. L. Lefaucheur, Y. Y. Ji, H. Qiu, *Growth and Evaluation of Large Size LGS ($La_3Ga_5SiO_{14}$), LGN ($La_3Ga_{5,5}Nb_{0,5}O_{14}$) and LGT ($La_3Ga_{5,5}Ta_{0,5}O_{14}$) Single Crystals*, IEEE Int. Freq. Contr. Symp. (1998) 748–760.

[12] P. W. Krempl, *Quartzhomeotypic gallium orthophosphate: A new high tech piezoelectric crystal*, Ferroelectrics **202** (1997) 65–69.

[13] K. Jacobs, P. Hofmann, D. Klimm, J. Reichow, M. Schneider, *Structural Phase Transformations in Crystalline Gallium Orthophosphate*, J. Solid State Chem. **149** (2000) 180–188.

[14] F. Krispel, C. Reiter, J. Neubig, F. Lenzenhuber, P. W. Krempl, W. Wallnöfer, P. M. Worsch, *Properties and Applications of Singly Rotated $GaPO_4$ Resonators*, IEEE Int. Freq. Contr. Symp. (2003) 668–673.

[15] M. Strassburg, J. Senawiratne, N. Dietz, U. Haboeck, A. Hoffmann, V. Noveski, R. Dalmau, R. Schlesser, Z. Sitar, *The growth and optical properties of large, high-quality AlN single crystals*, J. Appl. Phys. **6** (2004) 5870–5876.

[16] A. D. Katnani, K. I. Papathomas, *Kinetics and initial stages of oxidation of aluminum nitride: thermogravimetric analysis and x-ray photoelectron spectroscopy study*, J. Vac. Sci. Technol. **A5** (1987) 1335–1340.

[17] A. Bellosi, E. Landi, A. Tampieri, *Oxidation behavior of aluminum nitride*, J. Mat. Res. **8** (1993) 565–572.

[18] O. Ambacher, M. S. Brandt, R. Dimitrov, R. A. Fischer, A. Miehr, T. Metzger, M. Stutzmann, *Thermal Stability and Desorption of Group III Nitrides Prepared by MOCVD*, J. Vac. Sci. Technol. **14** (1996) 3532–3542.

[19] P. Krempl, G. Schleinzer, W. Wallnöfer, *Gallium phosphate, $GaPO_4$: A New Piezoelectric Crystal Material for High-Temperature Sensorics*, Sens. Actuators, A **61** (1997) 361–363.

[20] D. Cachau-Herreillat, J. Bennazha, A. Goiffon, A. Ibanez, E. Philippot, *X-ray, DTA and crystal growth investigation on $AlPO_4$-$GaPO_4$ and $AlPO_4$-$AlAsO_4$ systems*, Eur. J. Solid State Inorg. Chem. **29** (1992) 1295–1307.

[21] S. Uda, S. Q. Wang, N. Konishi, H. Inaba, J. Harada, *Growth habits of 3 and 4-inch Langasite Single Crystals*, J. Cryst. Growth **237–239** (2002) 707–713.

[22] K. Jacobs, P. Hofmann, D. Klimm, *OH impurities in $GaPO_4$ crystals: correlation between infrared absorption and mass loss during thermal treatment*, J. Cryst. Growth **237–239** (2002) 837–842.

[23] R.-U. Barz, M. Grassl, P. Gille, *Study of anisotropic effects in hydrothermal growth of gallium orthophosphate single crystals*, Ann. Chim. Sci. Mat. **26** (2001) 95–98.

[24] K. Jacobs, P. Hofmann, J. Reichow, *Physico-chemical aspects of the hydrothermal growth of $GaPO_4$*, Ann. Chim. Sci. Mat. **26** (2001) 85–90.

[25] O. Cambon, P. Yot, D. Balitsky, A. Goiffon, E. Philippot, B. Capelle, J. Detaint, *Crystal growth of $GaPO_4$, a very promising material for manufacturing BAW devices*, Ann. Chim. Sci. Mat. **26** (2001) 79–84.

[26] B. V. Mill, Y. V. Pisarevsky, *Langasite-type Materials: From Dicovery to Present State*, Proc. IEEE/EIA Int. Freq. Control Symp. (2000) 133–144.

[27] A. N. Gotalskaya, D. I. Drezin, V. V. Bezdelkin, V. N. Stassevich, *Pecularities of technology, physical properties and applications of new piezoelectric material langasite ($La_3Ga_5SiO_{14}$)*, IEEE Int. Freq. Contr. Symp. (1993) 339–347.

[28] J. Bohm, E. Chilla, C. Flannery, H.-J. Fröhlich, T. Hauke, R. Heimann, M. Hengst, U. Straube, *Czochralski growth and characterization of piezoelectric single crystals with langasite structure: LGS, LGN and LGT. Part II: Piezoelectric and elastic properties*, J. Cryst. Growth **216** (2000) 293–298.

[29] J. Boy, R. Besson, E. Bigler, R. Bourquin, B. Dulmet, *Theoretical and experimental studies of the force-frequency effectin BAW LGS and LGT resonators*, IEEE Int. Freq. Contr. Symp. (2001) 223–226.

[30] S. Ganschow, C. Cavalloni, P. Reiche, R. Uecker, *Growth of $La_3Ga_5SiO_{14}$: A Modern Material for High-Temperature Piezoelectric Application*, Proc. SPIE **2373** (1995) 55–58.

[31] H. Takeda, S. Tanaka, S. Izukawa, H. Shimizu, T. Nishida, T. Shiosaki, *Effective Substitution of Aluminum for Gallium in Langasite-type Crystals for A Pressure Sensor Use at High Temperature*, IEEE Ultras. Symp. (2005) 560–563.

[32] E. N. Domoroshchina, A. B. Dubovskii, G. M. Kuz'micheva, G. V. Semenkovich, *Influence of Point Defects on the Electrical Conductivity and Dielectric Properties of Langasite*, Inorg. Mater. **41** (2005) 1378–1381.

[33] J. Hornsteiner, E. Born, G. Fischerauer, E. Riha, *Surface Acoustic Wave Sensors for High Temperature Applications*, IEEE Int. Freq. Contr. Symp. (1998) 615–620.

[34] H. Fritze, H. L. Tuller, G. Borchardt, T. Fukuda, *High Temperature Properties of Langasite*, Mater. Res. Soc. Symp. Proc. **604** (2000) 65–70.

[35] H. Fritze, H. L. Tuller, *Langasite for High Temperature Bulk Acoustic Wave Applications*, Appl. Phys. Lett. **78** (2001) 976–977.

[36] H. Fritze, H. Seh, H. L. Tuller, G. Borchardt, *Operation Limits of Langasite High Temperature Nanobalances*, J. Europ. Ceram. Soc **21** (2001) 1473–1477.

[37] H. Fritze, M. Schulz, H. Seh, H. L. Tuller, *High Temperature Operation and Stability of Langasite Resonators*, Mater. Res. Soc. Symp. Proc. **835** (2005) 157–162.

[38] J. Sauerwald, H. Fritze, E. Ansorge, S. Schimpf, S. Hirsch, B. Schmidt, *Electromechanical properties of langasite structures at high temperatures*, presented at: International Workshop on Integrated Electroceramic Functional Structures, Berchtesgaden, Germany, June 6-8, 2005.

[39] D. Richter, H. Fritze, T. Schneider, P. Hauptmann, N. Bauersfeld, K.-D. Kramer, K. Wiesner, M. Fleischer, G. Karle, A. Schubert, *Integrated High Temperature Gas Sensor System Based on Bulk Acoustic Wave Resonators*, Sens. Actuators, B **118** (2006) 466–471.

[40] C. Reiter, P. W. Krempl, H. Thanner, W. Wallnöfer, P. M. Worsch, *Material Properties of GaPO4 and their Relevance for Application*, Ann. Chim. Sci. Mat. **26** (2001) 91–94.

[41] H. Fritze, O. Schneider, G. Borchardt, *High temperature bulk acoustic wave properties of gallium orthophosphate and langasite*, presented at: International Meeting on Chemical Sensors, Boston, July 8-10, 2002.

[42] H. Fritze, O. Schneider, G. Borchardt, *High Temperature Bulk Acoustic Wave Properties of Gallium Orthophosphate and Langasite*, Sensor 2003 Proceedings, AMA Service GmbH .

[43] H. Seh, *Langasite bulk acoustic wave resonant sensor for high temperature applications*, Ph.D. thesis, Department of Materials Science and Engineering, MIT, Cambridge, MA, USA (2005).

[44] H. Fritze, H. L. Tuller, *High-Temperature Balance*, U.S. Patent No. 6.370.955 .

[45] H. Fritze, H. L. Tuller, *Sensor, Sensoranordnung und Messverfahren*, PCT/DE 03/03774 (submitted).

[46] D. A. Berlincourt, D. Curran, H. Jaffe, *Physical Acoustics, Principles and Methods*, Vol. 1–Part A, Academic Press, 1964, Ch. 3 Piezoelectric and Piezomagnetic Materials and their Function in Transducers, pp. 169–270.

[47] T. Ikeda, *Fundamentals of Piezoelectricity*, Oxford University Press, 1990.

[48] *IEEE Standard on Piezoelectricity, ANSI/IEEE Std. 176-1987*, The Institute of Electrical and Electronic Engineers, New York, 1988.

[49] K. W. Kwok, H. L. W. Chan, C. L. Choy, *Evaluation of the Material Parameters of Piezoelectric Materials by Various Methods*, IEEE Trans. Ultrason. Ferroel. Freq. Contr. (1997) 733–742.

[50] J. Wang, Y.-K. Yong, T. Imai, *Finite Element Analysis of the Piezoelectric Vibrations of Quartz Plate Resonators With Higher-order Plate Theory*, IEEE Int. Freq. Contr. Symp. (1997) 650–58.

[51] H. F. Tiersten, *A Derivation of Two-dimensional Equations for the Vibration of Electroded Piezoelectric Plates Using an Unrestricted Thickness Expansion of the Electric Potential*, IEEE Int. Freq. Contr. Symp. (2001) 571–579.

[52] P. C. Y. Lee, J. D. Yu, W. S. Lin, *A New 2-D Theory for Vibrations of Piezoelectric Crystal Plates with Electroded Faces*, IEEE Ultras. Symp. (1996) 1591–94.

[53] R. D. Mindlin, H. Deresiewicz, *Thickness-Shear Vibration of Piezoelectric Crystal Plates with Incomplete Electrodes*, J. Appl. Phys. **25** (1954) 21–24.

[54] H. F. Tiersten, *Linear Piezoelectric Plate Vibration*, Plenum Press, 1969.

[55] C. E. Reed, K. K. Kanazawa, J. H. Kaufman, *Physical Description of a Viscoelastically Loaded AT-cut Quartz Resonator*, J. Appl. Phys. **68** (1990) 1993–2001.

[56] J. Vig, *Quartz Crystal Resonators and Oscillators*, www.ieee-uffc.org/freqcontrol/tutorials/, 2005.

[57] D. Salt, *Hy-Q handbook of Quartz Crystal Devices*, Van Nostrand Reinhold (UK) Co. Ltd, 1987.

[58] B. Zimmermann, R. Lucklum, P. Hauptmann, J. Rabe, S. Büttgenbach, *Electrical Characterisation of High-Frequency Thickness Shear-Mode Resonators by Impedance Analysis*, Sens. Actuators, B **76** (2001) 47–57.

[59] J. G. Smith, *Influence of Moving Domain Walls and Jumping Lattice Defects on Complex Material Coefficients of Piezoelectrics*, IEEE Trans. Sonics Ultras. (1976) 168–174.

[60] G. Arlt, *The Role of Domain Walls on the Dielectric, Elastic and Piezoelectric Properties of Ferroelectric Ceramics*, Ferroelectrics **76** (1987) 451–458.

[61] R. Lucklum, P. Hauptmann, *Determination of Shear Modulus with Quartz Crystal Resonators*, Faraday Discuss. **107** (1997) 123–140.

[62] C. Behling, *The Non-gravimetric Response of Thickness Shear Mode Resonators for Sensor Applications*, Ph.D. thesis, Otto-von-Guericke-Universität Magdeburg (1999).

[63] B. A. Martin, H. E. Hager, *Velocity profile on quartz crystals oscillating in liquids*, J. Appl. Phys. **65** (1989) 2630–2635.

[64] G. Sauerbrey, *Messung von Plattenschwingungen sehr kleiner Amplitude durch Lichtmodulation*, Z. Phys. **178** (1964) 457–471.

[65] C. Behling, R. Lucklum, P. Hauptmann, *Possibilities and Limitations in Quantitative Determination of Polymer Shear Parameters by TSM Resonators*, Sens. Actuators, A **61** (1997) 260–266.

[66] K. S. van Dyke, *The piezoelectric resonator and its equivalent network*, Proceedings of the Institute of Radio Engineers (1928) 742–764.

[67] S. Butterworth, *Electrically maintained vibrations*, Proc. Phys. Soc (1915) 410–424.

[68] B. Friedland, O. Wing, R. Ash, *Principles of Linear Networks*, McGraw-hill Book Company, 1961.

[69] W. Göpel, J. Hesse, Z. J. N., *Sensors, A Comprehensive Survey, Vol. 7*, VCH Weinheim, 1994.

[70] R. Lucklum, C. Behling, R. W. Cernosek, S. J. Martin, *Determination of complex shear modulus with thickness shear mode resonators* , J. Phys. D: Appl. Phys. **30** (1997) 346–356.

[71] A. Bund, G. Schwitzgebel, *Signal oscillations of a piezoelectric quartz crystal caused by compressional waves*, Anal. Chim. Acta **364 (1)** (1998) 189–194.

[72] A. Altindal, R. Patel, R. Zhou, F. Josse, Z. Ozturk, O. Bekaroglu, *Soluble dodecylsulfanylphthalocyanines as sensitive coatings forchemical sensors in gas phase*, IEEE Int. Freq. Contr. Symp. (1998) 676–684.

[73] W. H. Press, B. P. Flannery, S. A. Teukolsky, W. T. Vetterling, *Numerical Recipes in Pascal*, Cambridge University Press, New York .

[74] D. R. Lide (Ed.), *CRC Handbook of Chemistry and Physics, 84th Edition.*, CRC Press, 2003.

[75] J. A. Kosinski, R. A. Pastore, Jr., E. Bigler, M. Pereira da Cunha, C. D. Malocha, J. Detaint, *A Review of Langasite Material Constants from BAW and SAW Data: Toward an Improved Data Set*, IEEE Int. Freq. Contr. Symp. (2001) 278–286.

[76] Piezocryst GmbH, *Data sheet: $GaPO_4$ material constants, Update 11/2005*, http://www.piezocryst.com (2005).

[77] M. Schulz, H. Fritze, U. Straube, *Determination of Material Parameters of Langasite ($La_3Ga_5SiO_{14}$) at Elevated Temperatures*, presented at: 345th Wilhelm and Else Heraeus Seminar: "Acoustic Wave Based Sensors: Fundamentals, Concepts, New Applications", Bad Honnef, Germany, April 11-13, 2005.

[78] J. Schreuer, J. Rupp, C. Thybaut, J. Stade, *Temperature dependence of elastic, piezoelectric and dielectric properties of $La_3Ga_5SiO_{14}$ and $La_3Ga_{5.5}Ta_{0.5}O_{14}$: An application of resonant ultrasound spectroscopy*, IEEE Ultras. Symp. (2002) 360–363.

[79] J. Schreuer, C. Thybaut, *Anelastic relaxation effects and elastic instabilities in CGG-type compounds*, IEEE Ultras. Symp. (2005) 695–698.

[80] M. Schulz, *Untersuchung der Eigenschaften von Langasit für Hochtemperaturanwendungen*, Ph.D. thesis, Technische Unversität Clausthal (2007).

[81] W. Johnson, S. Kim, S. Uda, *Acoustic Loss in Langasite and Langanite*, Proc. IEEE Int. Freq. Contr. Symp. (2003) 646–649.

[82] J. J. Martin, *Acoustic Loss in Cultured Quartz*, IEEE Int. Freq. Contr. Symp. (1996) 170–178.

[83] J. J. Martin, *High-temperature Acoustic Loss In Thickness-Shear Mode Quartz Resonators*, IEEE/EIA Int. Freq. Contr. Symp. (2000) 359–363.

[84] R. C. Smythe, R. C. Helmbold, G. E. Hague, K. A. Snow, *Langasite, Langanite, and Langatate Bulk-Wave Y-Cut Resonators*, IEEE Trans. Ultrason. Ferroel. Freq. Contr. **47** (2000) 355–360.

[85] S. A. Sakharov, P. Senushencov, A. Medvedev, Y. Pisarevsky, *New Data on Temperature Stability and Acoustical Losses of Langasite Crystals*, Proc. IEEE Int. Freq. Contr. Symp. (1995) 647–652.

[86] D. S. Steavens, H. F. Tiersten, *An Analysis of Doubly-Rotated Contured Crystal Resonators*, IEEE Transactions (1985) 436–444.

[87] B. Neubig, W. Briese, *Das große Quarz-Kochbuch*, Franzis-Verlag, 1997.

[88] J. Stade, L. Bohaty, M. Hengst, R. B. Heimann, *Electro-optic, Piezoelectric and Dielectric properties of Langasite ($La_3Ga_5SiO_{14}$), Langanite ($La_3Ga_{5.5}Nb_{0.5}O_{14}$) and Langataite ($La_3Ga_{5.5}Ta_{0.5}O_{14}$)*, Cryst. Res. Technol. **37** (2002) 1113–1120.

[89] C. Klemenz, M. Berkowski, B. Deveaud-Pledran, D. C. Malocha, *Defect Structure of Langasite-type Crystals: A Challange for Applications*, IEEE Int. Freq. Contr. Symp. (2002) 301–306.

[90] R. Fachberger, E. Riha, E. Born, W. Ruile, P. Pongratz, S. Kronholz, *Homogeneity of Langasite and Langatate Wafers*, IEEE Int. Freq. Contr. Symp. (2002) 311– 319.

[91] G. M. Kuz'micheva, V. B. Rybakov, E. N. Domoroshchina, A. B. Dubovskii, *X-ray Diffraction Study of an Inhomogeneous Langasite ($La_3Ga_5SiO_{14}$) Crystal*, Inorg. Mater. **38** (2002) 1040–1047.

[92] A. Kaminskii, B. Mill, G. Khodzhabagyan, A. Konstantinova, O. A.I., I. Silvestrova, *Investigation of trigonal $(La_{1-x}Nd_x)_3Ga_5SiO_{14}$ crystals: I. Growth and Optical Properties*, Phys. Stat. Sol. (A) **80** (1983) 387–398.

[93] I. H. Jung, Y. H. Kang, K. Joo, A. Yoshikawa, T. Fukuda, K. Auh, *$Ca_3Ga_2Ge_4O_{14}$ (CGG)-type $Sr_3Nb_{0.95}Ga_{3.083}Si_2O_{14}$ single crystal grown by the Czochralski method for piezoelectric applications*, Mater. Lett. **51** (2001) 129–134.

[94] B. H. T. Chai, A. N. P. Bustamante, M. C. Chou, *A new class of ordered langasite structure compounds*, IEEE/EIA Int. Freq. Contr. Symp. (2000) 163–168.

[95] H. Seh, H. L. Tuller, *Defects and Transport in Langasite I: Acceptor-doped ($La_3Ga_5SiO_{14}$)*, J. Electroceram. **16** (2006) 115–125.

[96] H. Seh, H. L. Tuller, *Defects and Transport in Langasite II: Donor-doped $La_3Ga_{4.75}Nb_{0.25}SiO_{14}$*, J. Electroceram. **15** (2006) 192–202.

[97] H. Seh, H. L. Tuller, H. Fritze, *Defect Properties of Langasite and Effects on BAW Gas Sensor Performance at High Temperatures*, J. Eur. Ceram. Soc. **24** (2004) 1425–1429.

[98] F. A. Kröger, *The Chemistry of Imperfect Crystals*, North Holland, Amsterdam, 1964.

[99] Y.-M. Chiang, D. P. Birnie III, W. D. Kingery, *Physical ceramics*, John Wiley & Sons, 1996.

[100] R. H. Doremus, *Diffusion of Reactive Molecules in Solids and Melts*, John Wiley & Sons, 2002.

[101] R. Glöckner, A. Neiman, Y. Larring, T. Norby, *Protons in $Sr_3(Sr_{1+x}Nb_{2-x})O_{9-3x/2}$ perovskite*, Solid State Ionics **125** (1999) 369–376.

[102] S. Suzuki, S. Nakashima, *In-situ IR measurements of OH species in quartz at high temperatures*, Phys. Chem. Minerals **26** (1999) 217–225.

[103] F. Shimojo, K. Hoshino, H. Okazaki, *Effects of doped acceptor ions on proton diffusion in perovskite oxides: A first-principles molecular dynamics simulation*, J. Phys.: Condens. Matter **10** (1998) 285–294.

[104] I. E. Animitsa, A. Y. Neiman, A. R. Sharafutdinov, M. G. Kazakova, *Strontium Tantalates with a Perovskite Structure: Their Conductivity and High-Temperature Interaction with Water*, Russ. J. Electrochem. **37** (2001) 266–272.

[105] T. Norby, *Solid-state protonic conductors: Principles, properties, progress and prospects*, Solid State Ionics **125** (1999) 1–11.

[106] J. Crank, *The mathematics of diffusion*, Oxford University Press, 1975.

[107] T. Ishihara, H. Matsuda, Y. Takita, *Oxide ion conductivity in doped $NdAlO_3$ perovskite-type oxides*, J. Electrochem. Soc. **141** (1994) 3444–3449.

[108] N. J. Long, F. Lecarpentier, H. L. Tuller, *Structure and electrical properties of Ni-substituted lanthanum gallate perovskites*, J. Electroceram. **3(4)** (1999) 399–407.

[109] C. Klemenz, *High-quality $La_3Ga_{5.5}Ta_{0.5}O_{14}$ and $La_3Ga_{5.5}Nb_{0.5}O_{14}$ LPE films for oscillators and resonators*, J. Cryst. Growth **250** (2003) 34–40.

[110] P. G. Shewmon, *Diffusion in Solids*, McGraw-Hill Book Company, New York, 1963.

[111] J. Maier, *Mass Transport in the Presence of Internal Defect Reactions-Concept of Conservative Ensembles: IV Tracer Diffusion and Intercorrelation with Chemical Diffusion and Ion Conductivity*, J. Am. Ceram. Soc. **76** (1993) 1228–1232.

[112] K. Schulgasser, *Relationship between single-crystal and polycrystal electrical conductivity*, J. Appl. Phys. **47** (1976) 1880–1886.

[113] H. Kimura, S. Uda, X. Huang, S. Koh, *Equilibrium phase diagram of incongruent-melting langatate ($La_3Ta_{0.5}Ga_{5.5}O_{14}$) and the influence of growth atmosphere and impurity Ir on the resistivity of langatate*, presented at: 15th International Conference on Crystal Growth, August 12–17, 2007, Salt Lake City, USA (preliminary abstract: http://www.crystalgrowth.us/iccg15).

[114] H. Fritze, M. Schulz, H. Seh, H. L. Tuller, *Sensor Application-related Defect Chemistry and Electromechanical Properties of Langasite*, Solid State Ionics **177** (2006) 2313–2316.

[115] D. P. Butt, Y. Park, T. N. Taylor, *Thermal vaporization and deposition of gallium oxide in hydrogen*, J. Nucl. Mat. **264** (1999) 71–77.

[116] B. A. Maksimov, S. S. Kazantsev, V. N. Molchanov, I. A. Verin, B. V. Mill, *Crystal structure and microtwinning of monoclinic $La_3SbZn_3Ge_2O_{14}$ crystals of the langasite family*, Crystallogr. Rep. **49** (2004) 585–590.

[117] M. Kumatoriya, H. Sato, J. Nakanishi, T. Fujii, M. Kadota, Y. Sakabe, *Crystal growth and electromechanical properties of Al substituted langasite ($La_3Ga_{5-x}Al_xSiO_{14}$)*, J. Cryst. Growth **229** (2001) 289–293.

[118] Z. Wang, D. Yuan, A. Wei, H. Qi, X. Shi, G. Zhang, D. Xu, M. Lue, *Growth and optical activity of $Ca_3NbGa_3Si_2O_{14}$ single crystal*, Appl. Phys. **A78** (2004) 561–563.

[119] Y. H. Kang, I. H. Jung, K. Joo, K. B. Shim, K. H. Auh, *Crystal growth and the piezoelectric property of the $Ca_3NbGa_3Si_2O_{14}$ compound*, J. Ceram. Process. Res. **2** (2001) 170–173.

[120] Z. Wang, D. Yuan, Z. Cheng, X. Duan, H. Sun, X. Shi, X. Wei, Y. Lue, D. Xu, L. M., L. Pan, *Growth of a new ordered langasite structure compound $Ca_3TaGa_3Si_2O_{14}$ single crystal*, J. Cryst. Growth **253** (2003) 398–403.

[121] R. B. Heimann, M. Hengst, M. Rossberg, J. Bohm, *Growth and optical activity of strontium tantalum gallium silicon oxide ($Sr_3TaGa_3Si_2O_{14}$, STGS)*, Phys. Stat. Sol. **198** (2003) 415–419.

[122] D. Puccio, D. Malocha, M. M. C. Chou, *Investigations of STGS, SNGS, CTGS, and CNGS materials for use in SAW applications*, IEEE Int. Freq. Contr. Symp. (2003) 627–630.

[123] J. Schreuer, C. Thybaut, M. Prestat, J. Stade, E. Haussuhl, *Towards an understanding of the anomalous electromechanical behaviour of langasite. and related compounds at high temperatures*, IEEE Ultras. Symp. (2003) 196–199.

[124] H. Fritze, D. Richter, H. L. Tuller, *Simultaneous Detection of Atmosphere Induced Mass and Conductivity Variations Using High Temperature Resonant Sensors*, Sens. Actuators, B **111-112** (2005) 200–206.

[125] D. Richter, H. Fritze, T. Schneider, P. Hauptmann, *Selectivity improvement of high temperature resonant gas sensors by application of different electrode layouts*, Sensor, Internat. Conf. (Wunstorf: AMA Service) **12** (2005) 19–24.

[126] E. Ansorge, S. Schimpf, S. Hirsch, B. Schmidt, H. Fritze, J. Sauerwald, *Micromecanical structures in langasite ($La_3Ga_5SiO_{14}$) by wet chemical etching*, Transducers **13** (2005) 908–911.

[127] E. Ansorge, S. Schimpf, S. Hirsch, J. Sauerwald, H. Fritze, B. Schmidt, *Piezoelectric driven resonant beam array in langasite ($La_3Ga_5SiO_{14}$)*, Sens. Actuators, A **132** (1996) 271–277.

[128] J. Sauerwald, D. Richter, H. Fritze, *Micromachined piezoelectric structures for high-temperature sensors*, J. Electroceramics (in press).

[129] S. L. Firebaugh, K. F. Jensen, M. A. Schmidt, *Investigation of High-Temperature Degradation of Platinum Thin Films with an In-Situ Resistance Measurement Apparatus*, J. Microelectromech. Systems **7** (1998) 128–135.

[130] E. EerNisse, *Quartz Resonator Frequency Shifts Arising from Electrode Stress*, IEEE Freq. Contr. Symp. (1975) 1–4.

[131] Y. Watanabe, M. Koyama, H. Sekimoto, Y. Oomura, *Precise Determination of the Optimum Supporting Position of a Stress Compensated (SC) Cut Quartz Crystal Resonator Using a Semiconductor Pulsed-Laser System*, Jpn. J. Appl. Phys. **34** (1995) 2617–2619.

[132] K. E. Heusler, A. Grzegorzewski, L. Jäckel, J. Pietrucha, *Measurement of Mass and Surface Stress at One Electrode of a Quartz Oscillator*, Ber. Bunsenges. Phys. Chem. **92** (1988) 1218–1225.

[133] D. C. Malocha, H. Francois-Saint-Cyr, K. Richardson, R. Helmbold, *Measurements of LGS, LGN, and LGT Thermal Coefficients of Expansion and Density*, IEEE Trans. Ultrason. Ferroel. Freq. Contr. (2002) 350–355.

[134] U. Balachandran, N. G. Eror, *Electrical conductivity in non-stoichiometric titanium dioxide at elevated temperatures*, J. Mat. Sci. **23** (1988) 2676–2682.

[135] K. H. Kim, E. J. Oh, J. S. Choi, *Electrical conductivity of "hydrogen reduced" titanium dioxide (rutile)*, J. Phys. Chem. Solids **45** (1984) 1265–1269.

[136] R. C. Smythe, *Material and Resonator Properties of Langasite and Langatate: A Progress Report*, IEEE Int. Freq. Contr. Symp. (1998) 761–765.

[137] H. Takeda, T. Kato, V. I. Chani, H. Morikoshi, K. Shimamura, T. Fukuda, *Effect of (Sr,Ba) substitution in* $La_3Ga_5SiO_{14}$ *and* $La_3M_{0.5}Ga_{5.5}O_{14}$ *(M=*Nb^{5+}*,* Ta^{5+}*) crystals on their synthesis, structure and piezoelectricity*, J. Alloys Compd. **290** (1999) 79–84.

[138] M. F. Dubovik, K. A. Karutnov, T. I. Korshikova, *The Nature of Langasite Crystals Coloration*, IEEE Int. Freq. Contr. Symp. (1995) 638–641.

[139] H. Haruta, *Agilent technologies impedance measurement handbook,* 2^{nd} *Edition*, Agilent Technologies Co. Ltd, 2000.

[140] C. S. Hsu, F. Mansfeld, *Concerning the Conversion of the Constant Phase Element Parameter* Y_0 *into a Capacitance*, Corrosion **57** (2001) 747–748.

[141] J. A. Kilner, R. A. De Souza, I. C. Fullarton, *Surface Exchange of Oxygen in Mixed Conducting Perovskite Oxides*, Solid State Ionics **86–88** (1996) 703–709.

[142] A. D. Le Claire, *The analysis of grain boundary diffusion measurement*, Br. J. Appl. Phys. **14** (1963) 351–356.

[143] P. Fielitz, G. Borchardt, M. Schmücker, H. Schneider, *How to measure volume diffusivities and grain boundary diffusivities of oxygen in polycrystalline oxides*, Solid State Ionics **160** (2003) 75–83.

[144] J. Schröder, S. Doerner, T. Schneider, P. Hauptmann, *Analogue and digital sensor interfaces for impedance spectroscopy*, Meas. Sci. Technol. **15** (2004) 1271–1278.

Acknowledgements

First, I would like to acknowledge the contributions of the coworkers from Clausthal University of Technology, especially Dr. Michal Schulz, Denny Richter and Jan Sauerwald. Their experimental work and feedback helped substantially to broaden the knowledge about the high-temperature piezoelectric materials.

Prof. Dr. Günter Borchardt supported this work generously by valuable discussions and guaranteeing attractive working conditions. I very much appreciate his help.

In particular, I thank Prof. Dr. Harry L. Tuller and Dr. Huankiat Seh from Massachusetts Institute of Technology. It is always very productive, inspiring and enjoyable to work with them. The tight collaboration is one of the most important driving forces of this work.

The cooperation with Prof. Dr. Klaus Jacobs and Dr. Steffen Ganschow from Institute for Crystal Growth, Berlin-Adlershof, is another important base of this study. Beside the preparation of the single crystals I appreciate the fruitful discussions.

Many others supported this work by providing their experimental techniques and specialized knowledge for data interpretation. In particular, I am thankful to Dr. Claus Rüscher, Sylvain Weber, Dr. Peter Fielitz, Dr. Horst Baumann and Dr. Mario Rudolphi.

Important, despite being mentioned at the end, I express my gratitude to Eberhard Ebeling and Frank Koch for their technical support.

Research grants from German Research Foundation (DFG) and German Government (BMBF) supported this work.